QUANTIFICATION OF TURBULENT CHARACTERISTICS USING HIGH FIDELITY COMPUTATIONAL FLUID DYNAMICS FOR HEAT EXCHANGER APPLICATIONS

A Dissertation

by

JONATHAN K. LAI

Submitted to the Office of Graduate and Professional Studies of
Texas A&M University
in partial fulfillment of the requirements for the degree of

DOCTOR OF PHILOSOPHY

Chair of Committee,	Yassin A. Hassan
Co-Chair of Committee,	Nagamangala K. Anand
Committee Members,	Elia Merzari
	Maria King
Head of Department,	Andreas A. Polycarpou

May 2019

Major Subject: Mechanical Engineering

ABSTRACT

Methods for transferring heat through convection are highly variable and numerous in application. Still, the principle mechanisms that drive convective heat transfer can be reduced down to thermal conditions, fluid properties, turbulent characteristics, and geometric features. Several of these principles will be analyzed through individual projects, which isolate the mechanism under consideration. Using high fidelity computational fluid dynamics (CFD), simulations that encompass variations in thermal properties in fuel rods, buoyancy driven flow within a closed system, and turbulence within a helical coil heat exchanger will be made. Turbulent statistics will be generated and then assessed through various methodologies. Sensitivity to modeling parameters, validation with experimental measurements, and analyzing higher order statistics will be some of the techniques to ensure the accuracy of the simulation.

The main objective of this work is to evaluate the advantages of using high fidelity CFD for heat exchanger applications and add to the wealth of knowledge for improving modeling of complex flows. Understanding the underlying physics for each problem will enable greater confidence in identifying the aspects of a simulation that need further investigation and whether chosen assumptions are justified. Moreover, the resolution and modeling parameters have been documented as a guideline to the minimum size and cost to conduct high resolution simulations of these flows. By using scaling of geometry and Reynolds number, future engineers will be able to use these turbulent quantities as a reference to more effectively improve the efficiency and safety of new designs that involve heat exchangers.

DEDICATION

To my mother, father, and brother.

ACKNOWLEDGMENTS

I would like to acknowledge my mentors Dr. Elia Merzari and Dr. Yassin Hassan for their guidance throughout my graduate school career. Also, the incredible help from Dr. Haomin Yuan and Dr. Paul Fischer were invaluable for learning the details regarding Nek5000. Lastly, I wouldn't have been able to finish my degree without the continuous support and friendship from my colleagues in the CFD Group.

Finally, I would like to acknowledge all our members of the Thermal-Hydraulic Research Laboratory at Texas A&M University (http://thrlab.tamu.edu/) for their help regarding experimental conditions and providing their data for validation. More specifically, Dr. Saya Lee and Marilyn Delgado were helpful for their work with the Helical Coil Steam Generator, and Dr. Rodolfo Vaghetto and Daniel Orea were helpful for their work on the Cold Leg Mixing CFD-UQ benchmark.

CONTRIBUTORS AND FUNDING SOURCES

Contributors

This work was supported by the dissertation committee consisting of Professor Yassin A. Hassan of the Department of Nuclear Engineering, Professor Nagamangala K. Anand of the Department of Mechanical Engineering, Dr. Elia Merzari of Argonne National Laboratory, and Professor Maria King of the Department of Biological & Agricultural Engineering.

The experimental measurements have been provided by the Thermal-Hydraulic Research Laboratory at Texas A&M University (http://thrlab.tamu.edu/) as previously mentioned for both the Helical Coil Steam Generator and the Cold Leg Mixing CFD-UQ benchmark projects. The RANS portion of the Low Prandtl Number channel flow was conducted by Dr. Dibbon K. Walters from the University of Oklahoma and his graduate students, while the LES portion was conducted by Dr. Shanti Bhushan from Mississippi State University and his graduate students. Both academic partners were also very helpful with the progress of the Low Prandtl Number Flow project.

All other work conducted for this dissertation was completed by the student independently.

Funding Sources

This work could not have been possible without the supercomputing resources of the Argonne Leadership Computing Facility, which is a DOE Office of Science User Facility supported under Contract DE-AC02-06CH11357. Portions of this research used the advanced computing resources provided by Texas A&M High Performance Research Computing. Lastly, my graduate study was funded by a fellowship, teaching assistantship, and research assistantship from Texas A&M University for various portions of schooling. The research assistantship is funded by DOE NEUP R&D Award CFA-17-13179 for the Low Prandtl Number Flow project.

NOMENCLATURE

CFD	computational fluid dynamics
PDE	partial differential equation
RANS	Reynolds-averaged Navier-Stokes
URANS	unsteady Reynolds-averaged Navier-Stokes
PANS	partially-averaged Navier-Stokes
LES	large eddy simulation
HRL	hybrid RANS-LES
DNS	direct numerical simulation
Re	Reynolds number
St	Strouhal number
Sc	Schmidt number
Sc_t	turbulent Schmidt number
Gr	Grashof number
Pr	Prandtl number
Pr_t	turbulent Prandtl number
$\mathbf{U}$	velocity vector
U	velocity in x-direction
V	velocity in y-direction
W	velocity in z-direction
y^+	non-dimensional wall normal distance
u_τ	friction velocity
τ_w	wall shear stress

ρ	density
μ	dynamic viscosity
ν	kinematic viscosity
ν_t	eddy diffusion for momentum transfer
α	thermal diffusivity
α_t	eddy diffusion for heat transfer
c_p	specific heat
TKE	turbulent kinetic energy
k	turbulent kinetic energy
η	Kolmogorov length scale
τ_η	Kolmogorov time scale
$\mathbf{g}$	body force vector
ε	turbulent dissipation rate
HCSG	helical coil steam generator
P/D	pitch-to-diameter
FFT	fast Fourier transform
PSD	power spectral density
SEM	synthetic eddy method
IC	initial condition
BC	boundary condition
N	polynomial order in Nek5000
GLL	Gauss-Lobatto-Legendre
OIFS	operator integrating factor splitting
EVM	entropy viscosity method
POD	proper orthogonal decomposition

BM	Boussineq approximation
LM	low-Mach

TABLE OF CONTENTS

Page

LIST OF FIGURES

FIGURE Page

LIST OF TABLES

TABLE Page

1. INTRODUCTION

1.1 Computational Fluid Dynamics

The focus of this dissertation features high fidelity simulations to quantify turbulent flows for heat transfer applications in three different scenarios using computational fluid dynamics (CFD). Due to the advancement of engineering technologies, methods for exchanging heat with convection are vast in variability and complexity. Traditionally, the design process involves scaled experiments into development of statistical correlations. Now, the advent of supercomputing introduces feasibility of a more physics-based approach, using CFD for large fluid domains to obtain whole-field information within the domain of interest. This enables researchers to discover the mechanisms that govern why certain quantities increase or decrease, making it easier to make decisions on which parameters should be modified. This enables the reduction of the number of iterations for experimental tests, and the design process can be sped up.

The basis for CFD usually entails finding solutions to the Navier-Stokes equations. Its derivation can be found in any fluid dynamics book, such as Pope [4], hence only some information will be presented as background. Starting from the law of conservation, the balance of momentum can be derived using an infinitesimal control volume, and the partial differential equation (PDE) can be written in the form of the Cauchy equation

$$\frac{\partial}{\partial t}(\rho \mathbf{u}) + \nabla \cdot (\rho \mathbf{u}\mathbf{u}) = -\nabla p + \nabla \cdot \boldsymbol{\sigma} + \rho \mathbf{g} \tag{1.1}$$

where the stress tensor $\boldsymbol{\sigma}$ for an infinitesimal fluid volume is unknown. Using the linear constitutive theory, the expression for this deviatoric stress tensor can be expressed as

$$\boldsymbol{\sigma} = \zeta(\nabla \cdot \mathbf{u})\mathbf{I} + \mu(\nabla \mathbf{u} + (\nabla \mathbf{u})^T - \frac{2}{3}(\nabla \cdot \mathbf{u})\mathbf{I}) \tag{1.2}$$

Combining Equations 1.1 and 1.2, the general form the Navier-Stokes equations can be derived.

Often, the flow under consideration is incompressible, allowing for divergence-free conditions for velocity. Furthermore, other fluid properties such as viscosity are often assumed to be constant as well. This simplifies mass conservation into the incompressible continuity equation and allows the derivation of the Poisson equation. Now, the number of terms in the Navier-Stokes equations can be reduced tremendously as such

$$\frac{\partial \mathbf{u}}{\partial t} + (\mathbf{u} \cdot \nabla)\,\mathbf{u} = -\frac{1}{\rho}\nabla p + \nu \nabla^2 \mathbf{u} + \mathbf{g} \tag{1.3}$$

$$\frac{\partial \mathbf{u}}{\partial \mathbf{x}} = 0 \tag{1.4}$$

This is known as the instantaneous incompressible Navier-Stokes equations. Due to the chaotic nature of turbulence, it becomes necessary to develop a statistical representation of the important quantities for engineering applications. Rather than wanting the signal of pressure drop or the instantaneous velocity at the outlet, the average pressure drop and average mass flow rate are often quantities of interest. The most common technique to obtain averages is using Reynolds decomposition, where the instantaneous velocity and pressure can be represented using their mean and fluctuating components as such

$$\mathbf{u} = \overline{\mathbf{U}} + \mathbf{u}' \tag{1.5}$$

$$p = \overline{P} + p' \tag{1.6}$$

where the overline denotes the Reynolds ensemble average and the prime denotes the fluctuating component. Applying Equations 1.5 and 1.6 to Equation 1.3, taking the ensemble average of the entire equation, and then applying the statistical properties of Reynolds averaging allows the Reynolds-averaged Navier-Stokes (RANS) equations to be derived as

$$\frac{\partial \overline{\mathbf{U}}}{\partial t} + \left(\overline{\mathbf{U}} \cdot \nabla\right) \overline{\mathbf{U}} + \overline{\mathbf{u}'\mathbf{u}'} = -\frac{1}{\rho}\nabla \overline{P} + \nu \nabla^2 \overline{\mathbf{U}} + \mathbf{g} \tag{1.7}$$

$$\frac{\partial \overline{\mathbf{U}}}{\partial \mathbf{x}} = 0 \tag{1.8}$$

where the Reynolds stress tensor $\overline{\mathbf{u}'\mathbf{u}'}$ can be written as $\overline{u_i' u_j'}$ in Einstein notation. This form of the Navier-Stokes equations can be used to derive other conservation transport equations such as for turbulent kinetic energy or turbulent dissipation. Since the number of knowns remains larger than the number of equations, additional modeling methodologies – which provides closure to the RANS equations – are required before solutions can be found. Many methods have been explored, but the use of eddy viscosity has gained widespread influence for solving the closure problem. One of the most renown eddy viscosity assumptions is the Boussinesq hypothesis [5]

$$-\overline{u_i' u_j'} = 2\nu_t S_{ij}^* - \frac{2}{3} k \delta_{ij} \tag{1.9}$$

$$S_{ij}^* = \frac{1}{2}\left(\frac{\partial \overline{U_i}}{\partial x_j} + \frac{\partial \overline{U_j}}{\partial x_i} - \frac{2}{3}\frac{\partial \overline{U_k}}{\partial x_k}\delta_{ij}\right) \tag{1.10}$$

where ν_t is the eddy viscosity. Typically, the larger the ratio of eddy viscosity to molecular viscosity indicates how much turbulence is modeled, and the higher the Reynolds number (Re) is, the more scales of motion need to be modeled using eddy viscosity or another method based off similar principles. Re is defined as $\mathrm{U_c L_c}/\nu$ where $\mathrm{U_c}$, $\mathrm{L_c}$, and ν are the characteristic velocity, characteristic length, and kinematic visosity respectively. Often, $\mathrm{U_c}$ is based on inlet velocity or bulk velocity, and $\mathrm{L_c}$ is based on hydraulic diameter of the inlet or a geometric parameter.

In order of the most amount of turbulence modeled, the steady Reynolds-averaged Navier-Stokes (RANS) models all the kinetic energy as well as its temporal effects. Then comes the Unsteady Reynolds-averaged Navier-Stokes (URANS), which can capture temporal effects. Next is hybrid RANS-LES (HRL) that encompasses methods that control modeling only some of turbulence, such as bridging methods. After that is Large Eddy Simulation (LES), which can capture most of the subinertial energy by basing its subgrid model off of grid size. And finally, there is Direct Numerical Simulation (DNS) that does not require any model and resolves all motions

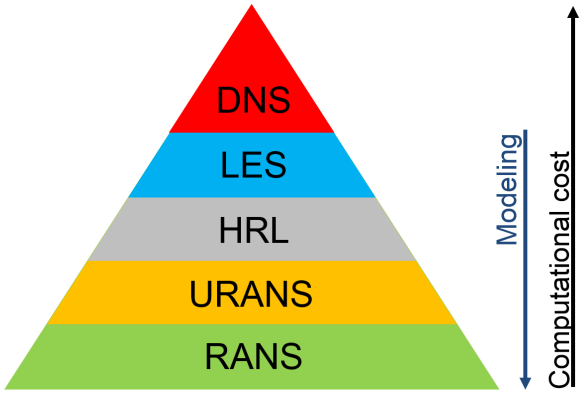

Figure 1.1: Triangle of turbulence modeling relative to the amount that needs to be modeled versus their computational costs.

within turbulence governed by the Navier-Stokes equations. As more turbulence is modeled, the less expensive it becomes to simulate as shown in Fig. 1.1. Each of these methods will be discuss briefly as how it relates to the work in this dissertation.

1.2 Turbulence Modeling

1.2.1 Direct Numerical Simulation

The "brute force" method for solving the Navier-Stokes equations is known as DNS. This technique removes the need for any turbulence model, which makes it the most accurate method. For laminar flows there are less challenges, however for turbulent flows the scales of motion become exponentially small and requires an extremely fine computational mesh to resolve them. In 1941, Kolmogorov made his similarity hypotheses that continues to be influential today [6]. It is systematically derived and concluded that at sufficiently high Reynolds number, the smallest scales of motion are governed by the kinetic viscosity ν and dissipation rate of turbulent kinetic energy ε. Knowing the relationship between ε is the velocity scale cubed divided by the length scale, the following is derived

$$u_\eta = (\nu\varepsilon)^{1/4} \tag{1.11}$$

and knowing that the smallest scale of motion should be of order one, i.e. $\mathrm{Re}_\eta \sim \mathcal{O}(1)$, the Kolmogorov length scale can be written as

$$\eta = (\frac{\nu^3}{\varepsilon})^{1/4} \tag{1.12}$$

and knowing that the velocity scale is the ratio of the length and velocity scale, the Kolmogorov time scale becomes

$$\tau_\eta = (\frac{\nu}{\varepsilon})^{1/2} \tag{1.13}$$

Using Equations 1.11 and 1.12, it can be shown that for three-dimensional turbulence, the number of grid points is proportional to $\mathrm{Re}^{9/4}$. And by using the number of floating-point operations for a given number of grid points, the computational costs will scale to Re^3. Therefore, even moderate Reynolds numbers becomes too expensive for practical purposes [4]. Still, this method has the highest fidelity for the Navier-Stokes equations and serves as a baseline for improving more practical turbulent models. For scientific studies, it is important to ensure that Re is low to enable reasonable computational costs before starting calculations.

1.2.2 Large Eddy Simulation

In Kolmogorov's second similarity hypothesis, it is shown that isotropic turbulence has a common trend in the energy spectrum. At small wave numbers, the large scales of motion are governed by turbulent production. At intermediate scales – known as the subinertial range – energy cascades at a constant rate without significant energy gain or loss. At the largest wave numbers, turbulence is governed by molecular dissipation. The purpose of LES is to model dissipation while still capturing the energy cascade of turbulence. Common techniques involve modeling the residual stress tensor (analogous to the Reynolds stress tensor), which can be derived by applying filtering methods rather than ensemble averaging [4]. The final equation has a similar form to Equation 1.7

$$\frac{\partial\langle\mathbf{U}\rangle}{\partial t} + \langle\mathbf{U}\rangle\cdot\nabla\langle\mathbf{U}\rangle + \langle\mathbf{u}'\mathbf{u}'\rangle = -\frac{1}{\rho}\nabla\langle P\rangle + \nu\nabla^2\langle\mathbf{U}\rangle + \mathbf{g} \tag{1.14}$$

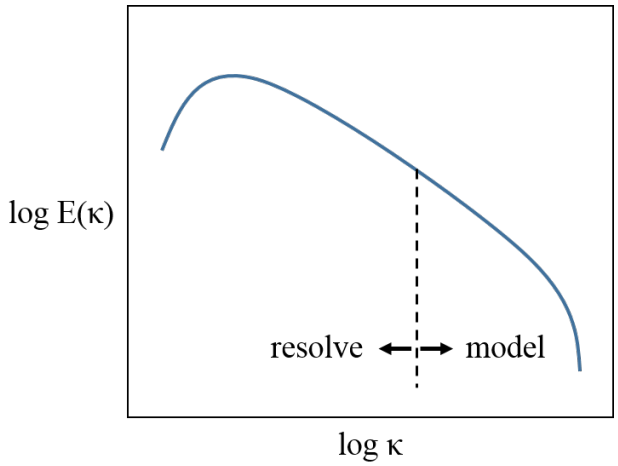

Figure 1.2: The Kolmogorov spectrum for incompressible turbulence showing how LES can resolve some inertial range and models viscous dissipative range.

where solving the term $\langle \mathbf{u}'\mathbf{u}' \rangle$ often uses the sub-grid scale (SGS) model and includes the popular classical Smagorinsky and dynamic Smagorinsky models [7]. However, there are other techniques available for filtering the equations such as pseudo-DNS techniques where numerical dissipation is used.

LES for this research uses a less conventional method that dampens out the smaller scales of motion using a filter at the end of each time step. This is based on the spectral element method with Legendre polynomials, where the higher orders (or modes) that contain the largest oscillations are dampened with this filter. Additional details regarding this particular LES method will be discussed in Section 1.3. Still, the fundamental theory functions the same way, essentially adding more dissipation for mesh elements that cannot fully resolve the turbulence. The energy spectrum shown in Fig. 1.2 demonstrates how smaller wavenumbers will be resolved with LES while still modelling the dissipative motion at the Kolmogorov length scales.

1.2.3 Unsteady Reynolds-Averaged Navier-Stokes

Ensemble averaging of the Navier-Stokes equations produces Equation 1.7 and closure is often provided by finding solutions for the eddy viscosity ν_t. The k-ε turbulence model is one of the most common and will be discussed briefly [8]. Derivations of the transport equations for both turbulent

kinetic energy k and dissipation rate of turbulent kinetic energy ε are done using manipulations of Equation 1.7 and can be found in any book on turbulence [4].

$$\frac{\partial k}{\partial t} + \overline{U_j}\frac{\partial k}{\partial x_j} = P - \varepsilon + \frac{\partial}{\partial x_j}((\nu_t \sigma_k + \nu)\frac{\partial k}{\partial x_j}) \tag{1.15}$$

$$\frac{\partial \varepsilon}{\partial t} + \overline{U_j}\frac{\partial \varepsilon}{\partial x_j} = C_{1\varepsilon}\frac{P\varepsilon}{k} - C_{2\varepsilon}\frac{\varepsilon^2}{k} + \frac{\partial}{\partial x_j}((\nu_t \sigma_\varepsilon + \nu)\frac{\partial \varepsilon}{\partial x_j}) \tag{1.16}$$

$$\nu_t = C_\mu \frac{k^2}{\varepsilon} \tag{1.17}$$

There are many other turbulence models for URANS such as the well-known k-ω by Mentor (1994) and its variants [9]. These new transport equations introduce turbulent coefficients (such as σ_k, σ_ε, $C_{1\varepsilon}$ and $C_{2\varepsilon}$) that have to be calculated empirically. This is the fundamental reason why these equations are not universal and can become very inaccurate when considering flows with different physics and high Re. However, they are advantageous because the computational costs of RANS and URANS are significantly less than LES or DNS and, in fact, can be extremely accurate if a suitable turbulent model, wall function, and grid resolution are properly selected.

The purpose of high fidelity methods such as DNS is to calculate the turbulent budgets, which can be used to empirically derive the best turbulent coefficients. Often, it is assumed that these turbulent coefficients can be scaled to higher Re or to flows with similar physics. Since k is such an essential quantity of turbulence, often its turbulent budgets are calculated from DNS. From the definition of k, the production and dissipation term can be described as

$$k = \frac{1}{2}\overline{u_i u_i} \tag{1.18}$$

$$P_{ij} = -\overline{u_i u_k}\frac{\partial \overline{U_j}}{\partial x_k} - \overline{u_j u_k}\frac{\partial \overline{U_i}}{\partial x_k} \tag{1.19}$$

$$\varepsilon_{ij} = 2\nu \overline{\frac{\partial u_i}{\partial x_k} \frac{\partial u_j}{\partial x_k}} \tag{1.20}$$

1.2.4 Partially-Averaged Navier-Stokes

Hybrid methods are classified under HRL, because they are often more expensive than URANS but cheaper than LES. In the present work, the only HRL method explored is the partially-averaged Navier-Stokes (PANS) model [10, 11]. This turbulent bridging method allows an arbitrary mesh resolution by controlling the amount of turbulent kinetic energy filtered. Decomposition is similar to LES except that instead of wave number, k is implicitly controlled. The two parameters that control this filter width are the following unresolved-to-total ratio of kinetic energy f_k and ratio of dissipation rate f_ε

$$f_k = \frac{k_u}{k} \tag{1.21}$$

$$f_\varepsilon = \frac{\varepsilon_u}{\varepsilon} \tag{1.22}$$

where k_u and ε_u are the unresolved turbulent kinetic energy and the unresolved turbulent dissipation rate, respectively. The advantage of PANS is that it can be implemented in any turbulence solver, because the k_u and ε_u transport equations take the same form as RANS after derivation.

$$\frac{\partial k_u}{\partial t} + \overline{U_j} \frac{\partial k_u}{\partial x_j} = P_u - \varepsilon_u + \frac{\partial}{\partial x_j}((\nu_u \sigma_{ku} + \nu) \frac{\partial k_u}{\partial x_j}) \tag{1.23}$$

$$\frac{\partial \varepsilon_u}{\partial t} + \overline{U_j} \frac{\partial \varepsilon_u}{\partial x_j} = C_{1\varepsilon} \frac{P_u \varepsilon_u}{k_u} - C^*_{2\varepsilon} \frac{\varepsilon_u^2}{k_u} + \frac{\partial}{\partial x_j}((\nu_u \sigma_{\varepsilon u} + \nu) \frac{\partial \varepsilon_u}{\partial x_j}) \tag{1.24}$$

where the unresolved eddy viscosity ν_u and the turbulent coefficients are defined as

$$\nu_u = C_\mu \frac{k_u^2}{\varepsilon_u} \tag{1.25}$$

$$C_{2\varepsilon}^{*} = C_{1\varepsilon} + \frac{f_k}{f_\varepsilon}(C_{2\varepsilon} - C_{1\varepsilon}) \tag{1.26}$$

$$\sigma_{ku} = \sigma_k \frac{f_k^2}{f_\varepsilon} \tag{1.27}$$

$$\sigma_{\varepsilon u} = \sigma_\varepsilon \frac{f_k^2}{f_\varepsilon} \tag{1.28}$$

Comparing these equations to Equation 1.15 and 1.16, it is apparent that the only difference is the quantity the transport equation is solving and their turbulent coefficients. In the same systematic manner that the RANS coefficients were derived, the PANS coefficients can be derived. The present implementation of PANS keeps f_k and f_ε constant throughout the domain, and when f_k = f_ε = 1, it is observed that the RANS equations are being solved. When f_k and f_ε approach 0, the unresolved eddy viscosity goes to zero and the Navier-Stokes equations are being directly solved. Intermediate values are difficult to predict, however it is recommended when there is a clear distinction between high energy and dissipative scales, f_ε = 1 and f_k < 1 [10].

1.3 Spectral Element Method

The spectral element method allows high-order approximations of PDEs within each domain of integration, which will be called an element for the context of this work. By subdividing the entire computational domain into a combination of smaller piecewise elements, a system of algebraic equations can be generated and solved using linear algebra or numerical techniques. This procedure is identical to the finite element method where the weak formulation is made and solved with a set of basis functions. To illustrate this framework, the generalized Galerkin method by Quarteroni and Valli (1994) [12] begins with finding u_N for

$$\mathcal{A}_N(u_N, v) = \mathcal{F}_N(v) \tag{1.29}$$

where $\mathcal{A}_N$ and $\mathcal{F}_N$ are approximations derived from Gaussian quadrature rules defined within the

element. The difference between spectral elements versus finite elements is the particular choice of trial and test functions. Low-order finite elements are numerically efficient, but spectral elements become increasingly more efficient at higher-orders [13]. In summary, the spectral element approximation can be defined as

$$u_N^e(\xi) = \sum_{j=0}^{N} u_j^e \pi_j(\xi) \tag{1.30}$$

where the associated interpolation basis of polynomial order N is given as

$$\pi_j(\xi) = \frac{-1}{N(N+1)} \frac{(1-\xi^2)L'_N(\xi)}{(\xi - \xi_j)L_N(\xi_j)} \tag{1.31}$$

indent where L is the Lagrange polynomial. The present work focuses on using the Gauss-Lobatto-Legendre (GLL) quadrature for each element. Although spectral elements are appealing, it is less flexible for complex element shapes whereas finite elements formulations have been established for any element type. This makes it more difficult for spectral elements to conform to complex geometries and preserve important features.

This method is implemented in open-source FORTRAN code Nek5000 [14]. It is able to scale well with a very high number of processors as shown by others using the same code [15]. The Helmholtz equation is solved for velocity, while the Poisson's equation is solved for pressure using the generalized minimal residual (GMRES) method. There are two solvers that are available: $\mathbb{P}_\mathrm{N}\mathbb{P}_\mathrm{N}$ [16] and $\mathbb{P}_\mathrm{N}\mathbb{P}_\mathrm{N\text{-}2}$ [17] where N indicates the polynomial order. Hence, $\mathbb{P}_\mathrm{N}\mathbb{P}_\mathrm{N}$ means that the discretization of pressure is the same order and slightly more accurate. Also, pressure and velocity are decoupled from each other, which allows for the option of solving non-divergence free flows. Since the discretization of pressure is lower for $\mathbb{P}_\mathrm{N}\mathbb{P}_\mathrm{N\text{-}2}$, the solver is optimized to reduce computational costs and lower pressure iterations at the expense of pressure accuracy.

Within every element, the highest mode in the Legendre polynomials described in Equation **??** has a filter applied at the end of each time step. This filtering attentuation filter α is specified a prior and should be adjusted depending on the resolution of the mesh [18]. This technique is similar to

an explicit low-pass filter, since it removes high frequency oscillations contained within the highest modes. When the flow is properly resolved (as it is in DNS), the energy content within the highest mode approaches zero and the filter will have negligible influence on the solution. However, if the elements are coarser and only LES is under consideration, the filter is required to stabilize the flow and dampen high frequencies.

Temporal discreziation in Nek5000 is based on the high-order operator integrating factor splitting (OIFS) method developed by Maday et al. (1990) [17]. Subintegration of the convective term allows larger timestep sizes with larger Courant-Friedrich-Lewy (CFL) number up to 2-5 while maintaining stability. Time stepping without using extrapolation is also an option to increase speed when smaller time steps are required. Also, the order of accuracy can be selected to be second- or third-order. In the present work, all cases are conducted using second-order temporal discretization.

1.4 Turbulent Processes for Heat Exchanger Applications

To characterize the reliability and importance of high fidelity CFD for heat exchanger applications, a subset of three different cases will be analyzed. Heat exchangers are devices to efficiently transfer heat from one medium to another. The need for cooling or heating is widespread in almost all engineering applications including power plants, refineries, refrigeration, computer cooling, and chemical processing. The driving mechanisms are often multifaceted, involving complex geometry, convection with turbulence, multiphase flow, varying fluid properties, and more. The following three cases analyze some of the most universal processes where turbulence, buoyancy, and fluid properties, respectively, are analyzed

1. Turbulence within the complex heat exchanger of a helical coil geometry.

2. Mixing in a purely buoyancy-driven system with low mass diffusion.

3. Heat transfer within a bare rod bundle with different Prandtl numbers.

This will provide the breadth needed to encompass the mechanisms involved in heat exchangers, yet still provide the depth into each project's applications and technical challenges. Although

high fidelity methods are deemed reliable, it is still important to validate the results with an experimental facility to ensure correctness of boundary conditions and fluid properties. Validation will be conducted on each case at measured region of interests, and then additional information for each project will be extended into other parts of the domain. This will complement existing measurements and provide further insight into the physics involved with the heat exchanger mechanism.

2. HELICAL COIL HEAT EXCHANGER*

2.1 Literature Review

Almost all power plants function using a heat source in order to produce steam to turn an electrical turbine. This process typically uses two fluids, a hot primary coolant that exchanges heat with water which is then converted into steam. Due to their simplicity and ease of construction, the most popular geometries for these heat exchangers are straight or U-shaped tubes. In the recent decades, the chemical, nuclear, and other power industries have explored the use of helically banked tubes. It has been discovered that the helical coil steam generator (HCSG) can transfer more heat per unit volume than straight ones. Prabhanjan et al. studied this geometry using fluid-to-fluid heat transfer, whereas similar studies used constant wall temperature or constant flux boundary conditions. This work shows that helical coil heat exchangers can produce heat transfer coefficients from 16% to 43% larger than straight tubes [19]. Also, their capability to resist flow-induced vibrations and thermal expansion is an additional feature that makes HCSG appealing for small modular reactors and other future power plants [20, 21]. Although their geometry is unique, its physical process can be related to a shell and tube heat exchanger with physics that resemble crossflow over a cylinder.

Interests for HCSG range from both within the tubes and around the shell, however this work will focus only on the single-phase flow across the shell in order to isolate the turbulent process within this geometry. Its wide application to many engineering problems makes crossflow a heavily studied research topic. A heat transfer study by Simoneau and VanFossen (1984) investigated both in-line and staggered array of rods with Reynolds numbers from 5000 to 125,000. For in-line rods, one extra row of rods upstream increased the heat transfer by 50%, while adding up to five extra rows did not increase heat transfer any more. For a staggered array of rods, the addition of up to five extra rows of rods continued to increase heat transfer by amounts from 21% to 64% [22]. Sumner's (2010) literature review of this phenomenon shows that flow behavior in the wake

*Part of this section is reprinted with permission from "Large Eddy Simulation of the Flow Behavior in a Simplified Helical Coil Steam Generator" by J. K. Lai, E. Merzari, Y. A. Hassan, 2019. *Journal of Fluids Engineering*, Vol. 141, 021401-1, Copyright 2019 [1].

and in proximity to the rods can change drastically depending on the pitch-to-diameter (P/D) ratio between rods [23]. The unique aspect of helical coils is that lateral ratio constantly changes due to its geometric nature, while the transverse ratio is generally controlled. An example of this is NuScale Power's steam generator that have rods banked in alternating opposite directions, a patent that has been used as a guideline for the present work's geometry [24]. This rate of change in the lateral ratio, characterized by its banked angle, is a new geometric parameter for HCSG that introduces a wide range of new studies.

Simulations for helical coils has been a prevalent tool for studying their performance. In a study by Rivas and Rojas (2016) using the realizable k-ε RANS model, the simulation results are validated an integrated HCSG experiment with molten salts in Rome. Correlations found in literature were not suitable for the helical coil geometry, hence a new Nusselt number (Nu) correlation has been derived and validated for Re between 400 and 1200 for Pr between 4 to 11 [25]. A similar heat transfer correlation study conducted by Kharat et al. (2009) had to account for additional dependent variables such as the gap between concentric coils, the tube diameter, and the coil diameter. First, validation with experiments using load percentage and temperature relationships were confirmed with reasonable error. Then, optimization techniques were utilized on the new Nu correlation that is valid for the range of Re studied, roughly between 20,000 to 140,000 [26]. More intricate experimental facilities have also been considered such as Jayakumar et al.'s (2008) study where the fluid interaction between the shell and tube is accounted for. At first, RANS simulations were employed using constant temperature boundary conditions and then constant flux boundary conditions, but it is concluded that accurate predictions of Nu requires conjugate heat transfer [27]. As essential as heat transfer correlations are for design, the mechanisms that dictate enhanced heat transfer coefficients per unit volume can only be investigated with the transience of higher fidelity simulations.

Previously mentioned studies have only considered RANS models, whereas more suitable models for higher accuracy require HRL, LES, or DNS. Since difficulty already exists with predicting turbulence on the shell side, including heat transfer is superfluous and studies rather investigate the

forces on the rods to access structural integrity. Yuan et al. (2017) had one-way coupling between LES with a structural analysis code for HCSG. Although focus was on flow-induced vibrations, a comparison between LES and RANS reveal that LES captures larger velocity variances, suggesting the presence of coherent structures that cannot be predicted with Reynolds-averaging techniques [28]. A study by Lee et al. (2018) discovered these vortical structures near the rib surface of a HCSG-like geometry. This investigation is very similar to the present work, where LES and URANS simulations within STAR-CCM+ are validated with experimental measurements. While LES shows better mean velocities, significant improvements are shown in the Reynolds stresses compared to URANS [29].

Most literature for HCSG consider cases where adjacent rods are banked with the same coil angle. However, more complex geometric configurations are also in development such as the design in previously mentioned NuScale Power's steam generator [24]. The alternating curvature of this HCSG enhances turbulent mixing but introduces undesired forces on both sides of the rod which can compromise their integrity. Based on the same patent, Joh (2011) analyzed the thermal hydraulic performance using the standard k-ε method. To reduce the size of the geometry, a 1 degree wedge and 5% of the central region is modeled using periodic boundary conditions in the axial and streamwise direction. The predicted pressure drop is roughly 50% larger than those predicted by correlations [30]. The current work analyzes a simplified version of HCSG where an experimental facility is constructed with a smaller fluid domain. In this case, only the region between two half-rods is built, greatly reducing the number of rods required for modeling while still preserving the essential physics. This reduction in the computational domain makes parametric studies using high-fidelity simulations feasible.

2.2 Experimental Facility

While details of the experiment can be found in Delgado et al.'s (2018) paper [31], essential information will be briefly discussed in this section. The experimental design consists of 12 rods that embody a single-column region, maintaining a transverse P/D ratio of 2.98. The lateral P/D ratio constantly changes along the axial direction of the rods as observed in Fig. 2.1. The rod

diameter is 15.875 mm, and the angle between the alternating rods is 12°. The working fluid para-cymene is kept at 20±1°C throughout each closed-loop experimental run. The volumetric flow rate of 189±4 LPM yields an average inlet velocity of 523.5 mm/s. Using the rod diameter and average inlet velocity as the characteristic length and velocity scale, the Reynolds number is 8643.

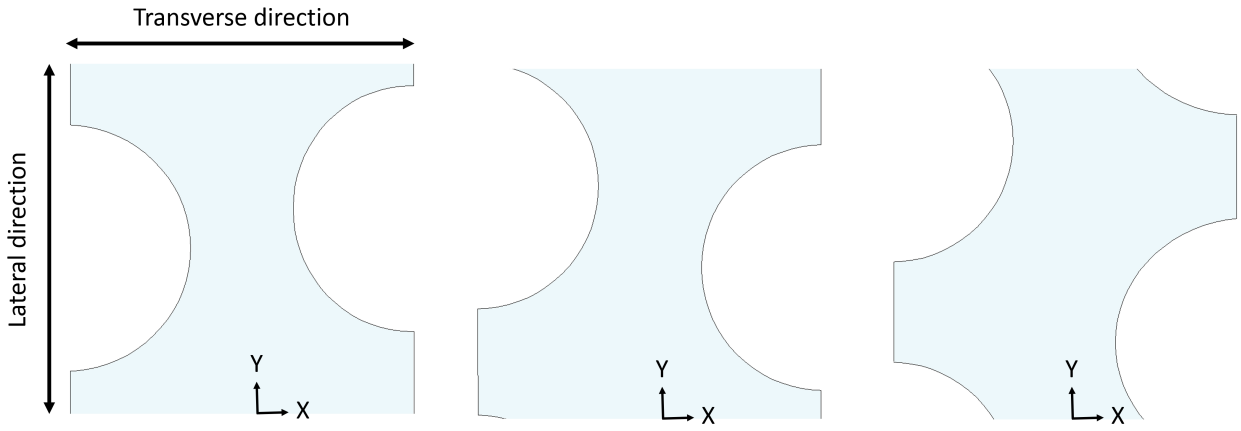

Figure 2.1: Slices of (left) Section A, (center) Section B, and (right) Section C with nomenclature for geometric directions. Reprinted with permission from [1].

The static gauge pressure transducers (OMEGA PX419) measure the pressure dorp above and below the rods to be 2849.8±0.2 Pa, where the uncertainty is the summation of manufacturer uncertainty and statistical error from multiple tests with the same fluid temperature. Particle image velocimetry (PIV) reads the velocity at 10,000 frames/s for the streamwise (lateral) and spanwise (transverse) direction of the flow with a frame size of roughly 24.5×23.2 mm capturing 896×848 pixels. PIV measurements are taken at Sections A, B, C, and D as shown in Fig. 2.2. Sections A, B, and C represent 1/4, 1/2, and 3/4 of the axial length, while Section D is located where Lee et al. (2017) conducted their analyses [32]. Before para-cymene enters the test section, it enters a honeycomb straightener into a mesh grid to replicate uniform inlet boundary conditions. To prove uniformity, PIV measurements with uniform spacing at the inlet are taken and interpolated to create an experimental BC for CFD. Pressure drop measurements for varying Re have been

taken to find similar trends between the simplified test section and multirod test section [33]. Still, the present work will only focus on the lowest Reynolds number to reduce the computational costs for validation. The length and location of the pressure drop is presented in Fig. 2.2, showing that all 12 rods are encapsulated.

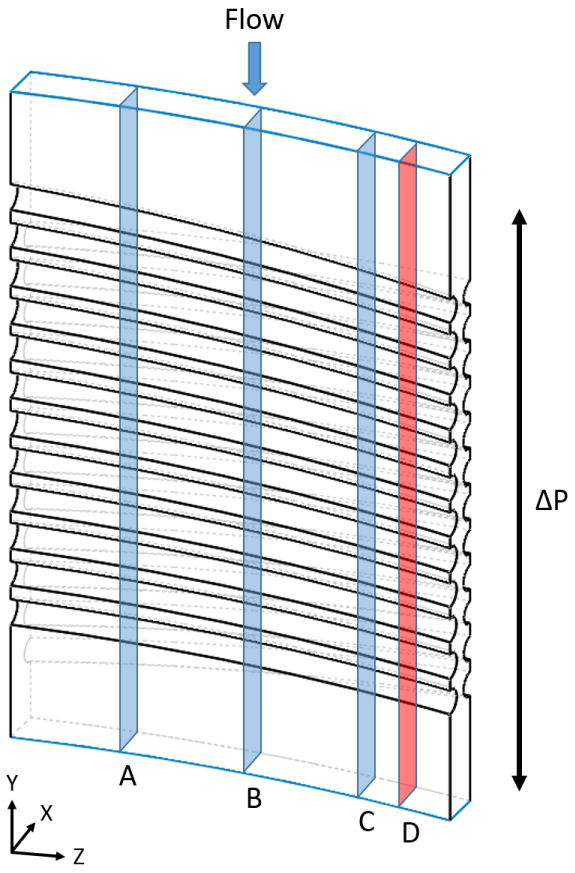

Figure 2.2: Geometry of fluid domain with locations of slices and pressure drop length. Reprinted with permission from [1].

2.3 Computational Domain

LES is conducted using aforementioned spectral element method code, Nek5000. A fully structured hexahedral mesh is created in ANSYS ICEM CFD for the geometry in Fig. 2.2 with extrusions at the inlet and outlet. O-grids are needed at each of the 12 rods, and connectivity is

resolved by filling in the center region with hex elements. After adding refinements near the wall, the elements total to 430,000. Besides than the inlet and outlet, all other surfaces are walls and treated as no-slip BCs for velocity. The skewed elements in the channel center is due to continuous change of the lateral P/D ratio.

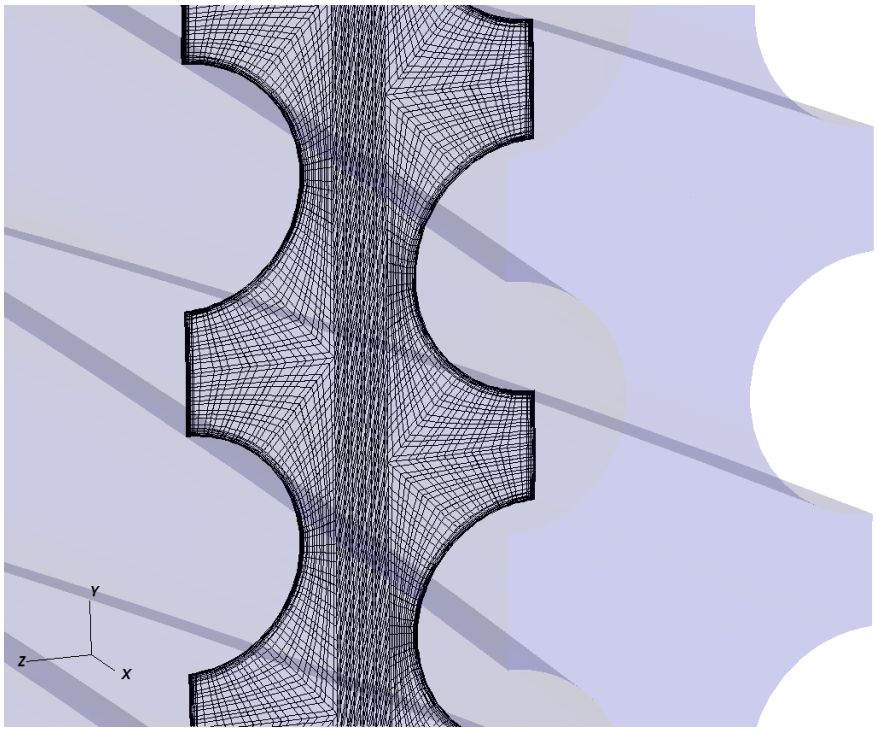

Figure 2.3: Slice of mesh for a 3rd-order polynomial order expansion with GLL points in geometry. Modified with permission from [1].

Discretization into GLL points yields 149×10^6 unique grid points for N = 7 and 316×10^6 unique grid points for N = 9. A lower polynomial order mesh is shown for visualization purposes in Fig. 2.3, which only has 12×10^6 grid points and is not considered for LES. The time step of N = 7 and N = 9 are 1.2×10^{-5}s and 0.9×10^{-5}s respectively. Characteristic time stepping with OIFS extrapolation enables stability for higher Courant numbers, allowing the average CFL number to be roughly 2.

2.4 Synthetic Eddy Method

To replicate realistic inlet boundary conditions, the synthetic eddy method (SEM) is used to generate fluctuations at the inlet. Coherent structures are superimposed on the velocity signal with symmetric shape functions as described by Jarrin et al. (2006) [34]. For a 1D case, the shape function can be defined as

$$\frac{1}{\Delta}\int_{-\Delta/2}^{\Delta/2} f_\sigma^2(x)dx = 1 \tag{2.1}$$

where $\Delta = b - a + 2\sigma$ with a and b as the interval of the inlet and σ is the size of the eddy. Writing these equations in 2D, the local instantaneous velocity signal can be defined as

$$u_j'(\mathbf{x}, t) = \frac{1}{\Psi}\sum_{i=1}^{\Psi} \epsilon_{ij} f_j(\mathbf{x} - \mathbf{x}_i(t)) \tag{2.2}$$

where ϵ is a random step of value $+1$ or -1, $\mathbf{x}_i$ is drawn randomly from $[a-\sigma, b+\sigma]$, and Ψ is the number of eddies. Additional information about implementation of these equations can be found in Jarrin et al.'s work in [34] and [35]. Using the mesh grid at the inlet BC as a reference, the value of Ψ is adjusted based on the number of holes in the mesh grid and the value of σ is based on the size of the square holes.

In addition to adding fluctuations to the inlet, an experiment inlet BC can be developed by interpolating the seven inlet PIV measurements shown in Fig. 2.4 onto the surface. Inaccuracy arises from interpolation, especially for secondary flow measurements, so only the primary component of PIV are mapped. This is a proper assumption, since the secondary flow is less than 5% of the streamwise velocity. Measurements reveal that the turbulent fluctuations yield a turbulent intensity of approximately 6%. Therefore, the root-mean-square (RMS) of the streamwise velocity fluctuations for SEM is specified as a constant value to reproduce an inlet signal comparable to that of the experiment.

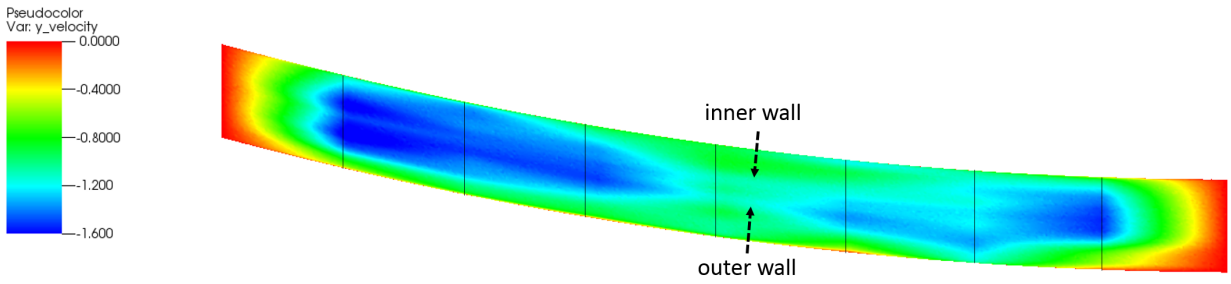

Figure 2.4: Normalized inlet velocity profile using interpolated values from PIV measurements (shown with black lines). Locations of y^+ lines are taken are shown with dashed arrows. Reprinted with permission from [1].

2.5 Verification

2.5.1 Inlet Boundary Condition Sensitivity

The purpose of simulating all 12 rods is to capture fully developed flow characteristics that are independent of the inlet and outlet. Ideally, periodic flow should be used to minimize computational costs, but the complex twisting geometry makes it difficult to properly model periodicity. Analysis at the sixth rod should exhibit the same characteristics regardless of the inlet BC in an ideal scenario. The mapped experimental inlet velocity profile is shown in Fig. 2.4, where data is interpolated from measurements at the black lines. To test the sensitivity of the inlet BCs, the following cases are considered:

1. Const BC: a constant mean velocity calculated using the mass flow rate and cross-sectional area of the inlet.

2. Exp BC: the mean experimental velocity profile using linear interpolation of the seven PIV measurements at the inlet.

3. Exp SEM BC: the experimental velocity profile using SEM to generate the same turbulent intensity as the experiment.

The consequence of interpolating between largely spaced lines is that mass will not always be conserved, therefore velocity measurements have been scaled by a small factor (which was nearly

1) so that Re remains consistent after linear interpolation. Mapping the velocity measurements to GLL points is coded at an additional cost in computational time, especially when higher polynomial orders are considered.

Fig. 2.5 gives a quantitative description of the effects of SEM BC on the variance of streamwise velocity. It is observed that without SEM, the flow becomes fully developed by the fifth rod, while with SEM, the flow becomes fully developed by the fourth rod. The only other discrepancies are due to difference in time integration, i.e. the time averaging was shorter for SEM due to the heavy cost of calculating continuous eddies. It can be concluded that the sixth rod exhibits fully developed flow characteristics and is independent of the inlet BCs.

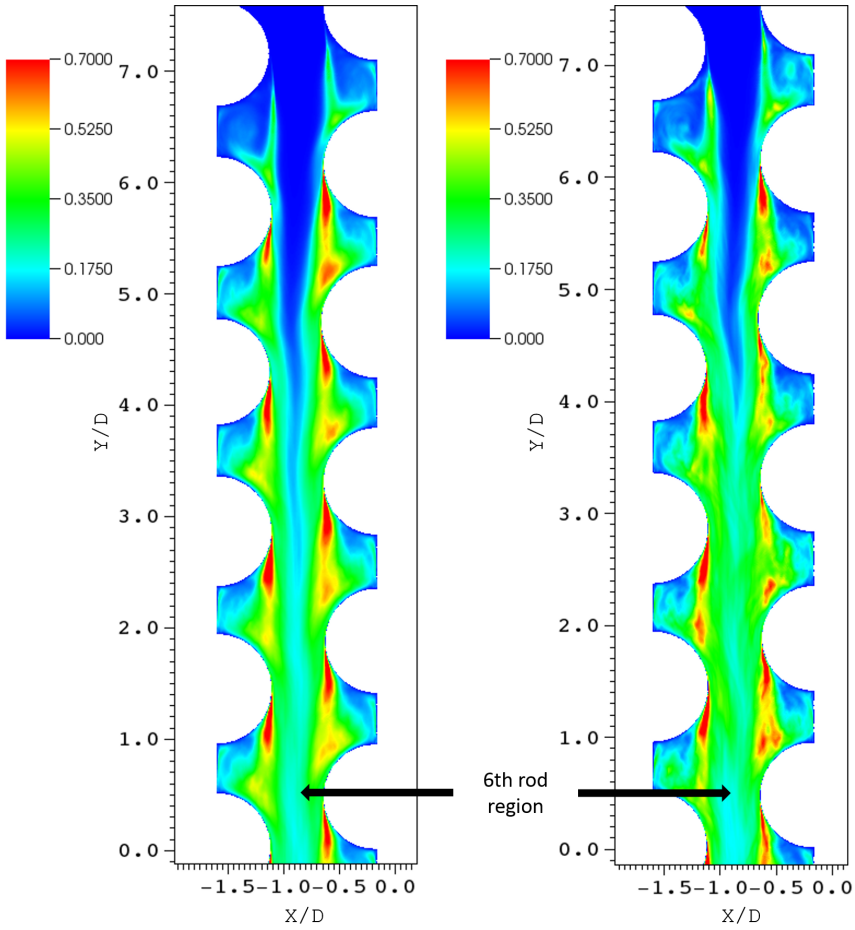

Figure 2.5: Variance of streamwise velocity normalized by inlet velocity (a) without SEM inlet BCs and (b) with SEM inlet BCs. Reprinted with permission from [1].

To substantiate the independence of inlet BCs, Table 2.1 has the pressure drop for each inlet BC under consideration. As expected, Exp SEM BC increases the pressure drop because of the additional turbulence introduced into the system. Still, there is a less than a 1% difference between Exp BC and Exp SEM BC, proving that a turbulent intensity of 6% has a small influence on the overall energy needed to drive the flow. The Const BC case has the smallest pressure drop, but still has less than a 1% difference in comparison with the other cases. The higher pressure drop with experimental BC is due to the introduction of crossflow due to non-uniformity. Overall, it can be concluded that the inlet will not have much effect on the overall solution within the test section and that results for Const BC will still properly represent the physics in the experiment.

Polynomial order	Inlet boundaries	Pressure drop (Pa)	Percent difference (%)
N = 7	Const BC	2960.0	3.9
N = 7	Exp BC	2973.4	4.3
N = 7	Exp SEM BC	2984.4	4.7

Table 2.1: Seventh-order pressure drop with varying BCs compared with experimental value of 2849.8$\pm$0.2 Pa. Reprinted with permission from [1].

2.5.2 Spatial Discretization Sensitivity

Now that suitable boundary conditions are established, sensitivity to the spatial discretization should be verified. Although multiple methodologies exist for grid convergence, p-refinement is the most straight-forward technique for the spectral element method. Solutions for varying degrees of the piecewise polynomial functions are made from N = 5, 7, and 9. In addition to the increase of unique grid points, the time step also decrease as GLL points get closer to the wall, greatly increasing computational costs. To achieve converged statistics for 1.5 seconds, 1×10^6 core-hours, 3×10^6 core-hours, and 10×10^6 core-hours are required for N = 5, 7, and 9 respectively. This simulation time is equivalent to the physical time measured in the experiments. Instantaneous snapshots are gathered for N = 7 due to the high computational cost of I/O from N = 9.

The pressure drop across the 12 rods at aforementioned locations for the different polynomial orders are shown in Table 2.2. Results are intuitive as a lower pressure drop for greater spatial resolution is the result of more energy being captured from the smaller scales of motion. There is a 6.8% difference between N = 5 and N = 7, while there is only a 1.7% difference between N = 7 and N = 9. This large difference in pressure drop for N = 5 hints that important dissipative characteristics are not being resolved, which are present in the higher polynomial orders. In addition to results presented in Table 2.2, further tests were performed at higher polynomial order with different meshing strategies, but with less time integration, confirming consistency in pressure drop with results for N = 9.

Polynomial order	Inlet boundaries	Pressure drop (Pa)	Percent difference (%)
N = 5	Const BC	3162.3	11.0
N = 7	Const BC	2960.0	3.9
N = 9	Const BC	2909.7	2.1

Table 2.2: Constant velocity BC with varying polynomial order compared with experimental value of 2849.8$\pm$0.2 Pa. Reprinted with permission from [1].

2.5.3 Wall Refinement

The curvature of the inner and outer channel have radii of $60.6D$ and $62.1D$, respectively, meaning that the $1.5D$ wide cross section of the inlet and outlet can be assumed to resemble classical channel for analysis. This analogy can be used to validate wall refinements with wall distributions in literature to ensure the low y^+ regions are resolved. To normalize the wall distance and velocity, the friction velocity u_τ is calculated as such

$$y^+ = \frac{y u_\tau}{\nu} \tag{2.3}$$

$$u_\tau = \sqrt{\frac{\tau_w}{\rho}} \tag{2.4}$$

where

$$\tau_w = \mu(\frac{\partial u}{\partial y})_{y=0} \tag{2.5}$$

and the velocity gradient can be calculated using the velocity at the nearest grid point. For the spectral element method, the nearest GLL point from the polynomial basis function can be used as a conservative estimate of the velocity gradient. Values are extracted from spectral space at the inner and outer diameter wall locations drawn in Fig. 2.4. Assuming this region is a straight channel, the first y^+ for N = 5, 7, and 9 are 0.79, 0.44, and 0.28 respectively.

Normalized velocities are overlaid with the theoretical viscous sublayer and Österlund's log-law regime in Fig. 2.6 [36]. For all cases, the viscous sublayer where y^+ equals U^+ is identical. It is not until the buffer layer that the different cases deviate from each other and have minor differences within the logarithmic region. Typically, the constants κ and B^+ are 0.41 and 5.0, respectively, however literature shows that deviations from the log law can occur and are even more likely for three-dimensional flows [37]. Since the curvature of the channel appears to underpredict the y-intercept in Fig. 2.6, the chosen variation of the log-law regime is $\kappa = 0.38$ and $B^+ = 4.1$ [36].

Comparisons between the inner and outer walls show variation in the log-law region. Observations show the outer wall has larger U^+ values compared to those on the inner wall for all simulations. This entails that the curvature of the bent channel introduces crossflow that affects typical channel flow characteristics. The largest deviations between the inner and outer wall are for the experimental BC cases. This is an expected consequence since the nonuniform inlet means that results are spatially dependent. Nonetheless, normalized velocity values from y^+ of 30 to 50 show relatively good correlation with the slope in the log-law regime regardless of the wall under consideration. Therefore, the wall refinement for LES can be considered sufficient for all intents and purposes.

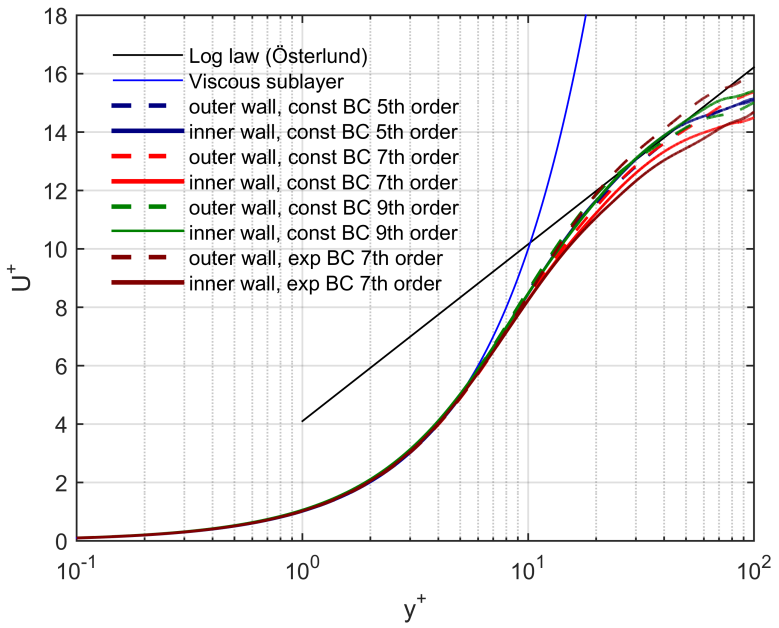

Figure 2.6: Freestream U^+ for inner and outer diameter walls of the curved channel. Reprinted with permission from [1].

2.5.4 Resolving Turbulence

Since turbulence exhibits similar wavenumber evolutions when isolated, the freestream region away from the walls should exhibit behavior similar to behavior described in Section 1.2. With a fast Fourier transform (FFT), the temporal scales can be shown to be resolved by analyzing the turbulence cascade in time. Using Taylor's hypothesis of frozen turbulence [38], autocorrelation can be used assuming that turbulent fluctuations at one point in the channel center is transported by the mean flow to a second point. Therefore, the point selected must be far from the walls where it is not affected by the BCs. The power spectrum in this freestream region between the two rods is shown in Fig. 2.7. The slope of normalized power over frequency is approximately -5/3, indicating that the temporal scales match the cascade for theoretical turbulence.

In addition to resolving turbulence temporally, the proper spatial scales can be compared with the Taylor microscale, which is a length scale where viscosity begins to influence the turbulent eddies in the flow. Similar to the Kolmogorov length scale, the mesh can be compared to the

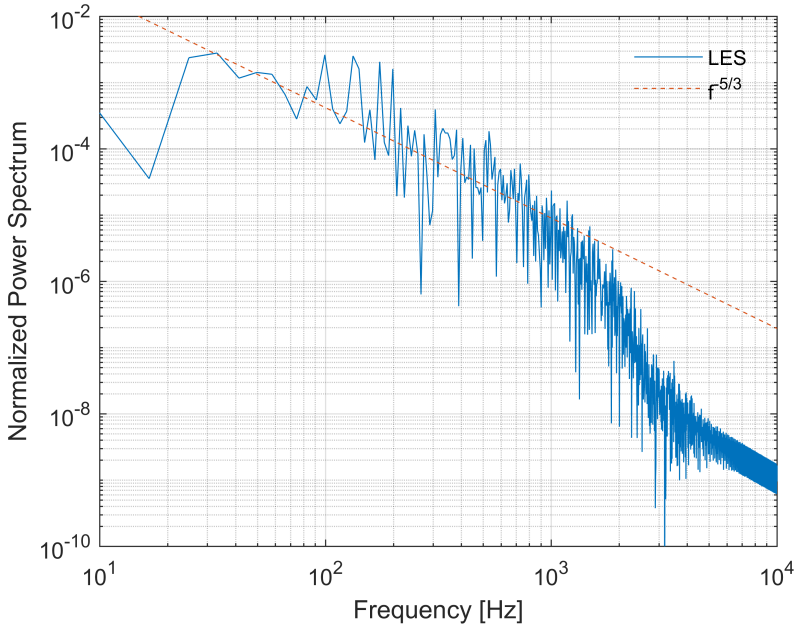

Figure 2.7: Power spectrum at a point in the freestream region with the theoretical slope for the inertial subrange. Reprinted with permission from [1].

Taylor microscale to ensure it is refined enough to capture large eddy effects. Using theory from isotropic turbulence, Taylor derived the length scale as

$$\lambda_t = \sqrt{15\frac{\nu}{\varepsilon}}u' \tag{2.6}$$

where u' is the RMS of the velocity fluctuation and ε is the turbulent dissipation rate. A prior studies were conducted using the realizable k-ε model with STAR-CCM+. Using the same meshing structure, a mesh of 31×10^6 elements is built and imported. Wall functions for an average y^+ of 0.6 and maximum y^+ of 12 are used with the Const BC for inlet. Since large errors exist for RANS for this problem, URANS calculations are made for 1.5 seconds to calculate the variables needed for Equation 2.6. The average pressure drop is calculated to be 2805.6 Pa, meaning that it underpredicts it by 1.6%. This is an expected result as RANS methodologies tend to dampen velocity fluctuations.

The contour of Taylor length scales at the region of interest (at the sixth rod) is presented in

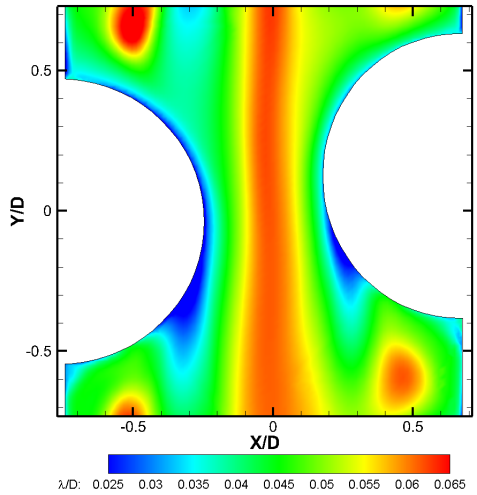

Figure 2.8: Taylor length scale normalized by the diameter of the rod at Section A. Reprinted with permission from [1].

Fig. 2.8. The magnitude of the length scales become relatively the same by the sixth rod, similar to the variance shown in Fig. 2.5. The smallest Taylor microscales are located at the walls and in the wake where the flow separates. Overall, the mesh size is generally half the microscale, since the average ratio of mesh size to Taylor length scale is 0.54, 0.41, and 0.32 for N = 5, 7, and 9, respectively. At local regions, this ratio can be larger, but the Taylor length scale still remains smaller than the mesh size.

2.5.5 Instantaneous Characteristics

A qualitative description of the physics can be made before validating results. As previously mentioned, this geometry has many similiarities with crossflow for an array of rods. In Fig. 2.9, the top right recirculation zone can be observed to have a growing and shrinking effect. This occurs due to the vortex shedding that is common for most rod-based geometries, and following the vectors downstream of this recirculation zone shows that vector arrows alternate in direction accordingly. This pulsating physics can be detrimental for safety concerns, since it amplifies the amount of force that impacts the rods. Instantaneous pressure histories from this data can be used for flow-induced vibrations, such as the study conducted by Yuan et al. (2017) [28]. Future studies can implement these methods to quantify the amount HCSG rods move when under such flow

conditions.

When analyzing the experimental video of instantaneous velocity vectors (not shown), it is observed that the same oscillatory effects are present. If the experimental facility undergoes large fluctuations, it is possible small flow-induced vibrations are present in the test section. Nonetheless, this case study is the first towards this goal and such uncontrolled factors can be assumed negligible. Due to the large fluctuations present in the instantaneous velocity vectors, there will be large magnitudes of RMS velocities relative to the average quantities. Moreover, there could be large flow structures that will be analyzed with techniques discussed in the sections after validation.

2.6 Validation

2.6.1 Velocity Contours

Velocity statistics from LES and PIV are extracted at the sixth and seventh rods from Sections A, B, and C. Measurements have an uncertainty of 17.9 mm/s, which is $\pm 1.7\%$ based on the average gap velocity magnitude of roughly 1.0 m/s. Moreover, it is not out of the question that PIV measurements near the wall could have additional uncertainty due to the camera resolution and lighting on certain regions during measurements. Details have been documented in Delgado et al. [33]. The streamwise velocities in Fig. 2.10 are normalized by the inlet velocity and reveal that the primary flow between LES and PIV are similar in terms of magnitude and shape. Within subchannel center the velocity is at its largest, while within the ribs there is backflow due to flow recirculation. As the location progresses from Section A to Section C, it is clear how the curvature affects P/D ratios and will change the physics as flow separates from the rods. This is less evident with the average velocities but is a crutial factor when analyzing the instantaneous velocities.

One important aspect to observe is the discrepancy between geometry that can accumulate to over one millimeter. Whereas the measured width of Section C covers 23.7 mm, the model covers a length of 22.5 mm. This difference can be explained by manufacturing tolerances and uncertainty of the laser angle. Moreover, it is possible that the theoretical rod diameters do not match the experimental ones. For example, Section B is aligned using the top of the right rod at Y/D of 0.4,

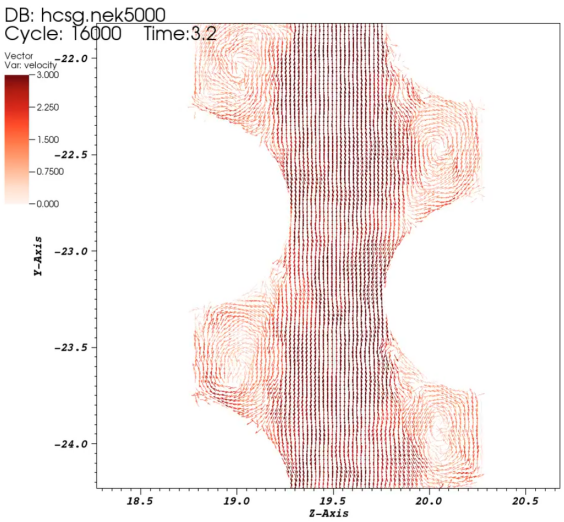

(a) t = 3.2 convective seconds

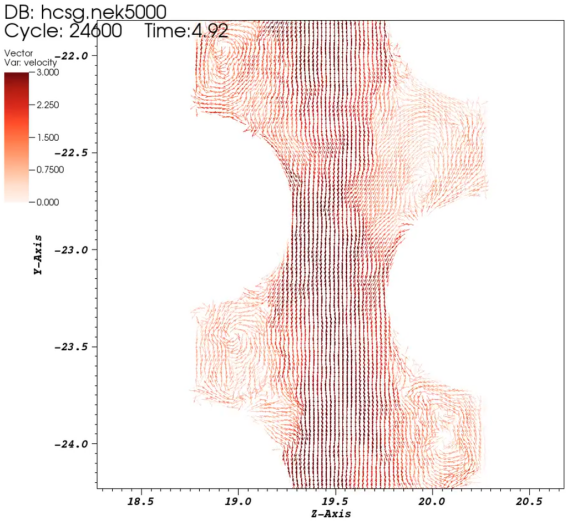

(b) t = 4.92 convective seconds

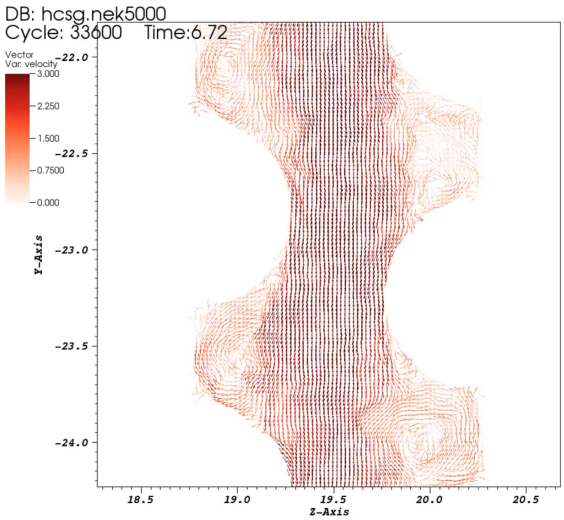

(c) t = 6.72 convective seconds

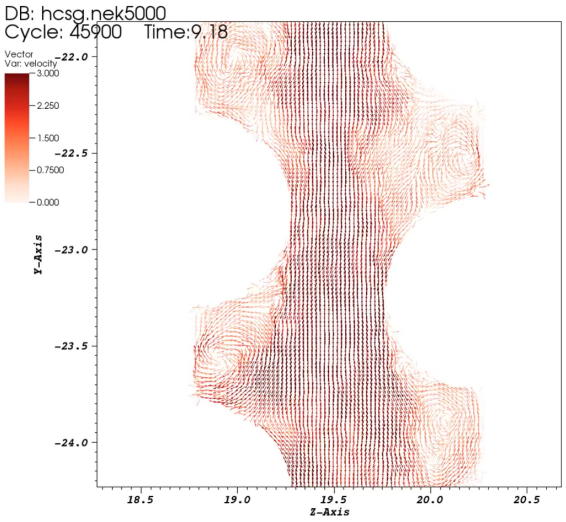

(d) t = 9.18 convective seconds

Figure 2.9: Instantaneous normalized vector contour at various normalized times to show oscillatory physics and flow behavior.

but the bottom of the right rod of the experiment shows that it is 5% larger than the model. Section B also shows that the alignment is not perfect, since the location of the left rod is not identical. Still, the magnitudes of both contours are very similar and should only introduce minor errors. Overall, it can be stated that primary characteristics are all captured using LES.

The streamlines in Fig. 2.11 show that freestream regions and recirculation zones are well captured with LES. The general locations of stagnation points from flow impingement and after flow separation are very similar between PIV and LES. The low stagnation point after flow separation imply the flow is highly turbulent and consists of frequent vortex shedding. The spanwise velocities are also normalized by the inlet velocity and show more deviations compared to the expeirment than the primary flow. The magnitudes of transverse flow are generally smaller for PIV than LES, which is most noticeable in Section B. Generally, LES predicts nearly symmetric flow between the left and right rods regardless of the section under consideration. However, PIV has less symmetry and is most evident in Section C, where the magnitudes of the spanwise velocity on the left rods are much greater than on the right. In ideal conditions, the flow should exhibit symmetric characteristics because the slices are far from the side walls, and it is not out of the question that experimental uncertainty could be a factor.

2.6.2 Velocity Profiles

It is difficult to make wall-to-wall comparisons, since width slices are different and zeros do not match. Therefore, comparisons will be made from the wall to freestream regions and adjusted accordingly. Generally, local wall comparisons have similar features with a few regions with poorer results. This is due to the reasons mentioned before. Therefore, Section A is selected due to its higher quality and more symmetric secondary flows, and in Fig. 2.12 lines are extracted from for quantitative comparisons.

Line A1 is located at a point where the flow has not separated from the rod. It is observed that the primary flow is much greater than the secondary flow in Fig. 2.13. The flat profile of the primary flow is due to the large amount of turbulence generated by rib-like geometric changes as the flow crosses the rods. Compared to experimental measurements, gradients in streamwise velocity

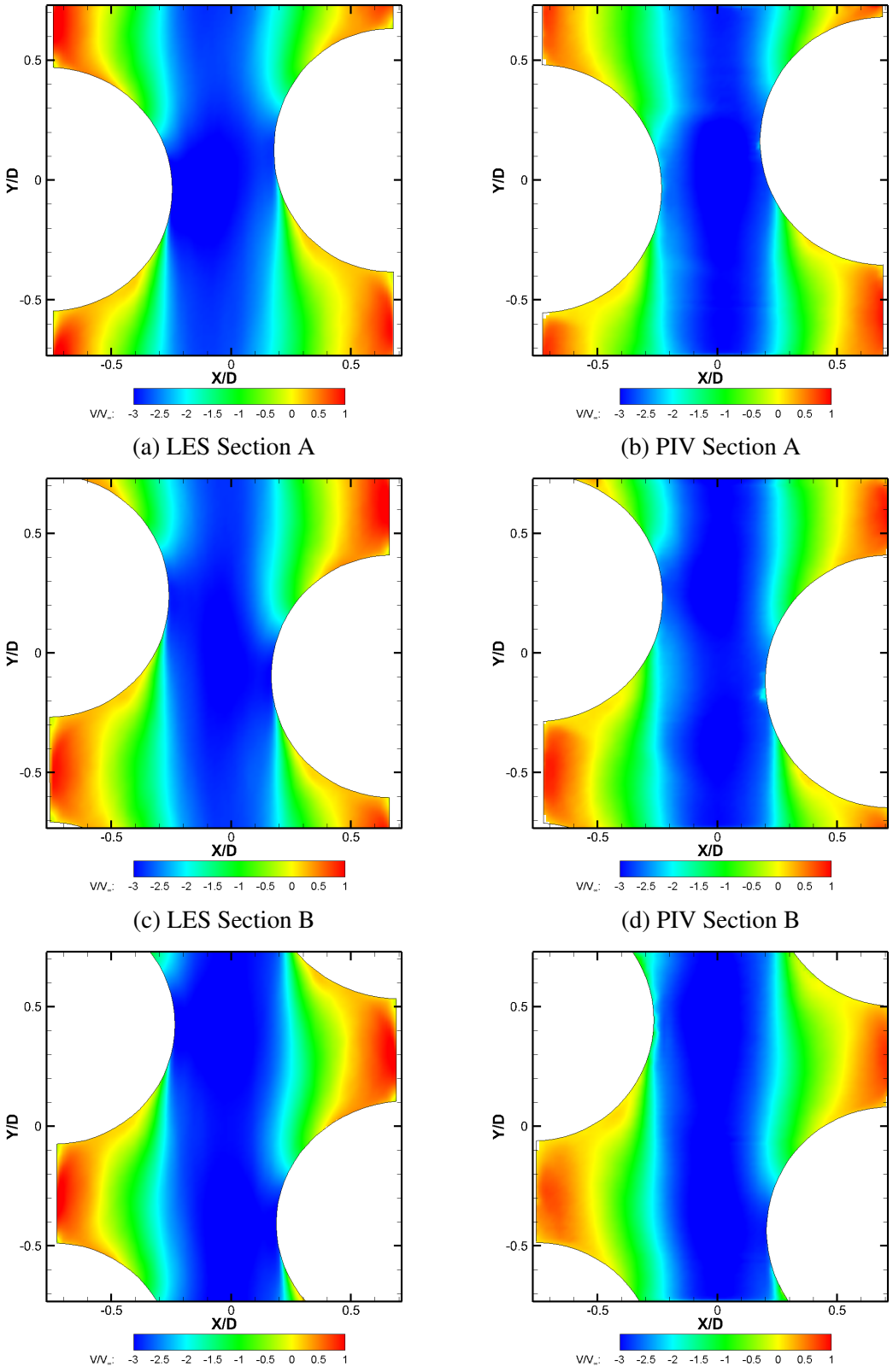

(a) LES Section A

(b) PIV Section A

(c) LES Section B

(d) PIV Section B

(e) LES Section C

(f) PIV Section C

Figure 2.10: Streamwise mean velocity contour for LES and PIV at Section A, Section B, and Section C.

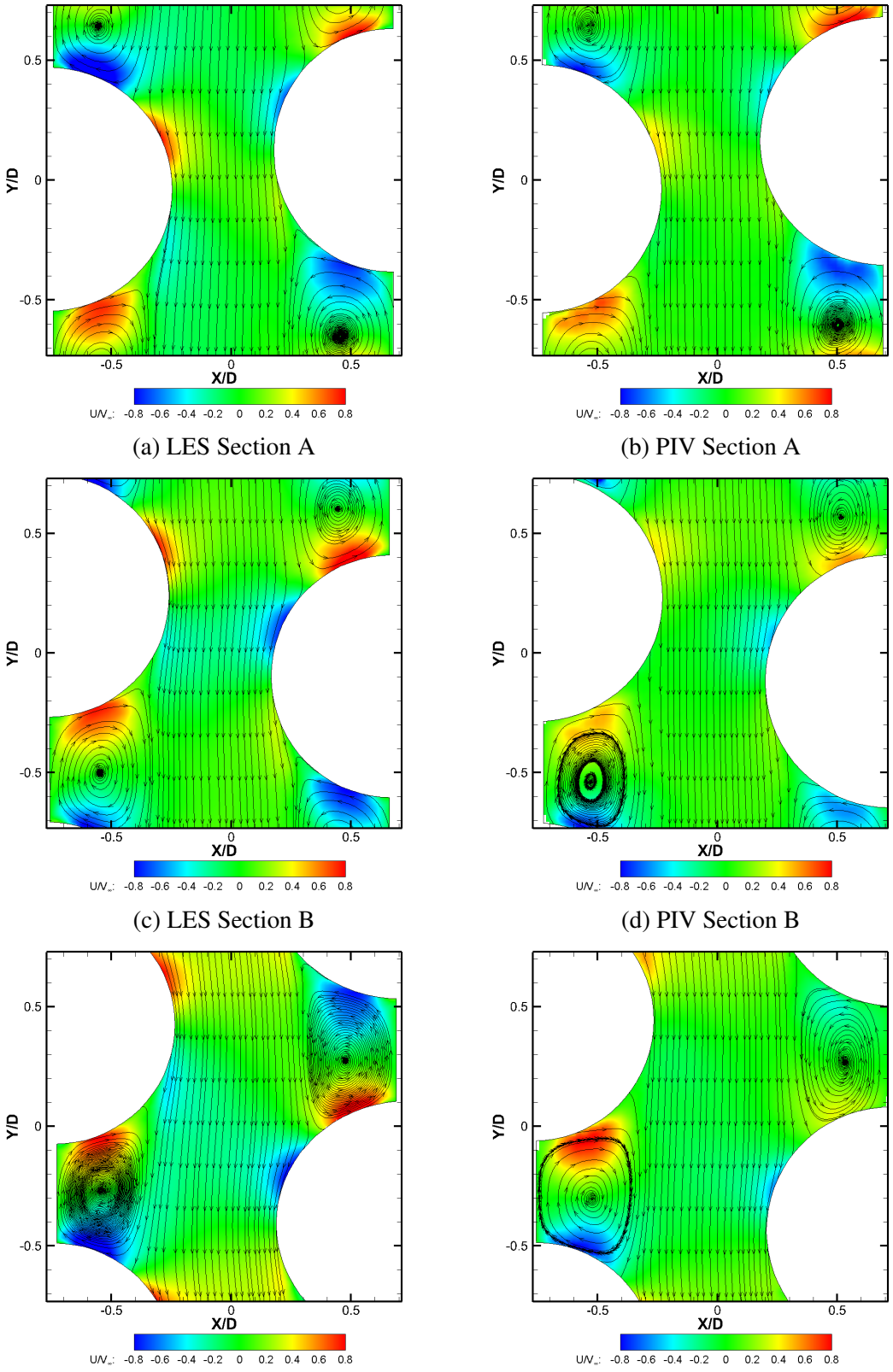

(a) LES Section A

(b) PIV Section A

(c) LES Section B

(d) PIV Section B

(e) LES Section C

(f) PIV Section C

Figure 2.11: Spanwise mean velocity contour and streamlines for LES and PIV at Section A, Section B, and Section C. Reprinted with permission from [1].

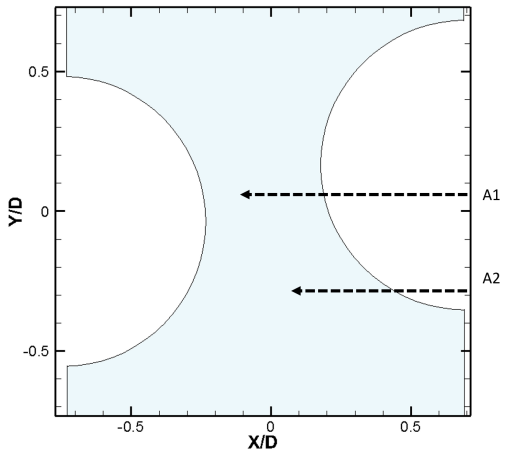

Figure 2.12: Locations of lines extracted from Section A. Reprinted with permission from [1].

for LES near the wall tend to be larger than gradients for PIV. This is a reasonable consequence of having a wider PIV iterrogation area than the extracted width of the model. When comparing the profiles between different simulations for sensitivity, there are little discrepancies for the streamwise direction. Spanwise velocities show greater differences, especially at the center of the subchannel. Here, it is confirmed that that solutions at N = 5 is too coarse to properly resolve the secondary flows in the system.

Line A2 in Fig. 2.14a-b is located in the region after the flow separates from the rod and near the point where it begins to recirculate. This flow is more interesting as when the primary flow is near zero, the magnitude of the secondary flow is very large. Overall, this large transverse flow and minimal primary flow near the wall are captured by LES. The trend where the spanwise velocity is overpredicted and the streamwise velocity is slightly underpredicted is present in other lines not shown. The similarities between N = 7 and N = 9 show that results are consistent and are not highly sensitive to spatial discretization. The use of exp BC introduces greater spanwise velocities, an outcome of having a non-uniform inlet boundary condition. This also explains the source of the larger pressure drop when using BCs that incorporate the interpolated experimental measurements. Still, the differences between LES and PIV are minor for first-order statistics and most prominant characteristics have been captured.

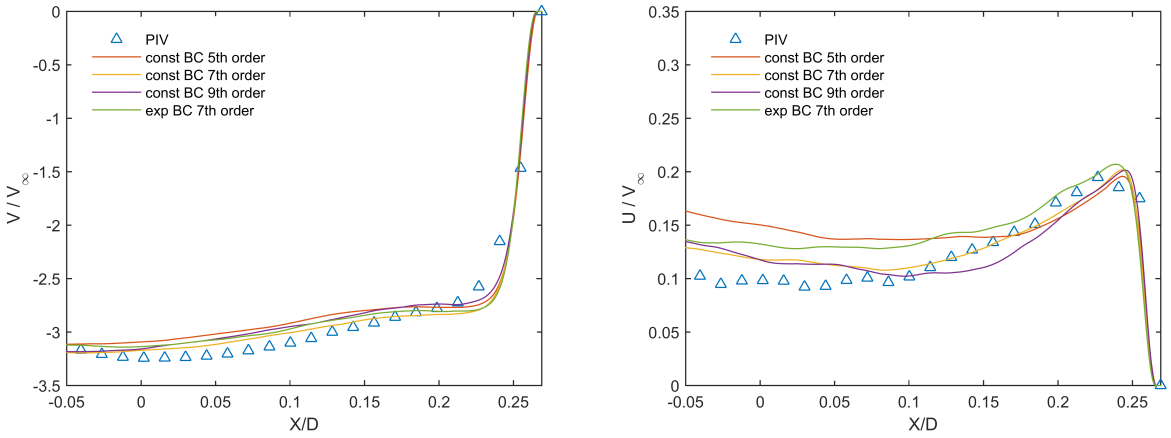

(a) (b)

Figure 2.13: Velocity at line A1 for (a) streamwise mean and (b) spanwise mean direction. Reprinted with permission from [1].

2.6.3 Reynolds Stresses

The fluctuating components of the velocity are presented as RMS in Fig. 2.14c-d and are normalized by the inlet velocity. Streamwise fluctuations show good correlation with the experiment, with significant improvement with N = 9. The peak of at X/D of 0.27 where the flow separates from the rod tends to be overpredicted for both components of flow. Greater overprediction compared to PIV in the transverse direction occurs, since the magnitude of the these velocities are much larger. The polynomial order appears to have a greater effect on higher-order statistics, where N = 9 shows notable differences compared to N = 5 and N = 7. On the other hand, the inlet BC only has minor differences between the various LES simulations as the peaks for both N = 7 cases are the same. This reinforces the fact that results within the region of interest are independent of the inlet BCs.

The shear stress in Fig. 2.14e and shows the similar trend of overprediction at the peak where there is flow separation. Still, the shape is similar to PIV with smaller magnitudes near the wall and larger ones at flow separation. Solutions at N = 9 produce much better results at the near-wall regions, indicating that the only method to get more accurate results for the Reynolds stress is to increase the resolution. Since smaller eddies are being resolved with N = 9, it can be deduced that

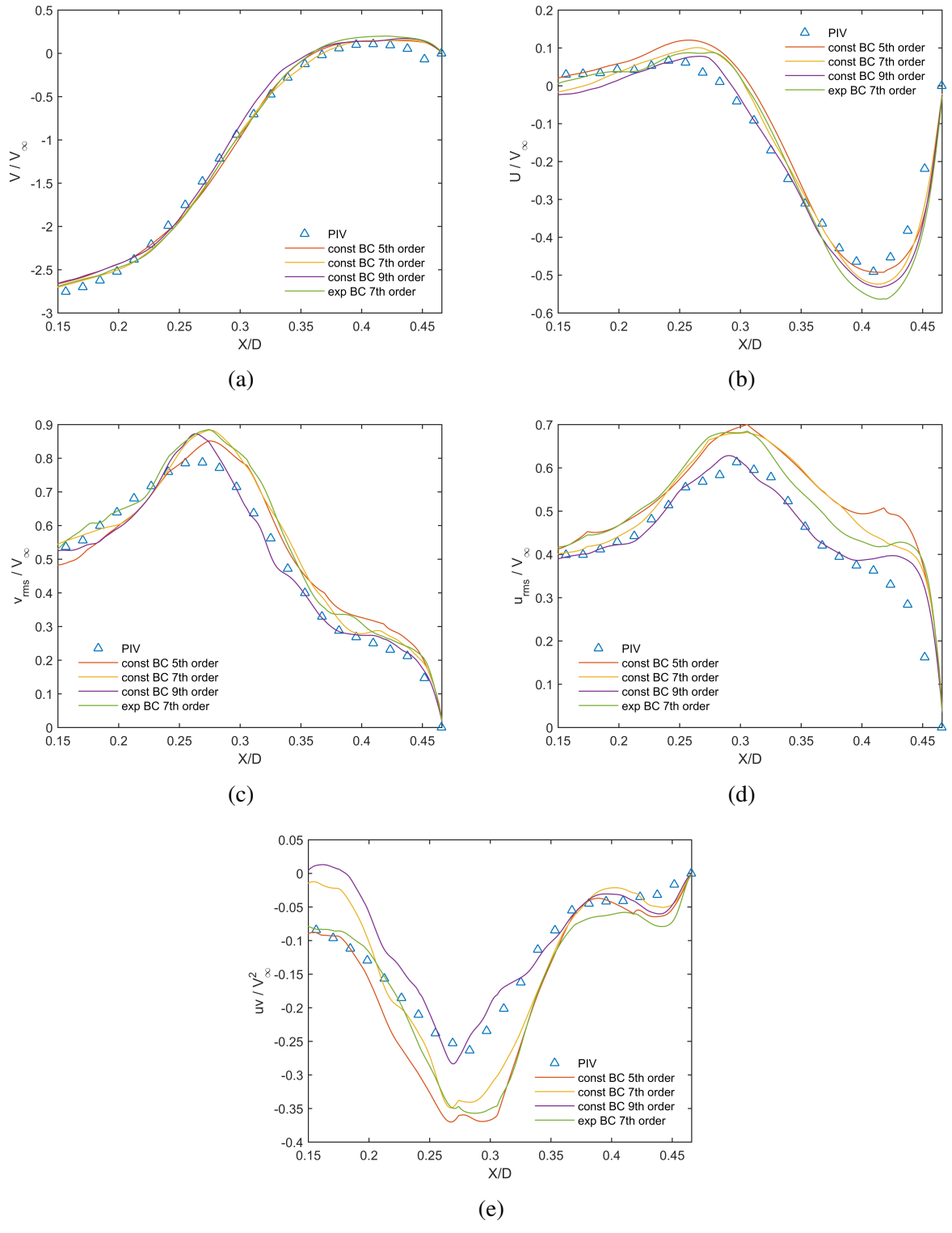

Figure 2.14: Velocity at line A2 for (a) streamwise mean, (b) spanwise mean, (c) streamwise RMS, (d) spanwise RMS, and (e) shear Reynolds stress. Reprinted with permission from [1].

these dissipative effects (which improved the pressure drop) also improve the fluctuations inside the HCSG. The experimental measurement time has been used as a reference for the simulation time, so difficulty in converging higher-order statistics becomes another source of the discrepancies for these sensitivity analyses. Nonetheless, the overall trend and magnitude of the flow matches well with PIV showing that LES simulations have been validated.

2.6.4 Proper Orthogonal Decomposition

A prevailing method for studying turbulence is proper orthogonal decomposition (POD) due to its simple description and its ability to characterize spatial-temporal effects by decomposing them into their most energetic modes. Quantifying instantaneous field data into matrices makes this method a powerful tool for studying the physics in both PIV and LES. Large flow structures are present in the mode with most turbulent kinetic energy and can be visualized in the first modes, while smaller flow characteristics are contained in later modes. Although the initial work in POD for turbulence was introduced by Lumley (1967) [39], this work will discuss one of the most popular techniques for solving these equations, known as the method of snapshots by Sirovich (1987) [40]. Nonetheless, the mathematical basis of POD is the same and starts with finding a solutions to the following equation

$$\int_{\Omega} \mathbf{R}(\mathbf{x}, \mathbf{x}')\mathbf{\Phi}(\mathbf{x}')d\mathbf{x}' = \lambda\mathbf{\Phi}(\mathbf{x}) \tag{2.7}$$

where Ω is the spatial domain, $\mathbf{R}$ is the two-point correlation tensor, λ are the eigenvalues, and $\mathbf{\Phi}$ are the eigenfunctions. By using numerical approximations for the two-point correlation and writing the basis modes as the original dataset, the system of equations can be written as the following eigenvalue problem

$$\mathbf{CA} = \lambda\mathbf{A} \tag{2.8}$$

where $\mathbf{C}$ corresponds to the auto-covariance matrix and $\mathbf{A}$ are the coefficients for the basis modes, which are defined as

$$\mathbf{C} = C(i,j) = \frac{1}{N}(u^T(\mathbf{x},t^i)u(\mathbf{x},t^j))i, \quad j = 1,...,N \tag{2.9}$$

$$\mathbf{A} = A(t^n), \quad n = 1,...,N \tag{2.10}$$

Once the eigenvalues are found, they must be arranged in descending order such that the first mode contains the most energy. This mathematical simplicity allows the original snapshots to be recovered through matrix algebra. Additional details on implementation can be found in Cavar and Meyer (2012) [41]. Since POD calculations from PIV involve only two components of the flow, local regions of the LES domain are isolated for analyses. Usage of POD in Nek5000 has also been implemented by Merzari et al. (2013) [42] and Fick et al. (2017) [43].

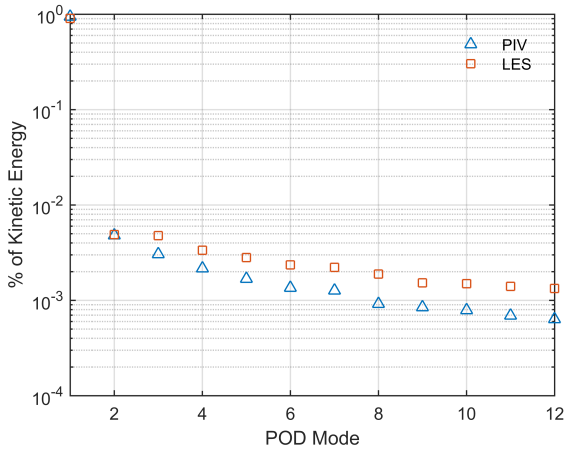

Figure 2.15: Fraction of kinetic energy for the first 12 modes from POD. Reprinted with permission from [1].

Lee et al. (2017) conducted 2D POD analysis on Section D for 1.0 seconds with a resolution of 10,000 frames/s at the sixth rod [32]. The first mode for PIV is calculated as having 94.4% of the kinetic energy, meaning the turbulent kinetic energy in the system is 5.6%. For N = 7 simulations, two-dimensional POD for LES is processed with 2500 snapshots over 1.5 s. LES predicts that

the first mode has 90.6% energy, meaning that the simulation overpredicts turbulent fluctuations as previously shown in line plots. The energy content within each mode is show in Fig. 2.15 on a log scale. Since the first mode from PIV holds more energy than LES, it is expected that LES will overpredict the energy within the other modes. Hence, the decay of energy for higher modes is larger for the experiment compared to LES.

The first mode is showin Fig. 2.16a-b, where the velocity magnitude is calculated from the x- and y-components of the velocity. Here, the larger PIV energy content in the first mode can be attributed to the larger magnitudes in the freestream region. This is consistent with the fact that mean streamwise velocities are slightly larger for PIV than LES. The vectors on this plot also provide insight on the flow direction within the recirculation regions. After the flow separates from the rod, fluid has a bias toward the inner wall. Fluid is directed away from the walls at the next rod and then accelerates toward proceeding rods.

The velocity associated within each POD mode can be calculated by multiplying the mode with its POD coefficient, obtained by projecting the flow field onto the mode. Flow structures can be observed using the second mode show in Fig. 2.16c-d. Large recirculation regions form within the subchannel close to rod walls and advect the flow between rod columns. The intensity of the structures is highest immediately before the flow impinges on the rod and could be a source of high pressures and fluctuations. The region where the flow separates from the rod for LES is generally larger than for PIV. Still, the agreement is remarkable, proving that LES is capable to capturing the main features from higher-order statistics.

Detailed POD analysis is only conducted for this 2D slice due to the availability of experimental calculations. However, 3D POD has been conducted as well (not shown) to find other rods regions have much different flow structures, a feature not present when observing the RMS velocities and Reynolds stress. Whereas high-order modes present a high degree of symmetry and coherence, this is not the case for the lower energy POD modes. The lower energy modes reveal features of decorrelation and asymmetry that requires much higher resolution and time integration for both PIV and LES to properly validate.

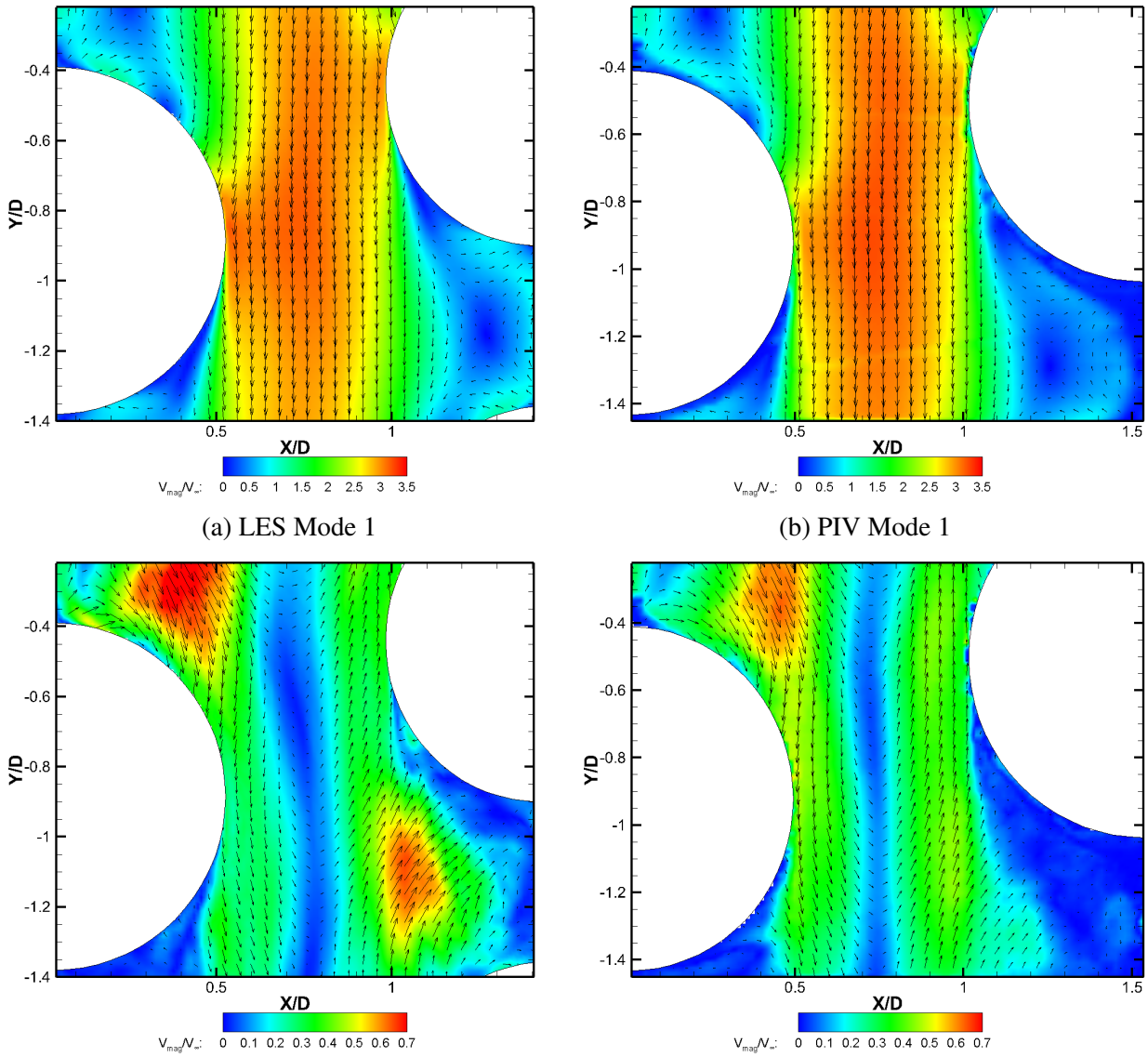

(a) LES Mode 1

(b) PIV Mode 1

(c) LES Mode 2

(d) PIV Mode 3

Figure 2.16: POD of mode 1 for (a) LES and (b) PIV and POD of mode 2 for (c) LES and (d) PIV. Reprinted with permission from [1].

2.6.5 Coherent Structures

To visualize coherent structures in the flow, the Lambda-2 (λ_2) vortex criterion is calculated from an instantaneous flow field [44]. Fig. 2.17 presents the motion of vortices for λ_2 = -1$\times 10^6$ s^{-2} superimposed on the contour of pressure in the system. The effect of geometry is clear, since the friction from the rib-like channel generates large turbulence structures. The highlighted upper region consists of many vortical structures, perhaps associated with entrance effects. On the other hand, the highlighted downstream region has less vortices in the outer wall-bounded area. This instantaneous time frame has bias attributed to vortex shedding that occurs after the flow separates from the rods at regions with high variance, as observed previously in Fig. 2.5. Typically, the full Kármán vortex street should be observed in regular crossflow, but the additional walls to simplify the geometry dampen this effect.

Coherent structures are generated in regions of flow separation and advected in a pulsatile fashion by modes of the type shown in Fig. 2.16c-d. The presence of vortex shedding manifests itself within a smaller scale, causing recirculation regions to grow and shrink in an oscillatory manner. Unlike previous analyses, the Lambda-2 vortex criterion gives insight into the 3D transient effects in this geometry. Local regions in the z-direction have less vortices while other regions are grouped at the location of the large eddies.

2.7 Conclusions

LES of the simplified, single-column HCSG reveals the capabilities of CFD for investigating the detailed physics for this type of heat exchanger. Results can be used as a guideline on the requirements necessary to properly capture the physics in this flow for future design and RANS simulations. It is discovered that the pressure drop shows little sensitivity to the inlet BCs, while minor differences are found for the lowest spatial resolution under consideration. The law of the wall and turbulence length scales were also analyzed to justify that the mesh is sufficient for capturing important dissipative effects. Instantaneous velocity vectors and λ_2 vortex criterion show that flow oscillations are present due to vortex shedding from the rods.

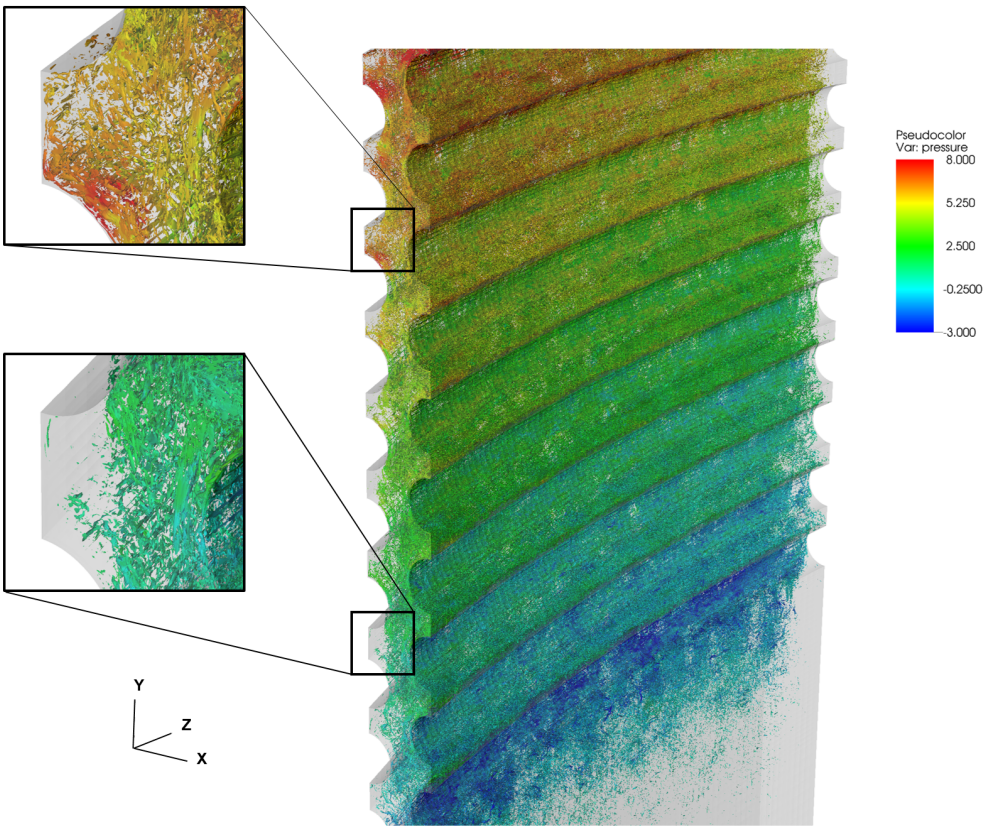

Figure 2.17: Instantaneous isosurfaces of λ_2 = -1$\times$10^6 s^{-2} with contour of normalized pressure imposed. Reprinted with permission from [1].

Contours of first-order statistics using the mean flow show remarkable similarities with PIV measurements. The difference in spanwise velocities can be attributed to the fact that experimental measurements were not as symmetric as LES, perhaps due to tolerances or uncertainty with modeling an ideal geometry. Quantitative comparisons of lines at Section A reveal good agreement despite minor geometric differences. The shapes of the Reynolds stresses and fluctuations match well, but the peaks are overpredicted. POD is also conducted to show primary modes agree well with experimental measurements. However, LES shows a lower decay rate for POD when analyzing the energy content of higher modes. Overall, simulations of the complex heat exchanger is validated with experimental results, and the resolution and boundary conditions are documented to be used as guidelines for larger scale HCSG efforts.

Deeper insight into modeling requirements and necessary physics have been provided with high fidelity simulations. Although turbulence can aid in heat transfer, an excessive amount can have adverse effects and reduce the heat transfer cofficient. Future work can include the addition of heat flux at the rods, similar to an actual HCSG, and investigate its efficiency per unit volume compared to other types of heat exchangers. Moreover, the main goal of this project is to obtain accurate pressure signals from the turbulent field for future work and use them for flow-induced vibrations. Though outside the scope of this work, future researchers can use data from stored history points to do structural analyses.

3. BUOYANCY DRIVEN FLOW*

3.1 Literature Review

The next phenomenon under consideration for heat exchanger applications is turbulent mixing between fluids of different properities due to buoyancy. Nonlinear hydrodynamics give rise to instabilities, coherent structures, and anisotropy that continues to challenge scientists and engineers alike. When there are changes in viscosity between fluids, there are significant impacts to the rate of mixing as well as changes the effective Reynolds number. Even with lower Re, viscosity differences between two fluids impacts the mixing characteristics during fluid injection as shown by Campbell and Turner (1985) [45]. Moreover, a study by Youngs (1991) on varying density differences show large changes in turbulent kinetic energy and density fluctuations [46].

One parameter that describes hydrodynamic instabilities is the Atwood number (A), which is defined as the density difference divided by their sum. The most simple, yet effective model for buoyancy is the Boussinesq approximation whose applicability corresponds to $A \rightarrow 0$ and lumps density difference effects into a single source term. Still, its practicality extends to predicting more complex instabilities such as Rayleigh-Taylor even at higher A, with reasonable error as shown by Mikaelian (2014) [47]. Livescu and Ristorcelli (2008) investigated isolated buoyancy driven turbulence to show that although mixing rates can drastically change at high A, the Boussinesq approximation can still be useful for lower-order integrated quantities. Also, they discovered large-scale influences when varying other non-dimensional parameters, such as the Schmidt number on the integral legnth scale [48]. Another study by Mueschke et al. (2009) on the Schmidt number indicates that there are large effects on mixing for even small Reynolds numbers [49].

Mixing of variable-density fluids has a critical role for nuclear power safety during the accident scenario of emergency core cooling (ECC) injection. This is due to a phenomena known as pressurized thermal shock (PTS) where rapid cooling of reactor vessel walls lead to dire consequences,

*Part of this section is reprinted with permission from "Sensitivity analyses in a buoyancy-driven closed system with high resolution CFD using Boussinesq approximation and variable density models" by J. K. Lai, E. Merzari, Y. A. Hassan, 2019. *International Journal of Heat and Fluid Flow*, Vol. 75, 0142-727X, Copyright 2019 [2].

such as jeopardizing the integrity of the material. Turbulent mixing quantities such as density gradients are essential in the cold leg-downcomer region where cold water enters the reactor vessel region [50]. Early studies by Wolf et al. (1987) analyzed experimental temperature measurements for the cold leg-downcomer region and concluded that thermal mixing can mitigate extreme thermal shocks. However, stress fields due to the cold plume region causes large axial stresses near the cold leg nozzle [51]. Experimental data from multiple test facilities has been gathered by Theofanous and Yan (1991) and interpreted by various transient codes to predict cooling. This is due to the complicated three-dimensional mixing within the cold leg-downcomer junction [52]. Advancements in supercomputing and CFD have now made it possible to predict mixing with higher fidelity.

Both experimental and numerical investigations on ECC injection indicate the dominance of buoyancy effects between hot and cold water. After verification through grid and model sensitivity, transient analyses by Scheuerer and Weis (2012) show turbulent mixing near the nozzle tends to be underpredicted with RANS simulations [53]. Another RANS calculation of PTS was performed by Shams et al. (2016) with different Re, Pr, and geometrical considerations to design a DNS benchmark case. Predictions show that even with a simplified geometry, over a billion grid points are needed to resolve the calculated Kolmogorov length scales [54]. Therefore, the only feasible method for high fidelity CFD for such a phenomenon is with scale-resolving simulations such as LES. Investigation on identifying the required mesh resolution for LES has been discussed among Loginov et al. (2010), and it is found that mixing in the downcomer is very sensitive to the fluctuations of the fluid injection for single phase flow [55]. Hence, sensitivity to boundary conditions must be examined for such cases.

Unlike previous studies, this buoyancy driven flow case focuses on LES of a completely closed system where the only contribution of energy are differences in density between two isothermal, miscible fluids. Due to dissipation from walls and entropy from mixing, system equilibrium will be reached when all momentum is lost and the fluids homogenize. However, the phenomena of interest is fully transient and must be analyzed using small time averaging windows rather than

statistically stationary methods. The Cold Leg Mixing CFD-UQ benchmark has been developed for the Nuclear Energy Agency (NEA-OECD), and LES of this case will be used to judge the capabilities of chosen governing equations and Schmidt numbers. Sensitivity analyses will be conducted for the case where the heavy fluid (NaCl and water mixture) and light fluid (ethanol and water mixture) yield an Atwood number of 0.05, which approaches the Boussinesq limit. Investigation of higher A will also be discussed.

3.2 Experimental Facility

The experimental facility consists of a cylindrical tank and annulus geometry connected by a transfer pipe. The pipe fitting nozzle is straight for the cylindrical tank, while the nozzle is smooth for the annulus as shown in Fig. 3.1. The valve that initially separates the heavy fluid from the light fluid is located off-center of the pipe, meaning that there will be asymmetry with the flow. The heights of the two fluids are adjusted depending on the Atwood number, such that the static pressure difference at the valve is zero (i.e. $\rho_H h_H = \rho_L h_L$). Although the top of the cylindrical tank is actually a free surface, it is treated as a wall for simplicity in the numerical simulation. This is safe assumption, since the free surface is far from the region of interests. Fluid properties are presented in Table 3.1, where the Atwood numbers are rounded to 0.05 and 0.10 to simplify the reporting of results. Additional details about the geometry, initial conditions, and boundary conditions can be found at Texas A&M University's Thermal-Hydraulic Research Laboratory (https://thrlab.tamu.edu/pressurized-thermal-shock-pts-facility-the-cold-leg-mixing-cfd-uq-benchmark/).

	Light Fluid	Heavy Fluid	Light Fluid	Heavy Fluid
Density (kg/m^3)	956.54	1064.7	920.0	112.3
Dynamic viscosity (Pa-s)	0.00245	0.00109	0.002867	0.001377
$(\rho_H$-$\rho_L)/\rho_0$	10.7%		18.9%	
A	0.05		0.10	

Table 3.1: Fluid properties of both Atwood number cases for buoyancy driven flow. Reprinted with permission from [2].

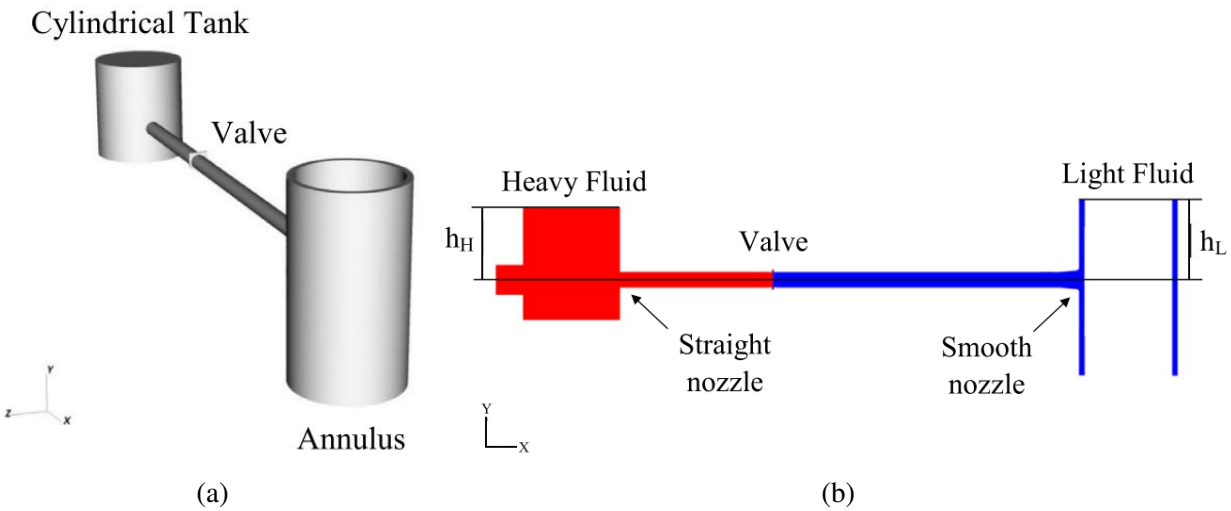

Figure 3.1: Geometry of fluid domain for (a) isometric view and (b) planar slice at z = 0 m. Reprinted with permission from [2].

3.3 Computational Domain

Similar to the validation work for HCSG, the measurement tool for the Cold Leg Mixing CFD-UQ benchmark is PIV. PIV is conducted using a match-index-of-refraction technique at the regions of interests on the symmetric plane of z = 0 m within the cold leg and downcomer [56]. Two cameras for PIV with a temporal resolution of 250 frames/s are positioned at locations in Fig. 3.6. The disc valve in Fig. 3.1b separates the heavy fluid (red) and light fluid (blue) from one another. Data acquisition is setup such that once the disc valve moves, both cameras simultaneously start to record data at what will be called time zero. At time zero, the disc opens in the position y-direction in approximation 0.028 s, where the fluids are allowed to mix. Energy loss in the closed system can be attributed to fluid mixing that dissipates potential energy and the walls that dissipate momentum. The bottom of the annulus will be filled before the cylindrical tank, since the volume of heavy fluid is larger than light fluid.

The fluid domain consists of roughly 1.5 million elements solved using N = 5 (190 million unique grid points) for A = 0.05 and using N = 7 (520 million unique grid points) for A = 0.10. This requires a time step of 2×10^{-4} s and 8×10^{-5} for A = 0.05 and A = 0.10 respectively. All

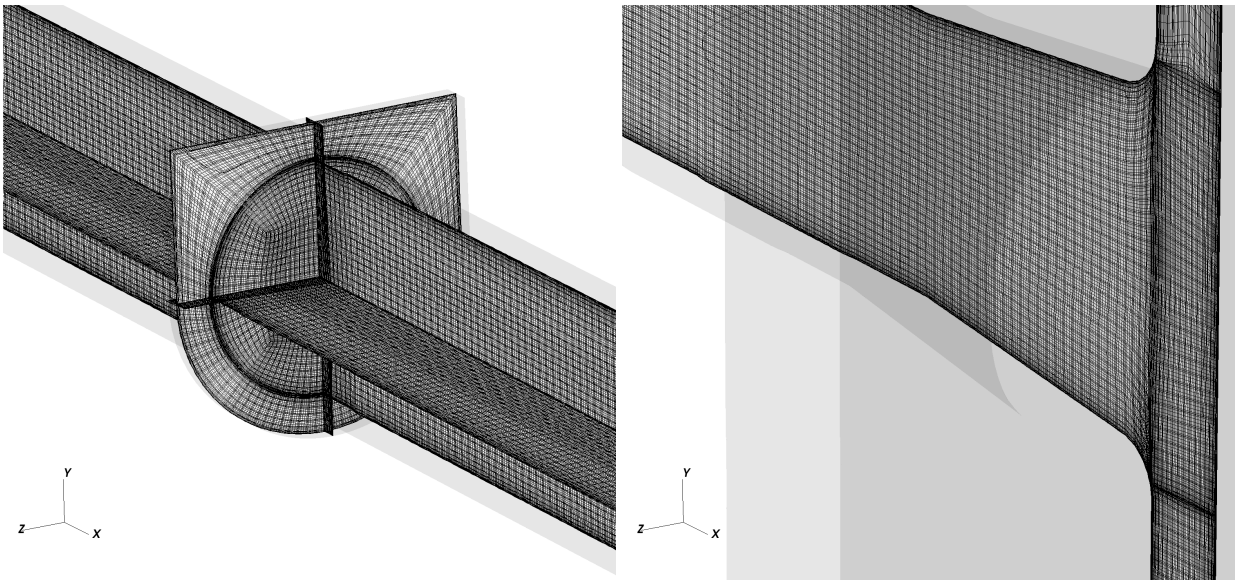

(a) (b)

Figure 3.2: GLL points of N = 5 mesh for (a) three slices at cold leg and (b) z = 0 m slice at nozzle. Reprinted with permission from [2].

boundary conditions are treated as walls, hence refinements are made such that near-wall grid points are sufficiently small. Similar to the LES grid requirements in Marin et al. (2016) and for analysis done on the HCSG, wall-normal grid sizes (y^+) are calculated using the friction velocity and viscous length [57]. On average, the first wall grid y^+ is roughly 0.1 within the cold leg and 0.3 within the downcomer. For the entire domain and length of the transience, the maximum wall y^+ only goes up to 0.7 for both Atwood numbers and occurs for a short time. This ensures that the viscous sublayer can be resolved throughout the simulation.

For LES using the spectral element method, a structured hexahedral mesh is built in ANSYS ICEM CFD with blocking, O-grids, and controlled wall-refinement to produce previously mentioned y^+ values. The mesh is exported into exodusII format and using Nek5000's exo2nek tool, element curvature, sidesets, and connectivity are imported. Aspect ratios are kept as small as possible for far-wall regions, allowing pressure iterations to average around 30 per time step for entire transience. The mesh is shown in Fig. 3.2, where elements are locally finer at regions of interest in the cold leg and downcomer than in regions where there is minimal flow movement.

3.4 Models

3.4.1 Boussinesq Approximation

For buoyancy driven flows, the Boussinesq approximation (BA) proves to be accurate for a large number of problems, as shown in [47, 58, 59]. Under the assumptions that density differences are sufficiently small, the buoyancy force can be accounted for in the momentum equation [60]. The new form of the incompressible Navier-Stokes equations that will be used is

$$\rho_0 \left(\frac{\partial \mathbf{u}}{\partial t} + \mathbf{u} \cdot \nabla \mathbf{u} \right) = -\nabla P + \nabla \cdot \mu \big[\nabla \mathbf{u} + \nabla \mathbf{u}^T \big] + (\rho - \rho_0)\mathbf{g} \tag{3.1}$$

$$\nabla \cdot \mathbf{u} = 0 \tag{3.2}$$

where the reference density ρ_0 can be arbitrarily chosen to be (ρ_H + ρ_L)/2 and ρ is the local density. The source term can be further simplified to the temperature differences times the coefficient of thermal expansion, in scenarios where buoyancy arises due to temperature differences. Since the problem under consideration is isothermal, the body force will only include density and gravity. Additionally, the full stress tensor is written out for this problem to account for variable viscosity. It is assumed both local density and viscosity are functions of concentration ϕ. Fluid properties are presented in Table 3.1 and intermediate values are calculated as such

$$\mu = \mu_L - (\mu_L - \mu_H)(\phi - \phi_L)/(\phi_H - \phi_L) \tag{3.3}$$

$$\rho = \rho_L + (\rho_H - \rho_L)(\phi - \phi_L)/(\phi_H - \phi_L) \tag{3.4}$$

where μ is the local dynamic vicsosity, ϕ is the local concentration, and the subscripts L and H indicate fluid properties of the light and heavy fluids respectively.

3.4.2 Low-Mach Navier-Stokes

Under scenarios where BA is not applicable, divergence-free conditions do not apply and a new equation-of-state must be included to close the system of equations. The low-Mach (LM) approximation formulation of the Navier-Stokes equations become suitable for this problem and is evaluated as [16]

$$\rho\left(\frac{\partial \mathbf{u}}{\partial t}+\mathbf{u}\cdot\nabla\mathbf{u}\right)=-\nabla P+\nabla\cdot\mu\big[\nabla\mathbf{u}+\nabla\mathbf{u}^{T}-\frac{2}{3}(\nabla\cdot\mathbf{u})\mathbf{I}\big]+(\rho-\rho_0)\mathbf{g} \tag{3.5}$$

$$\nabla\cdot\mathbf{u}=-\frac{1}{\rho}\frac{\mathrm{d}\rho}{\mathrm{d}\phi}\left(\frac{\partial \rho}{\partial t}+\mathbf{u}\cdot\nabla\phi\right) \tag{3.6}$$

Now, the divergence of velocity is a function of the density and concentration. Due to the linear dependence of concentration on density, the beta coefficient is known. Since pressure and velocity are not coupled with the $\mathbb{P}_{\mathrm{N}}\mathbb{P}_{\mathrm{N}}$ formulation [16], these governing equations can be solved in Nek5000 with minor modifications to the source code.

3.4.3 Concentration

For both BA and LM models, the concentration of the two fluids are calculated using the following advection-diffusion equation

$$\rho\left(\frac{\partial \phi}{\partial t}+\mathbf{u}\cdot\nabla\phi\right)=\nabla\cdot(\rho D)\nabla\phi \tag{3.7}$$

where D is the mass diffusion rate. This quantity is calculated using the molecular Schmidt number (Sc) as

$$\mathrm{Sc}=\frac{\nu}{D} \tag{3.8}$$

where ν is the kinematic viscosity based on local dynamic viscosity and local density. Since the Schmidt number is not known for the experimental fluids and the filtering method for LES does

not use a turbulent Schmidt number (Sc_t), a suitable Sc must be chosen. Finding the exact value of Sc for these mixtures is not clear-cut, although literature of pure quantities estimates Sc = 620 for coefficients of water-NaCl and a magnitude of 10^3 for water-ethanol [49, 61]. Since Sc_t adds an effective diffusion based on the eddy viscosity, the magnitude of Sc_t can be analogous to its molecular quantity since the viscosity ratio is often larger than one for turbulent flows. Literature shows that Sc_t of unity is often employed for many applications [62]. This implies that Sc = 1 may be a valid option for this type of flow since there are no issues with excessive mass diffusion with the same concentration. Therefore, sensitivity analysis of the Schmidt number will be conducted with ranges from 10^0 to 10^3, where 10^3 is roughly the actual molecular diffusivity.

3.4.4 Entropy Viscosity Method

High-order numerical approximations for the nonlinear term in the advection-diffusion equation can become very unstable, requiring the need for a large eddy diffusivity. Over-integration, spectral vanishing viscosity, and entropy viscosity method (EVM) are some recommended techniques for spectral elements when considering high Re as discussed by Malm et al. (2013) [63]. Although the effective Re for this problem is relatively low, the flow remains turbulent due to vortex shedding and the presence of Kelvin-Helmholtz instability from countercurrent flow. Moreover, the Schmidt number in this problem is in order of 10^3, so the Batchelor scale becomes three orders of magnitude smaller than the Kolmogorov length scales. This makes it impossible to resolve the gradients between the two fluids with the available computational resources. Thus, EVM by Guermond et al. (2011) is chosen such that more dissipation will be added proportional to local entropy production [64]. An upper bound is put on the following entropy viscosity

$$\nu_E(\mathbf{x}, t) = c_E h^2(\mathbf{x}) R(D_h(\mathbf{x}, t)) / \left|\left| E(u_h) - \overline{E}(u_h) \right|\right|_{\infty,\Omega} \tag{3.9}$$

where c_E is a tunable constant, h is a the local mesh size, R is a function that depends on the entropy residual D_h, E is entropy, and u_h is local velocity. Details of these functions and values can be found within [64, 65]. By increasing mass diffusion at regions of high entropy, the steep

gradients between the two mixing fluids can be smoothed to stabilize the solution at regions where the mesh is too coarse.

3.5 Taylor Microscales

Similar to Section 2.5.4 for the HCSG, it is important to ensure that the mesh distribution is appropriate and can be done by using the Taylor microscale. Equation 2.6 describes the formulation to calculate this length scale. A priori calculations using RANS are made with OpenFOAM 2.4.0 using the k-ε turbulent model [66]. Using a 3.5 million element structured mesh with the same blocking structure as Fig. 3.2, a pseudo-transient solution is developed with the finite volume method using the solver called "twoLiquidMixingFoam" with pressure-implicit with splitting of operators (PISO) algorithm [67]. This volume of fluid solver incorporates Fick's law of diffusion to calculate the mixing between the incompressible fluids, where Sc_t for this case is set to unity. The low-Re Launder-Sharma (1974) k-ε is used, since preliminary numerical tests reveal the effective Reynolds number is low [68]. The extra source terms remove the need for wall functions and allow k and ε to be solved within the viscous sublayer. Initial conditions are the same as previously mentioned, now with k and ε also being initialized to zero. The coarser mesh allows the time step to be set at 2×10^{-4} s with low courant numbers. Since the purpose of this work is sensitivity analyses for high fidelity LES, minimal verficiation was conducted on RANS.

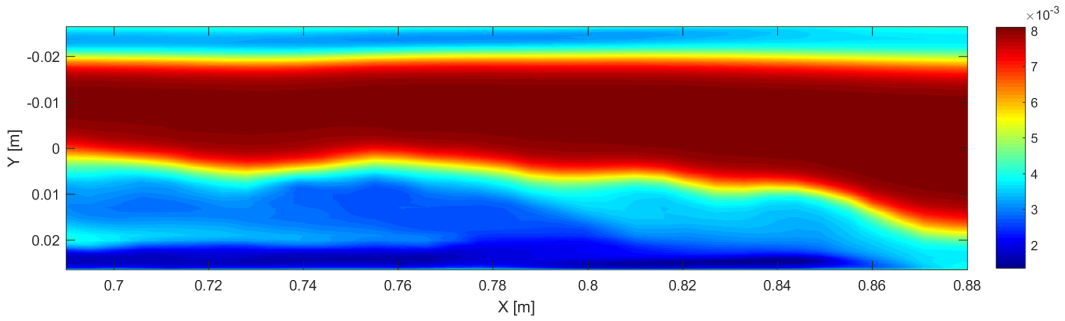

Figure 3.3: Taylor microscales (in meters) within the cold leg at t = 8 s. Reprinted with permission from [2].

Within the cold leg, velocities reach their peak when the two fluid fronts initially propogate through the transfer pipe and then begin to decay. Hence, the Taylor length scales are show in Fig. 3.3 at t = 8 s, a time roughly before the front reaches the end of nozzle and where length scales are smallest. For the downcomer, the smallest microscales appear at roughly t = 16 s. The largest ratio between local Taylor microscale and mesh size for the downcomer is 0.56 and 0.38 for N = 5 and N = 7 respectively. This means that regardless of the chosen polynomial order, the spatial discretization will resolve the large turbulent eddies and some dissipative effects as well.

3.6 Sensitivity Analyses and Validation

3.6.1 Initial Conditions

The opening of the valve described in Section 3.3 is difficult to characterize, because physics involve filling a vacuum once the disc is lifted. Sensitivity on initial conditions have been investigated to judge the long term effects on the fluid front and bulk quantities. Two-dimensional studies would be more efficient, however 2D over-predicts the growth of large scale structures compared to 3D as demonstrated by Youngs (1991) [46]. For this reason, the full 3D geometry has been numerically tested with various treatments of t = 0 s as shown in Fig. 3.4a-d.

1. IC1: Fluids are separated by a vertical plane at valve center (x = 0 m).
2. IC2: A smooth gradient for concentration of heavy and light fluids is defined across valve.
3. IC3: Fluids are separated by a slant plane to prevent fluid entrapment within valve ports.
4. IC4: Same density as IC1 but initial velocity of 1.8 m/s is specified at disc surfaces that do not touch the walls.

The reason for the large initial velocity is due to approximating its value using the height of the valve and the fast average experimental valve opening time of 0.028 s. Although IC4 represents experimental conditions most accurately, the time step must be reduced by an order of magnitude to maintain stability, making simulating the first second extremely expensive and impractical for other sensitivity analyses. Additionally, investigation of the ICs has been conducted at N = 3

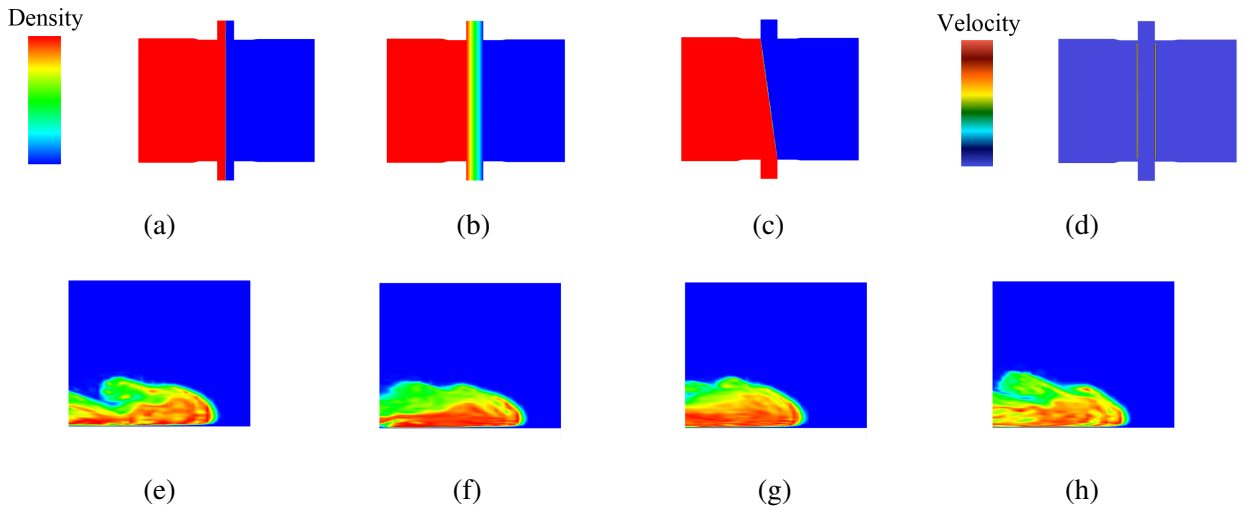

Figure 3.4: Slice of initial conditions t = 0 s at valve for density of (a) IC1, (b) IC2, (c) IC3, and velocity for (d) IC4. Slice of fluid front at t = 8 s at cold leg for densities of (e) IC1, (f) IC2, (g) IC3, and (h) IC4. Reprinted with permission from [2].

to reduce computational costs. Note that the words "density" and "concentration" will be used interchangeably for analysis within the context of the buoyancy driven flow due to their linear relationship.

The instantaneous density contours at 8 s are presented in Fig. 3.4e-h to show there are insignificant changes to location and shape of the fluid front. The location of the front of IC3 lags behind slightly, because the slanted IC has inherently more stable and has less potential energy. The wake of the front for IC2 shows less instabilities than its counterpart, because the smooth gradient of concentration suppresses the initial Kelvin-Helmholtz instabilities. Qualitatively, other locations also show almost no influence from these various ICs once the flow has developed through the cold leg and into the downcomer.

Statistics are taken to quantify whether ICs influence the bulk movement of the flow. The first several seconds after the front passes, there are clear differences in the valve between the four cases. This is due to the complexity of the Navier-Stokes equations where even small perturbations can drastically change how instabilities evolve [4]. However, these effects are eliminated once the flow reaches both tanks, and averaging from the time in Fig. 3.5a shows minor change in the bulk

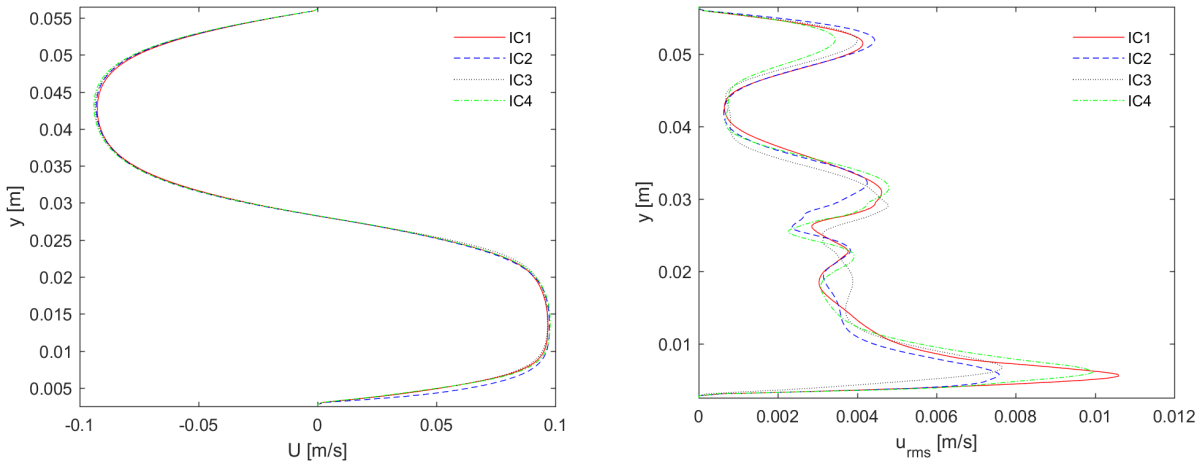

(a) (b)

Figure 3.5: Streamwise (a) mean and (b) fluctuations in cold leg at x = 0.1 m for various ICs from 7 to 17 s. Reprinted with permission from [2].

flow. The velocity fluctuations show greater differences even after time integration, which can be seen in Fig. 3.5b. The additional energy from IC4 creates greater fluctuations at the bottom of the pipe but less at the top. Generally, IC1 appears to have the closest RMS values compared to IC4. Although IC4 represents the valve physics most accurately, it is too expensive due to model a velocity of 1.8 m/s impinging onto the wall. Hence, other results for buoyancy driven flow will use IC1 due to its cheaper computational costs.

3.6.2 Time Integration of Transience

Selecting a suitable time window for a fully transient problem where system energy constantly decays irregularly is difficult. In order to obtain relatively time-independent statistics for comparing with PIV measurements, Taylor's hypothesis of frozen turbulence is used. This assumption allows the autocorrelation to be related with the two-point correlation, and the integral time scale can be computed as

$$T_{int} = \int_0^\infty B^{norm}(\tau) d\tau \tag{3.10}$$

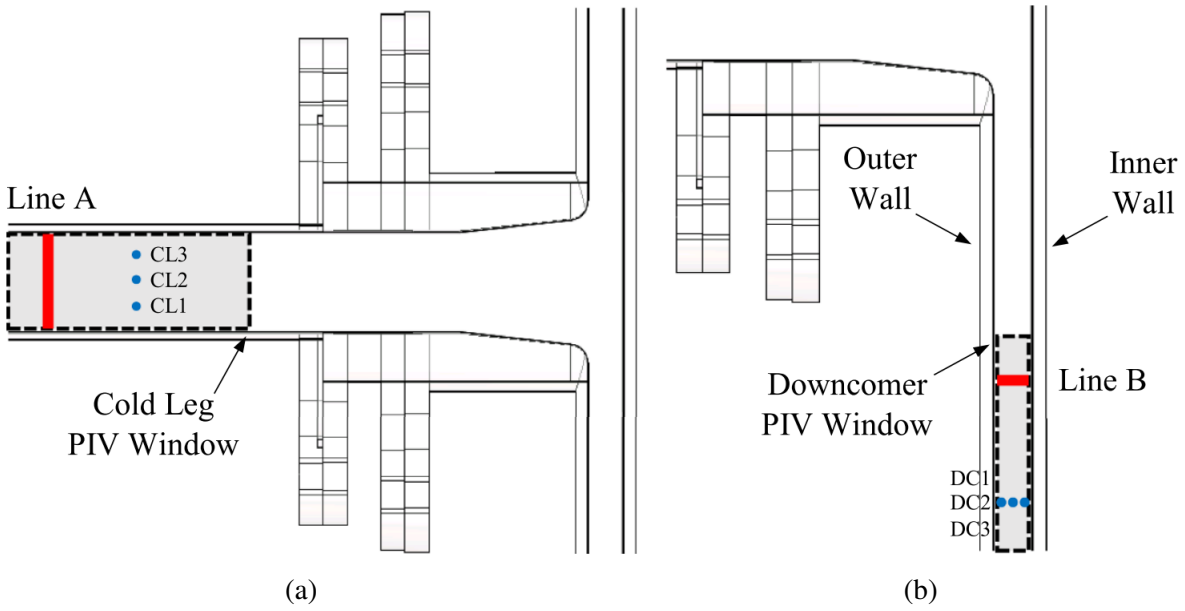

Figure 3.6: Locations of line profiles and points at (a) cold leg and (b) downcomer. Reprinted with permission from [2].

where B^{norm} is the autocorrelation at a given point in space [4]. This yields the time scale of energy within the largest eddy for a given temporal window. By computing T_{int} as the time window (ΔT) increases, time invariant data should show that the integral time scale does not change. Although this only occurs in statistically steady problems, it can still be used as a tool to justify time windows in a fully transient case.

Instantaneous monitoring points are indicated in Fig. 3.6 where cold leg points are numbered from bottom to top and downcomer points from left to right. Points are evenly spaced in fourths such that CL1 is located 1/4 of the pipe height from the bottom, CL2 is 1/2 of the height, and CL3 is 3/4 of the height. Results for different models can produce different profiles, so Fig. 3.7 is for LM Sc = 1000 since it has the most difficult convergence. It is shown that the time scale becomes relatively steady in 10 s for cold leg and in 5 s for downcomer. Therefore, it can be concluded that an averaging window of 10 s will be sufficient for gathering relatively stable statistics. Overall, it is impossible to have converged values, since the energy within the system is constantly decaying. This decay is observed in the downcomer of Fig. 3.7b, where the time scale of the largest eddy

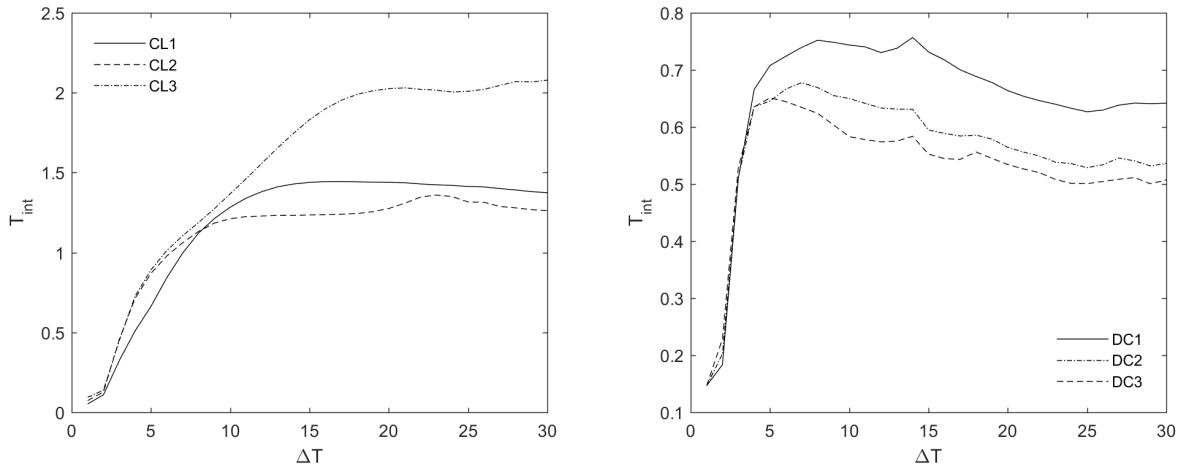

(a) (b)

Figure 3.7: Integral time scale every 1 s as statistics are taken starting from (a) 5 s for cold leg and (b) 10 s for downcomer. Reprinted with permission from [2].

decreases as ΔT increases. Generally, flow on the inner wall has a smaller time scale due to its larger velocities than the outer wall for the early transience. For the cold leg, convergence is faster in some regions than others due to variations in physics. The upper region of the pipe at CL3 has less fluctuations due to the light fluid's higher viscosity, and the slower oscillations take longer to converge. The high instabilities at the middle of the pipe at CL2 has the smallest time scale due to its quicker velocity fluctuations and smaller frequencies.

Qualitative observations are also made within the transfer pipe to describe this complex behavior to develop a greater understanding of the physics. The fluid stripe of heavy fluid undergoes interesting behavior immediately after the smooth nozzle. Countercurrent flow, instabilities, and the presence of vortex shedding at the pipe fittings create at least three transient phases, which can be observed in Fig. 3.8.

1. At t = 18 s, the countercurrent flow is stable in wake of the fluid front because of larger concentration gradients due to mixing. The fluid stripe has few oscillations and moves from attached-to-outer-wall to detached.

2. At t = 27.5 s, waves that grow from Kelvin-Helmholtz instabilities occur due to the steep

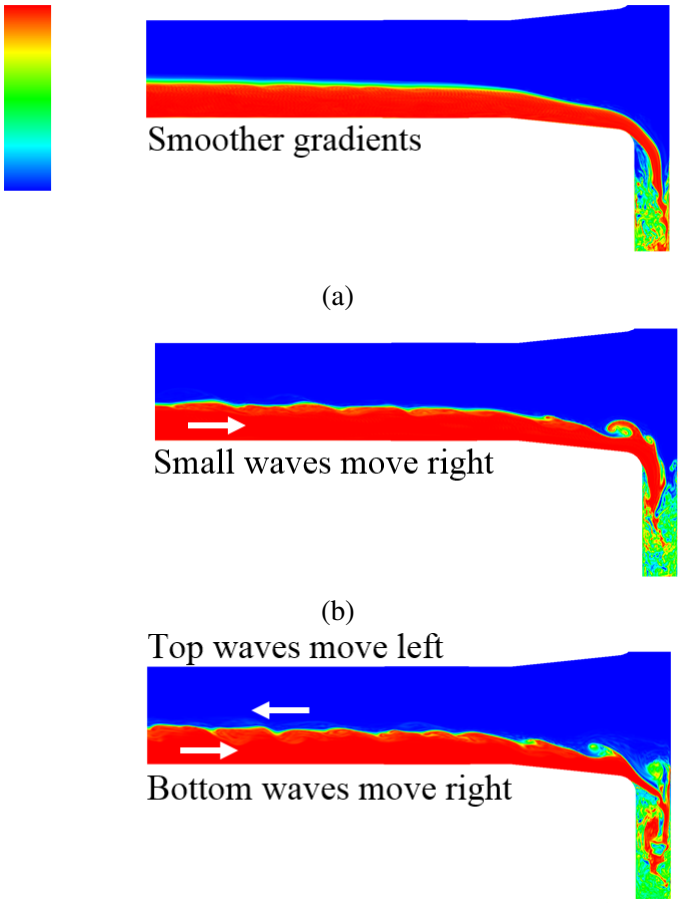

Figure 3.8: Instantaneous density contours at smooth nozzle of heavy (red) and light (blue) fluid mixtures using LM Sc = 1000 at (a) t = 18 s, (b) t = 27.5 s, and (c) t = 38.5 s. Reprinted with permission from [2].

Time window	10 to 20 s	20 to 30 s	30 to 40 s
Frequency [Hz]	0.1	0.3	1.16
Strouhal number	0.05	0.15	0.57

Table 3.2: Frequencies and Strouhal number using the spectral peak from power spectral density. Adapted with permission from [2].

concentration gradients. The fluid stripe now oscillates, constantly moving from attached to detached from the walls.

3. At t = 38.5 s, multiple waves of various wavelengths arise from propogation of vortex shedding within the nozzles. The fluid stripe now tends to detach to hit the inner wall and fluctuations more than at t = 27.5 s.

The time to transition between these phases can vary anywhere between 10 to 20 s. This reinforces the reason why the integral time scale never fully converges. These contour plots also demonstrate that these phases drastically change the velocity fluctuations entering the downcomer. More mixing occurs before the flow reaches the region of interest as oscillations grow larger within the cold leg. Hence, accurate prediction of the flow within the transfer pipe is essential for predicting physics within the downcomer.

To further demonstrate the instabilities that occur within the pipe, the power spectral density is calculated at CL1 to capture the spectral peak for various time intervals. The dominant frequencies shown in Table. 3.2 proves there is no dominant frequency for the first 10 s and has increasing frequencies for later time frames. Using the transfer pipe diameter of 5.3 cm as the reference length and the fluid front velocity of 10.8 cm/s as the reference velocity, the Strouhal numbers are shown to be as large as 0.57. For a Reynolds number of roughly 3200 (using the same characteristic values), it is shown that oscillations can be very large and grow over time due to instabilities and propogation of vortex shedding from the nozzle geometry.

3.6.3 Verification

Although many techniques have been developed for uncertainty quantification for the spectral element method, there is no generally accepted best practice method [69]. Therefore, a couple methods will be investigated for a short period of time due to computational costs of running LES. The first is an a posteriori error estimate by summing the truncation error and quadrature error from a given spectral element as done by Deville et al. (2002) [13]. The approximate form for a polynomial order discretization is

$$u_N^e(r) = \sum_{n=0}^{N} a_n^e L_n(r) \tag{3.11}$$

where L_n is the Legendre polynomial and a_n^e is the spectral coefficient. Using the last four points of the spectrum, the decaying function $[a(n)]$ can be constructed and the error estimate can be written as

$$\epsilon_{est} = \left(\frac{a_N^2}{\frac{1}{2}(2N+1)} + \int_{N+1}^{\infty} \frac{[a(n)]^2}{\frac{1}{2}(2N+1)} dn \right)^{1/2} \tag{3.12}$$

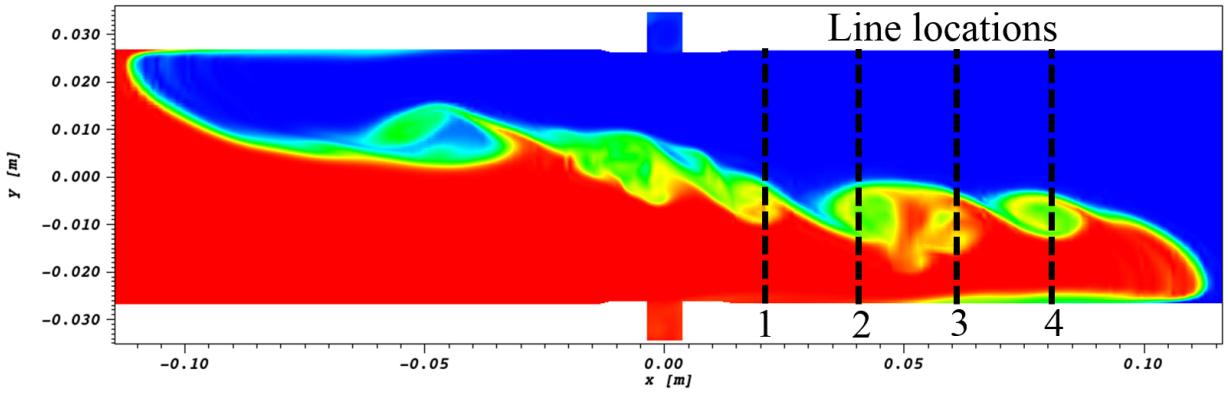

Figure 3.9: Density contour of heavy (red) and light (blue) fluids at t = 1 s with line locations at slice z = 0 m using LM Sc = 1.

The second method considered is quantifying error using p-refinement. By making assump-

tions to Oberkampf and Roy's (2010) mathematical formulation [70], Legendre polynomials can be analogous with the terms in the Taylor series expansion, allowing Equation 3.11 to take the same general form used for Richardson extrapolation as such

$$f_h = \overline{f} + g_p h^p + g_{p+1} h^{p+1} + g_{p+2} h^{p+2} + ... \tag{3.13}$$

where $\overline{f}$ is the exact solution. Therefore, the expansions for N = 5 and N = 7 can be combined for the same mesh and after dropping higher order terms, the error can be simplified to

$$\epsilon = F_s \left| f_{N=7} - f_{N=5} \right| \tag{3.14}$$

where the factor of safety F_s is equal to 3 for cases with only 2 grids. This method to quantify error will be denoted as "error bar", while the former method will be denoted as "error estimate." Now, errors can be developed for the lines shown in Fig. 3.9. Lines are chosen such that the fluid front has already passed so zeros will not be included in the window of statistics. Results are developed only for its initial transience to save computational costs, so streamwise velocities are averaged between 1.0 s to 3.0 s.

For LM Sc = 1000, errors are presented in Fig. 3.10 where red is from using the error bar and blue is from error estimate calculations. It is evident that the front of the countercurrent flow in Lines 1 and 2 have almost no error. This is because the locations of the lines are after the fluid front and does not capture its turbulent wake. On the other hand, Lines 3 and 4 still captures much of the turbulence that occurs after the front passes and, hence, both methods predict larger errors at these locations. The inflection point where concentration transitions from light to heavy is where a large source of error exists. Since the instabilities and turbulence due to density differences occur here, it is impossible to properly solve the Navier-Stokes equations and error will be larger. At near wall regions, there is more error at the bottom due to the passing of the fluid front (where concentration transitions from light to heavy), while the error at the top of the transfer pipe remains small due to concentration remaining light fluid for the entire time window. Nonetheless, errors from both

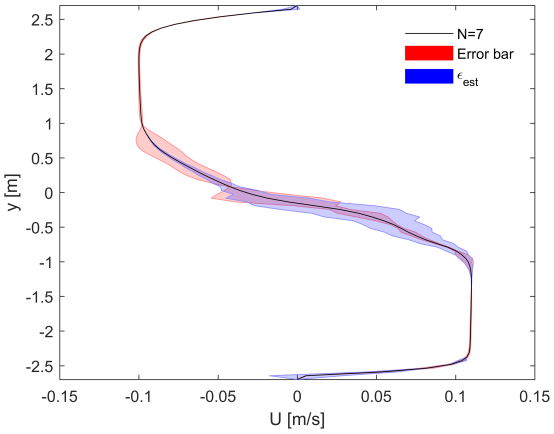

(a) Line 1

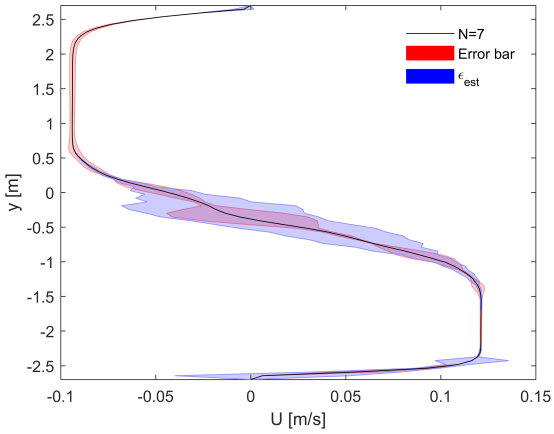

(b) Line 2

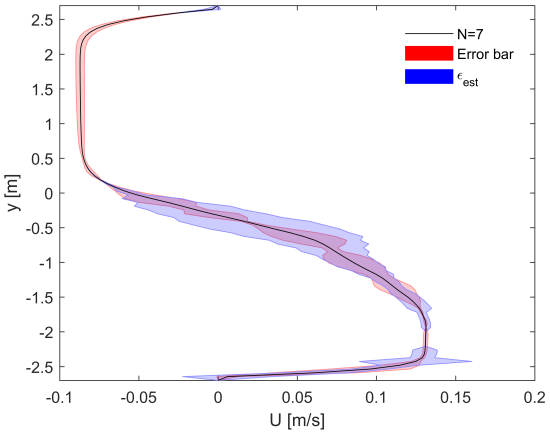

(c) Line 3

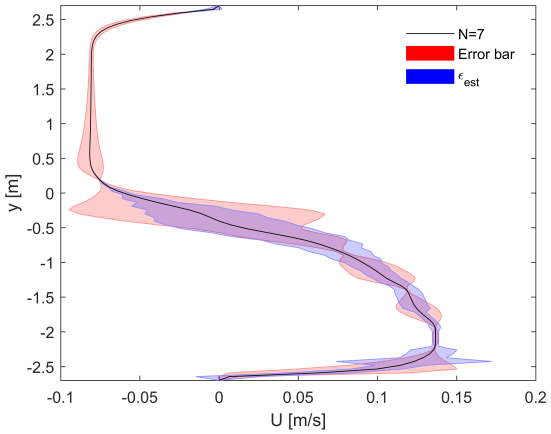

(d) Line 4

Figure 3.10: Error estimate and error bar of streamwise velocity between t = 1 s and t = 3 s for LM Sc = 1000 at lines indicated in Fig. 3.9.

methods remain relatively small everywhere except at the velocity's inflection point where the flow has instabilities due to buoyancy.

3.6.4 Cold Leg Model and Schmidt Number

Six production runs are simulated at N = 5 for 41 s, which required approximately 200 h wall clocks each using 1024 nodes, totaling 16,384 cores. The influence of varying the model and Sc is shown in Fig. 3.11 to Fig. 3.15 for the cold leg at Line A, which is located x = 0.730 m from valve center. Since the streamwise components are over 50 times larger than the secondary flow, they have much better validation than the spanwise velocity. The first 10 s averaging window for streamwise velocity matches well with PIV measurements in Fig. 3.11. In fact, even velocity fluctuations remain similar regardless of the modeling parameters as shown in Fig. 3.12. This is attributed to the time window capturing primarily the fluid front, which is dominated by buoyancy forces rather than turbulent mixing or mass exchange. For time windows starting from t = 16.5 s and t = 26.5 s, there are initially less fluctuations than PIV, but for later times LES begins to show better u_{rms}. This implies that the experiment may transition to Fig. 3.8c sooner than LES because of possible difficulty in predicting the onset of instability within the transfer pipe. Differences in RMS will have an impact on the mean, because larger RMS means more energy will be dissipated from the closed system. Fluctuations also have an impact within the downcomer, which will be observed in the next section. Regardless, the cold leg's inflection point for the mean moves in the positive y-direction at the same rate as the experiment.

The effects of the diffusive parameter for streamwise velocity are evident in the cold leg. For smaller Sc, RMS values are damped for later time windows. Between t = 26.5 to 36.5 s, fluctuations gradually increase from Sc = 1 to Sc = 1000 for LM. This trend correlates with the hypothesis that less mass diffusion creates greater instabilities, which causes larger velocity fluctuations. On the other hand, the influence of buoyancy model is not as clear. Generally, RMS streamwise velocity is better when using LM compared to BA, but is not as definitive as the effect of Sc on the simulations.

The mean spanwise velocities has less trends as magnitudes of these values tend to be extremely low in Fig. 3.13. As mentioned before, there is better correlation for the first averaging window due

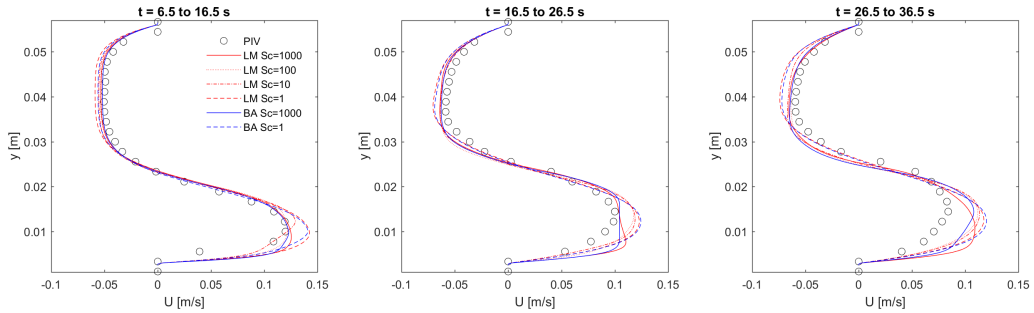

Figure 3.11: Sensitivity comparisons of cold leg at Line A for streamwise mean. Reprinted with permission from [2].

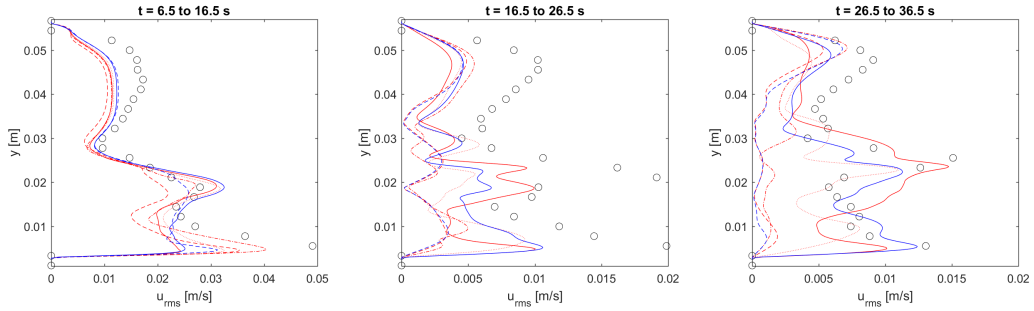

Figure 3.12: Sensitivity comparisons of cold leg at Line A for streamwise fluctuations. Reprinted with permission from [2].

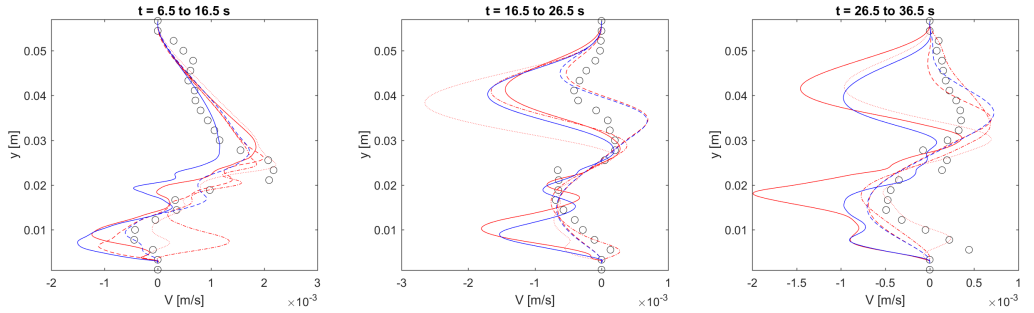

Figure 3.13: Sensitivity comparisons of cold leg at Line A for spanwise mean.

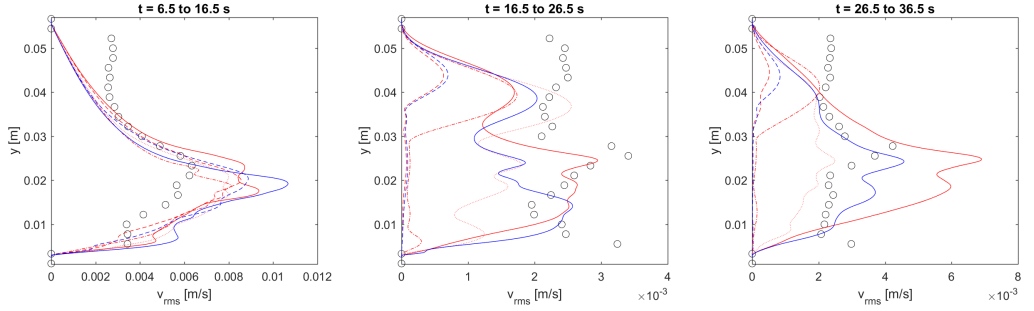

Figure 3.14: Sensitivity comparisons of cold leg at Line A for spanwise fluctuations.

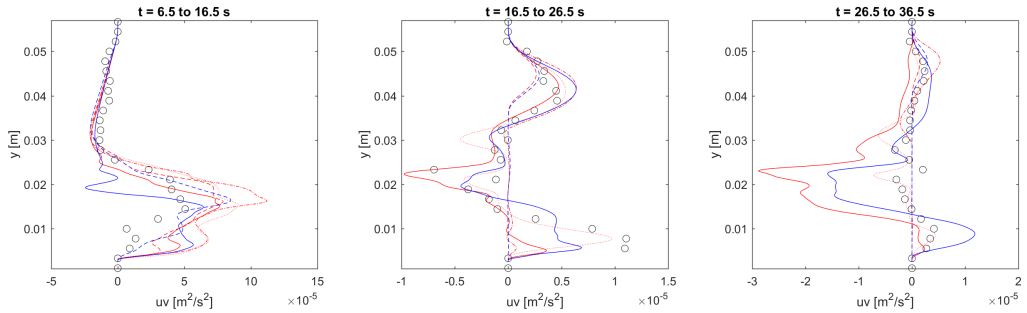

Figure 3.15: Sensitivity comparisons of cold leg at Line A for shear Reynolds stress.

to the buoyancy-dominant characteristics than later time frames. For later times, the magnitude of PIV appears to hover around 0.5×10^{-3}, whereas the simulations tend to be roughly twice as large. The shape is not as correlated for later times and is due to the transient nature of the problem. If the measurement line is shifted even a centimeter (not shown), the shape of spanwise velocities change drastically, whereas the streamwise direction had less variation. The Schmidt number appears to have less improvement on the spanwise velocities and, in fact, appears to be better for lower Sc. However, this is fortuitous and happens to be the result of additional mass diffusion decreasing velocities in general. Proof can be observed in Fig. 3.14 where RMS of the spanwise velocity is nearly zero for low Sc. One important feature to notice is the lack of fluctuations at the top of transfer pipe for LES. This distinct difference in RMS could be the source of discrepancies. The shear Reynolds stress in Fig. 3.15 also show the same relationships and it is obvious that the Reynolds stress is larger and arguably better for high Schmidt numbers.

3.6.5 Downcomer Model and Schmidt Number

The downcomer physics are much more complex, because it heavily depends on the flow coming from the smooth nozzle into the annulus. Line B is located at y = -0.161 m from the valve center and comparisons in Fig. 3.16 and Fig. 3.17 have different trends than the cold leg. Whereas the streamwise fluctuations v_{rms} trend to match well with PIV for cases at Sc = 1000, mean velocities vary more for the first time window. The first 10 s window for streamwise averages has a different shape than PIV, but tends to readjust itself when waves begin to develop within the transfer pipe at

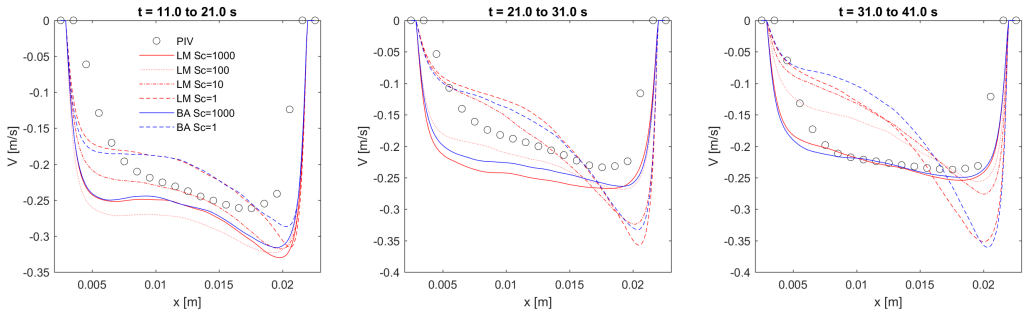

Figure 3.16: Sensitivity comparisons of downcomer at Line B for streamwise mean. Reprinted with permission from [2].

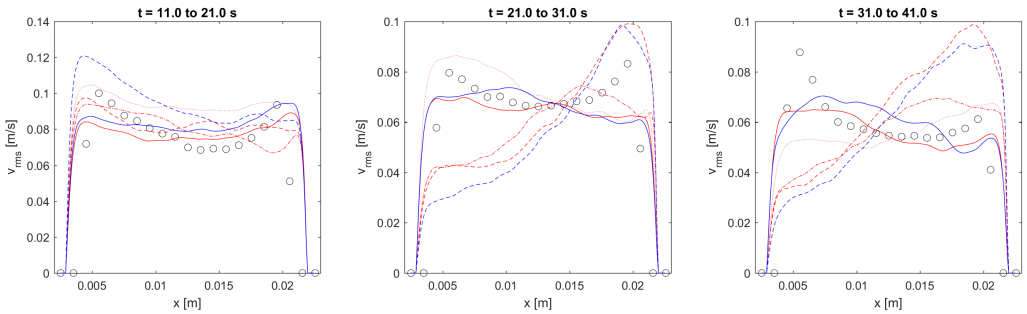

Figure 3.17: Sensitivity comparisons of downcomer at Line B for streamwise fluctuations. Reprinted with permission from [2].

later times. The RMS tends to be close to PIV regardless of the time window. Again, experiments show qualitatively that physics are more similar to Fig. 3.8c earlier than LES, enforcing the idea that resolving the tight gradients of the molecular Schmidt number is essential for this type of flow.

The Schmidt number plays a huge role for the downcomer in the bias towards the inner wall. Sc = 1 reduces the amount of momentum mixing due to greater mass diffusion, allowing the flow hug the inner wall. Less mass diffusion means the presence of instabilities and wave propogation that causes greater turbulence above the region of interest, leading to a more evenly distributed velocity profile. This trend is noticable in both average and RMS streamwise velocity. Similar to the cold leg, the downcomer shows that BA can do quite well in predicting flow at A = 0.05, even with the assumption of incompressibility.

The spanwise velocity tends to be overpredicted at early times but becomes better at later

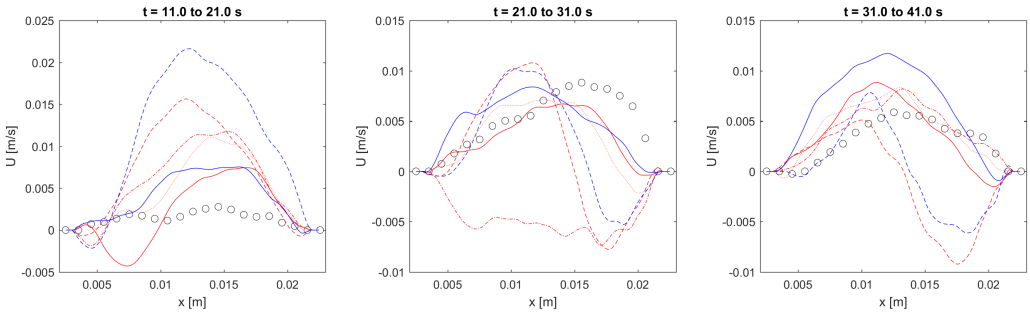

Figure 3.18: Sensitivity comparisons of downcomer at Line B for spanwise mean.

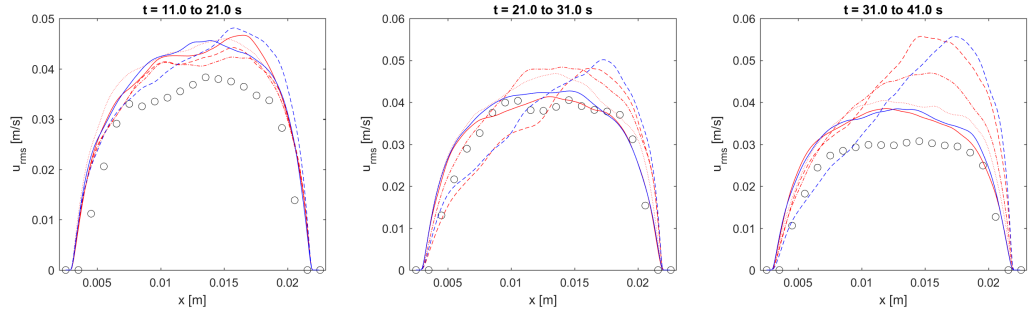

Figure 3.19: Sensitivity comparisons of downcomer at Line B for spanwise fluctuations.

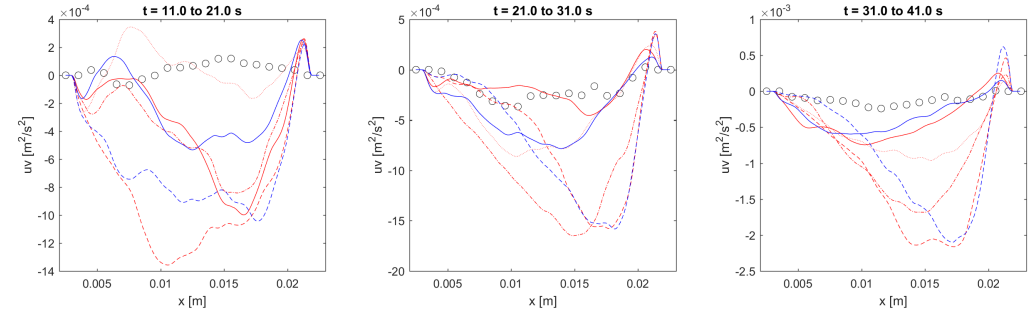

Figure 3.20: Sensitivity comparisons of downcomer at Line B for shear Reynolds stress.

times in Fig. 3.18. This is most likely due to difficulty in predicting the fluctuations for the initial transience. Like the streamwise component, the secondary flow in Fig. 3.19 stays relatively the same for the entire duration of the simulations for high Sc. The large mixing upstream in the smooth nozzle causes the RMS to be flatter. For the shear Reynolds stress in Fig. 3.20, results prove to be better for higher Sc than lower Sc. Although not measured, the spreading in the z-direction (not shown) becomes an important factor for the secondary flow as well. Magnitudes are comparable, if not larger, than those in the x-direction, and future work should consider capturing all secondary flow components to improve validation.

Overall, validation results reveal the challenges of predicting transient physics in buoyancy and the importance of capturing fluctuations for this type of flow. It is recommended for future simulations to make refinements at regions with tight concentration gradients at the center of the transfer pipe to minimize numerical diffusion. Additional sensitivity tests will be investigated in the next sections to uncover other reasons why downcomer simulations were not as accurate compared to PIV.

3.6.6 Nozzle Geometry

The downcomer is analyzed by investigating the effect of junction geometry between transfer pipe and annulus. Solutions with LM Sc = 1000 for meshes of the same structure as Fig. 3.2 are made for a straight nozzle geometry as shown in Fig. 3.21. An interesting set of physics occurs for the straight fitting where the flow hits the inner wall immediately, causing mixing start earlier. Moreover, vortex shedding that is nearly non-existent in the smooth nozzle appears quickly for the straight nozzle case after the annulus begins to fill. Instabilities that occurs within the pipe become fundamentally different at early stages of the flow, although this is not the focus of the study.

Since the region of interest is before the flow reaches the geometrical changes, velocity profiles for the cold leg are identical for the first 10 s averaging window. Only the downcomer has different behavior due to earlier mixing and exhibits momentum loss due to hitting the inner wall immediately. This effect is observed in Fig. 3.22. Mean velocities can deviate up to 20% between the two geometries. Moreover, the bias towards the inner wall is less pronounced due to enhanced

(a) (b)

Figure 3.21: Geometry of (a) smooth fitting of experiment and geomtery of (b) straight fitting used for sensitivity analyses. Reprinted with permission from [2].

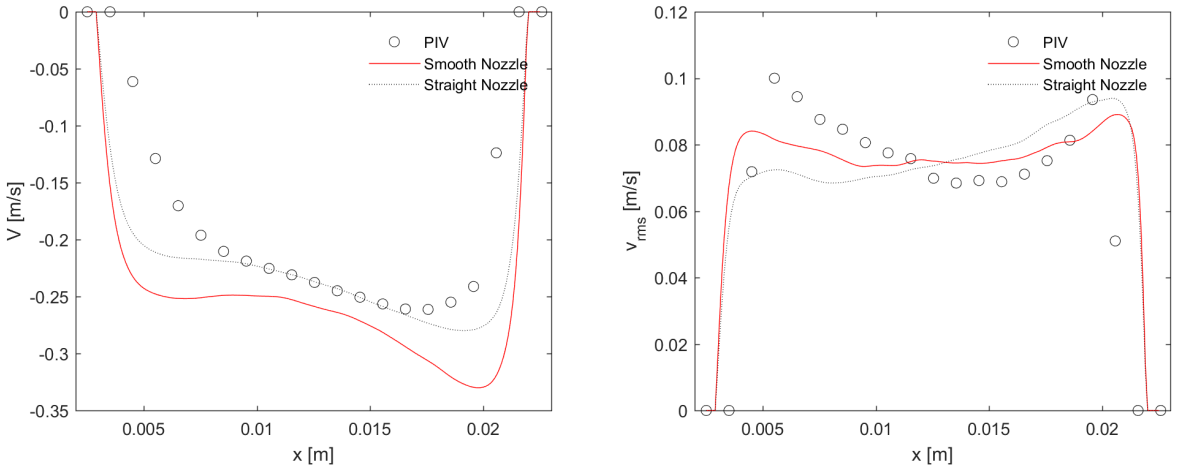

(a) (b)

Figure 3.22: Streamwise velocity for (a) mean and (b) RMS for smooth vs. straight fitting in the downcomer at Line B between 11.0 to 21.0 s. Reprinted with permission from [2].

mixing upstream of the measurement line. RMS velocity is roughly the same with slightly more bias towards the inner wall. Generally, the first time frame matches better with PIV measurements. However, this benefit only appears for the first 10 s time window, and the straight nozzle begins to have an adverse effect at later times leading to increases in percent error. An additional sensitivity test was conducted for small kinks in smooth nozzle, however negligible changes in mean quantities are present within the downcomer for the first time window. This is evidence that the vortex shedding is not the source of discrepancies, and another form of physics is missing.

3.6.7 Perturbation Sensitivity

Although it was demonstrated that statistics in the cold leg show little change with different ICs, the more turbulent downcomer can still be sensitive to small changes in ICs. Even the Lorenz equations can exhibit extreme sensitivity to 0.001% perturbations [4]. Unfortunately, testing IC4 at N = 5 is too expensive because of the small time step required for stability, so another technique must be investigated. During the quick opening of the valve, it is reasonable to assume some residual energy exists around the supports that hold the fittings. Hence, adding some type of perturbation becomes a viable sensitivity test. Solutions are initiated from LM Sc = 1000 at 9.0 s, since at this time the fluid front has not reached nozzle. Random perturbations are added in the smooth nozzle with TKE of 5% and 10% at the region shown in Fig. 3.23. This percentage is based on the average speed of the front, which is documented in Table 3.3. Using the mean velocity in the downcomer, the TKE percentage would be roughly 2% and 4% respectively.

Observations of these different scenarios qualitatively show the small perturbations do not change the fluid front nor the instabilities that occur in this region. In fact, no definitive conclusion can be made from analyzing videos of the flow from various angles, since the perturbations are very small. However, quantitative comparisons in Fig. 3.24 actually show that there is a significant change in mean quantities. Like previous geometric sensitivity tests, there is momentum loss due to additional mixing upstream from Line B. Consequently, the RMS values are smaller for 5% perturbations than without them. The case with 10% perturbations appear to be too large and have a negative influence on the percent error for both mean and RMS quantities. These results prove

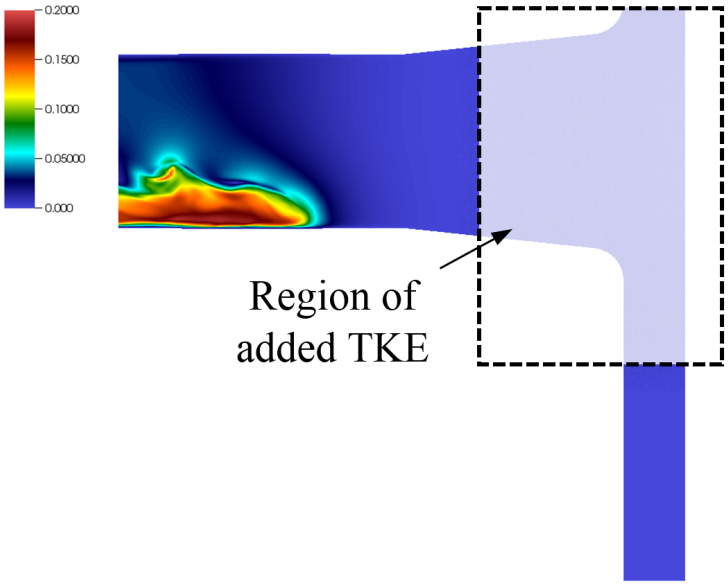

Figure 3.23: Location of added energy at t = 9 s, before the front reaches nozzle, for sensitivity analysis, superimposed on the contour of velocity magnitude [m/s]. Reprinted with permission from [2].

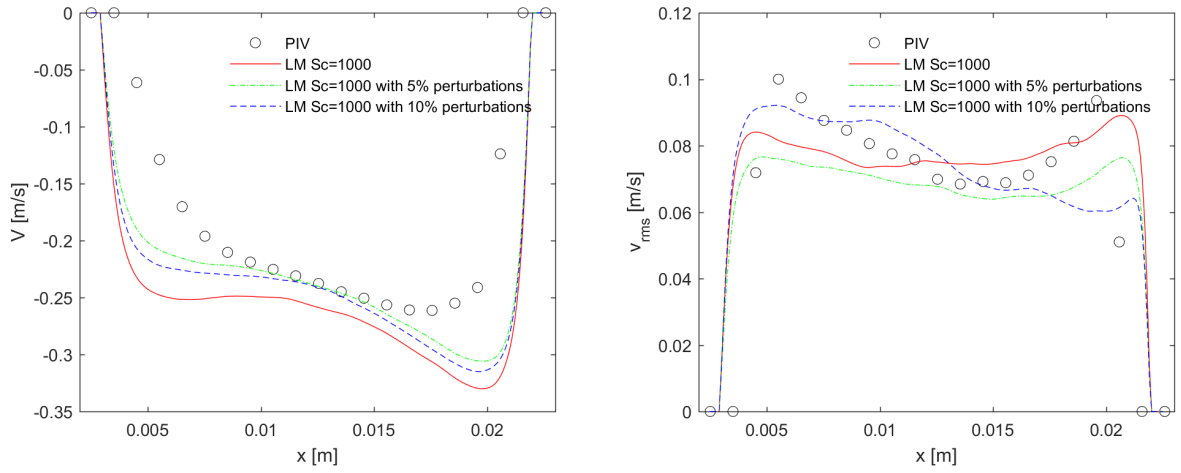

(a) (b)

Figure 3.24: Streamwise velocity for (a) mean and (b) RMS for cases with and without perturbations in the downcomer at Line B between 11.0 and 21.0 s. Reprinted with permission from [2].

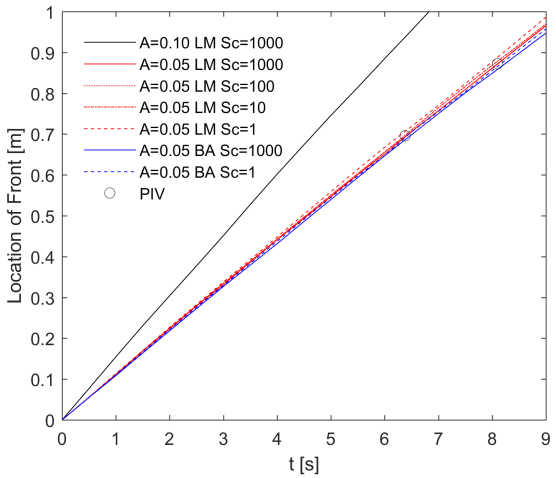

Figure 3.25: Temporal evolution of fluid front with entrance and exit times of PIV for A = 0.05. Reprinted with permission from [2].

that small residual energy due to the valve opening must be present, which has a large influence on downcomer quantities. Also, it is shown that the perturbations are very small compared to the energy in the bulk flow.

3.7 Additional Analyses

3.7.1 Atwood Number

The density's furthest point in the flow every 0.5 s is tracked for all simulations in Fig. 3.25. For PIV, the velocity is used to track the time when the front enters and exits the frame of interest. Despite minimal data due to difficulty in experimentally tracking the fluid front, it can be concluded that LM cases match with PIV better than BA cases. This is the result of having a greater fluid resistance when BA uses the reference density, which is larger than light fluid, rather than the local density.

Using linear regression on Fig. 3.25, the velocity front is computed for the chosen models and Atwood numbers in Table 3.3. When the Schmidt number is small, the fluid front is faster while when there is little mass diffusion, there is more resistance for the front to evolve. This trend is prevalent when going from Sc = 1 to Sc = 10, and less change is observed when Sc gets closer to

A	Model	Sc	Velocity of Fluid Front (cm/s)
0.05	LM	1000	10.8336
0.05	LM	100	10.8459
0.05	LM	10	10.9016
0.05	LM	1	11.0438
0.05	BA	1000	10.6792
0.05	BA	1	10.7671
0.10	LM	1000	14.8250

Table 3.3: Average fluid front speed using the slope of Fig. 3.25 where all R^2 values are greater than 0.999. Reprinted with permission from [2].

the molecular magnitude of 1000. BA predicts slower velocities than their LM counterparts. When analyzing every case, the maximum difference between velocities only goes up to 3%, hence it can be concluded that the velocity of the fluid front is not heavily affected by changing these fluid parameters and models.

Transience makes it difficult to compare results of different Atwood numbers. Still, the fluid front speed can be used as a reference for comparing the stage the system is in. For example, the ratio between velocities (for A = 0.05 and A = 0.10 with LM Sc = 1000) of 1.37 means that times at 10.0 s for A = 0.05 should show similar characteristics as results at 13.7 s for A = 0.10.

Using this analogy, statistics with different Atwood numbers are compared for the time window between 13.0 and 37.0 s for A = 0.05 with the time window between 9.5 and 27.0 s for A = 0.10 in Fig. 3.26 for LM Sc = 1000 in the cold leg. All values are normalized by the fluid front velocity (which will be denoted as U_{ff}) and proves to be a good normalization factor when analyzing the inflection point of the mean streamwise velocity. The additional buoyancy forces with A = 0.10 actually decreases the gradients near the wall, perhaps due to different vortex shedding effects. The fluctuations close to the wall are expectedly higher for the greater Atwood number but appears to be roughly the same in other regions of the pipe.

Although the magnitude of the spanwise velocities are low, the overall shape is very similar for both A. In fact, the top of the transfer pipe shows almost identical normalized magnitudes for spanwise mean and RMS. Because of the larger streamwise RMS for the higher A, the shear Reynolds

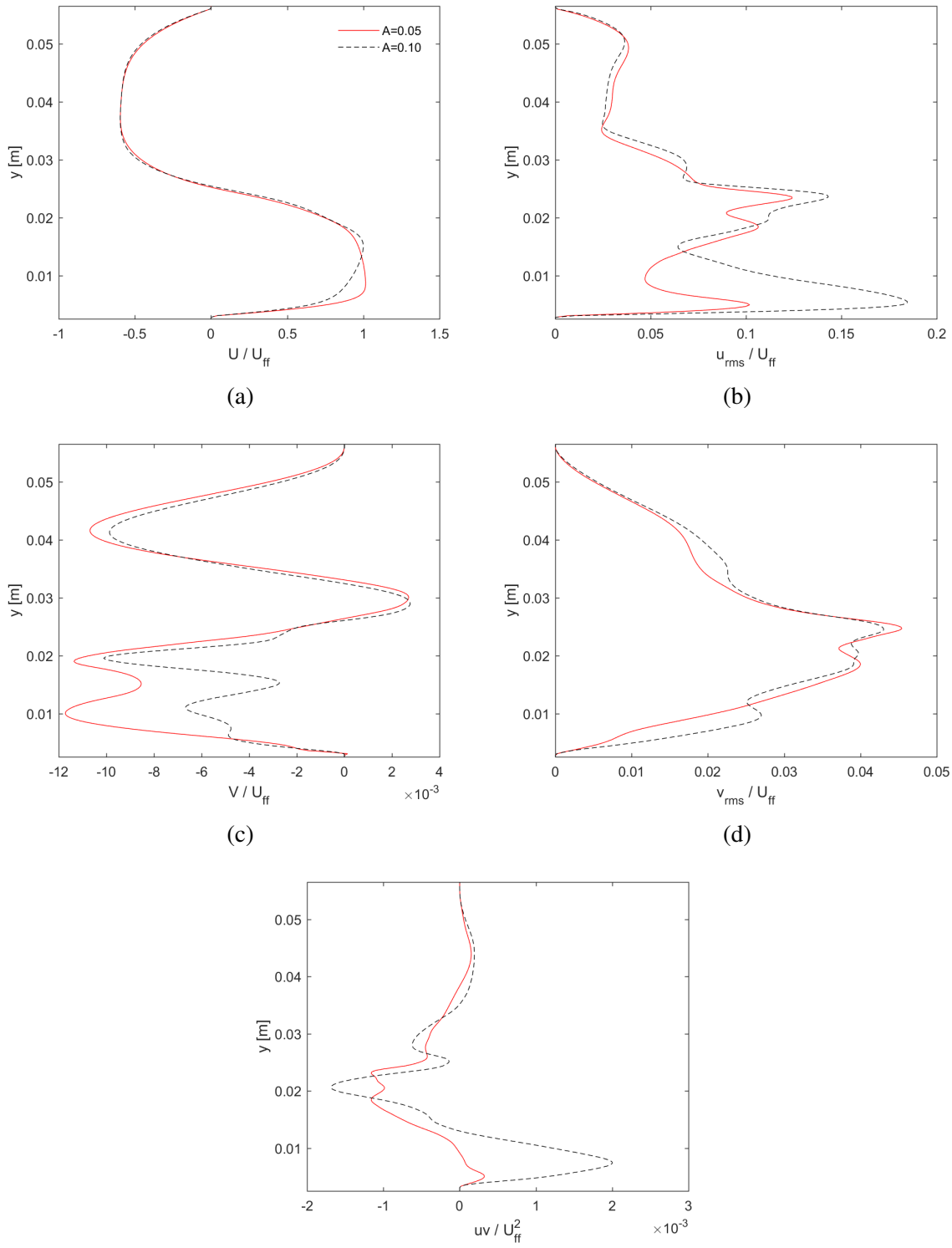

Figure 3.26: Velocity (a) streamwise mean, (b) streamwise RMS, (c) spanwise mean, (d) spanwise RMS, and (e) shear Reynolds stress for cold leg at Line A for both Atwood numbers, normalized by fluid front, for times mentioned previously. Reprinted with permission from [2].

stress is also larger at this wall region. However, other regions of the flow show similar characteristics, giving confidence that the time window of comparison is accurate and the characteristic velocity is reliable.

The downcomer for LM Sc = 1000 is also compared for the time window between 13.0 and 37.0 s for A = 0.05 with the time window between 9.5 and 27.0 s for A = 0.10 in Fig. 3.27. Here, it is less clear whether U_{ff} is a good characteristic velocity. The streamwise flow appears to be lower for the higher A, most likely due to loss of momentum from greater mixing upstream of the measurement line. Streamwise RMS shows bias towards the outer wall for A = 0.10, while the bias favors the inner wall for A = 0.05. Since the initial velocity is higher for A = 0.10, the flow resembles the physics when changing the geometry in Fig. 3.21 and exhibits hitting the inner wall much sooner. This is why the profile appears to have a greater bias towards the inner wall than the lower Atwood number.

There is less variation for the spanwise velocity, and little can be said about changing A since the magnitudes are so low. For this reason, there is more variation for the shear Reynolds stress in the center region for Line B. Overall, the sensitivity of the downcomer due to nozzle effects makes it difficult to predict how physics will change with varying Atwood numbers. Nonetheless, the general shapes are captured and analytical equations could be made for predicting flows at other Atwood numbers.

3.7.2 Proper Orthogonal Decomposition

As mentioned in Section 2.6.4, POD can be a useful method to study the transient nature of the flow. Instantaneous values in the entire domain are saved every 0.02 seconds, meaning every 10 seconds will be composed of 500 snapshots. This is obviously too small to ensure independence on the number of fields, but it has already been established that this fully transient problem will never truly reach convergence. Nonetheless, POD can provide further insight into the various phases the flow undergoes as waves develop within the transfer pipe as shown in Fig. 3.8. Now, it can be quantified how the waves propogates into their respective energetic modes.

The first mode in Fig. 3.28 and Fig. 3.29 represents the average velocities for the x- and y-

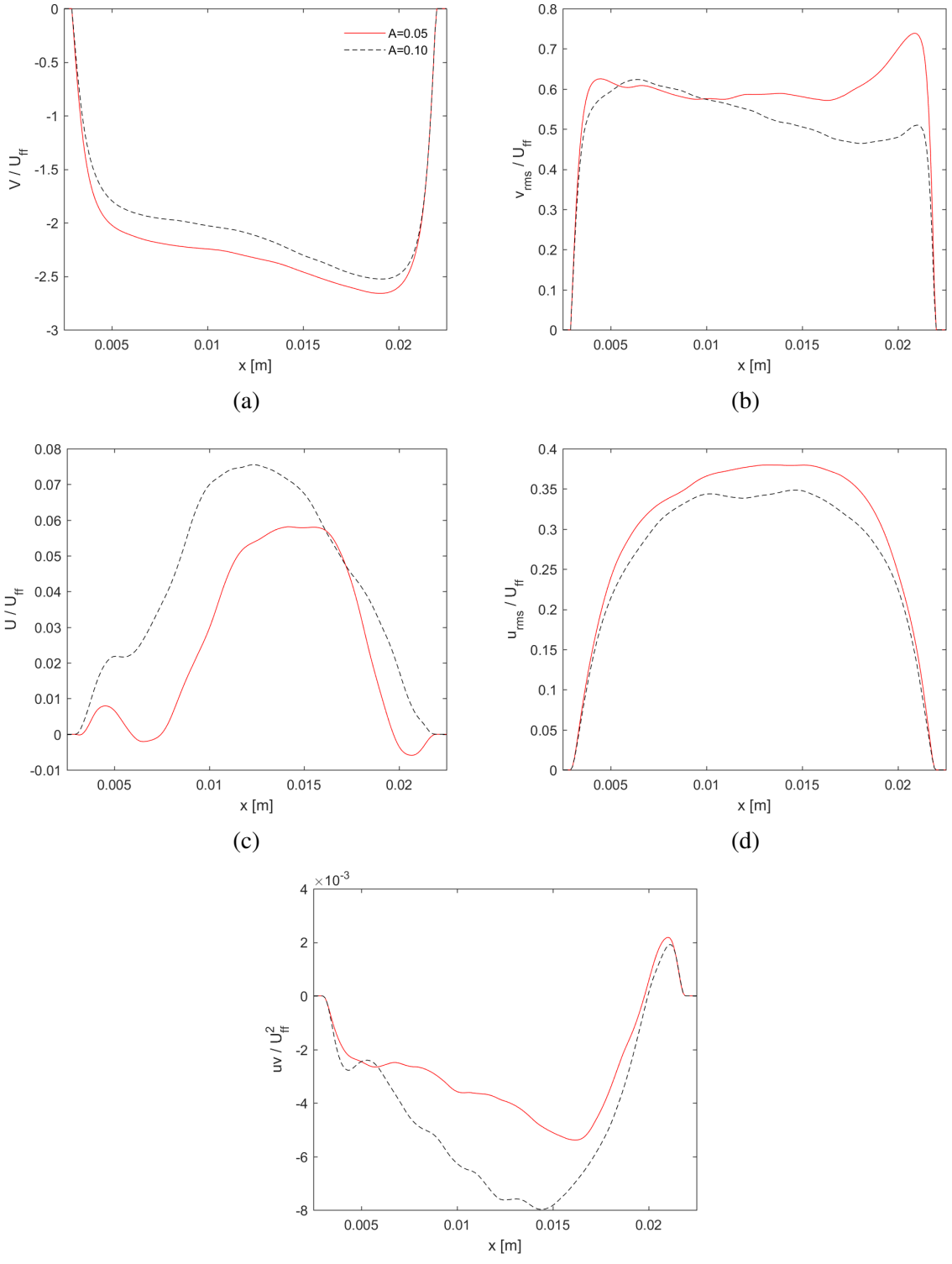

Figure 3.27: Velocity (a) streamwise mean, (b) streamwise RMS, (c) spanwise mean, (d) spanwise RMS, and (e) shear Reynolds stress for downcomer at Line B for both Atwood numbers, normalized by fluid front, for times mentioned previously. Reprinted with permission from [2].

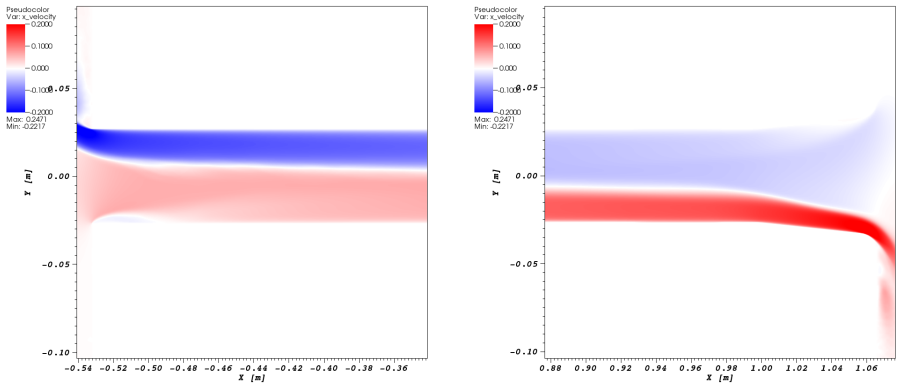

(a) 11 to 21 s.

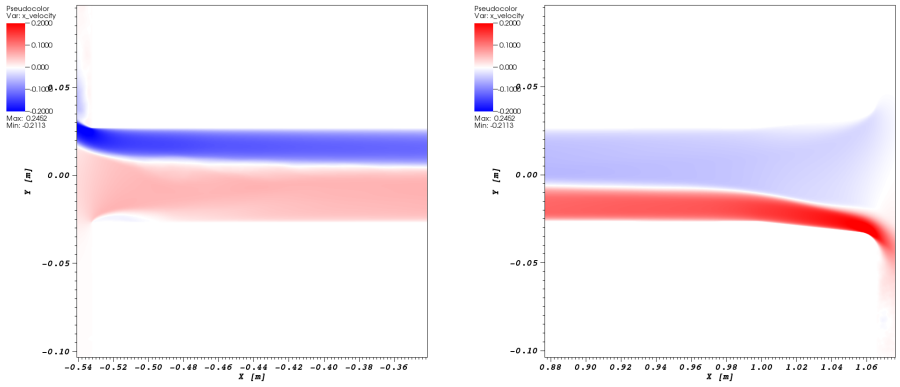

(b) 21 to 31 s.

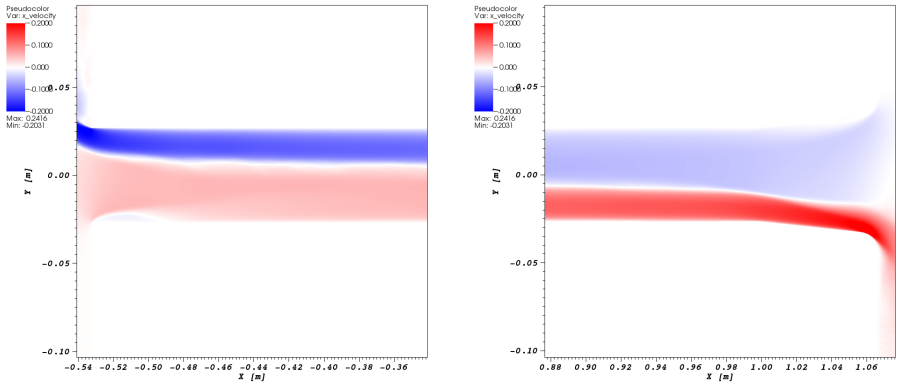

(c) 31 to 41 s.

Figure 3.28: POD mode 1 x-velocity at both (left) straight nozzle connected to tank and (right) smooth nozzle connected to annulus between various time windows.

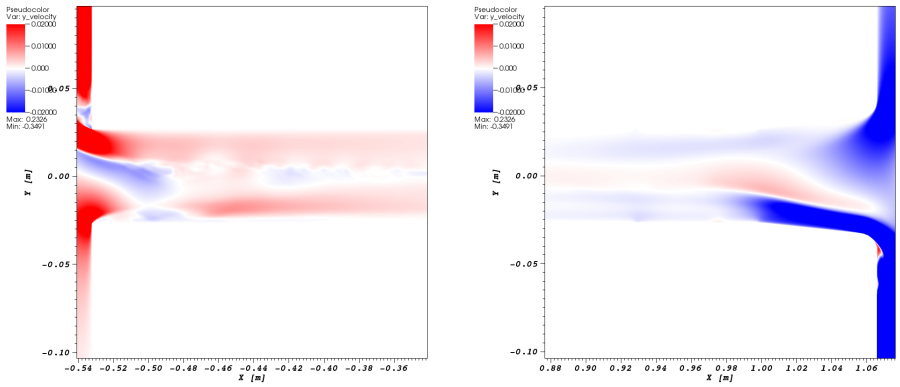

(a) 11 to 21 s.

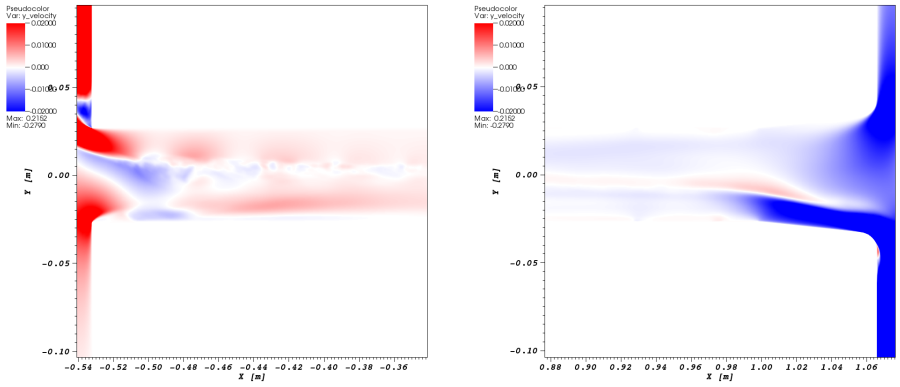

(b) 21 to 31 s.

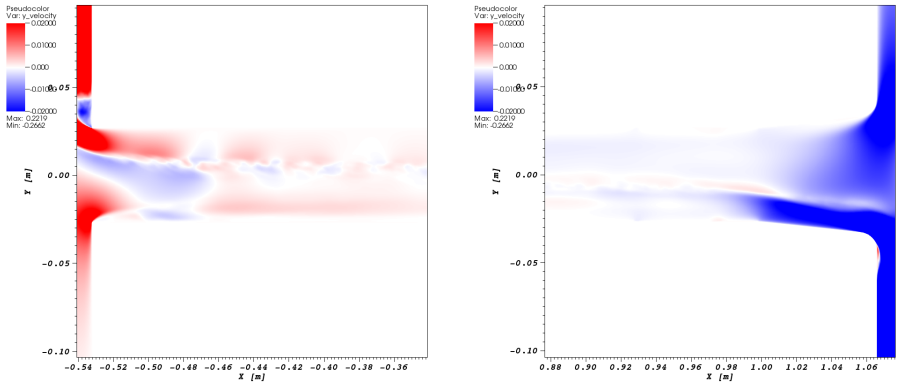

(c) 31 to 41 s.

Figure 3.29: POD mode 1 y-velocity at both (left) straight nozzle connected to tank and (right) smooth nozzle connected to annulus between various time windows.

direction respectively. It is observed that there is no discernable difference for the streamwise flow. There is a small decay in the primary velocity that has been quantitatively shown previously for validation. For the spanwise y-velocity, it is easy to tell there is a lack of convergence in statistics, because there are traces of vortex shedding exists in the straight nozzle region. Comparisons between different 10 s time averages show that there are more waves later in the time than earlier, a physical observation mentioned previously. Since the magnitudes have little deviation, it can be said the average transfer of mass from both regions has almost no variation for this 30 s time of interest.

The second mode in Fig. 3.30 reveal greater differences between the time intervals. Within the straight nozzle, the mean streamwise velocity has the largest magnitude in 21 to 31 s compared to the other times. In the first 10 s time frame, there is more energy in the negative direction as the dominant force is the initial vortex shedding. In the last 10 s, this characteristic swaps and the positive direction begins to have a larger magnitude. This feature represents the waves from the smooth nozzle influencing the flow within the straight nozzle. In Fig. 3.31, the spanwise velocities also show larger magnitudes from 11 to 21 s compared to later times. For these contours, it is more interesting to look at the smooth nozzle where the last time window shows evidence of vortex shedding and wave propogation. This distinctingly shows the time frame where the waves from one end of the transfer pipe affects the other end.

The third mode in Fig. 3.32 shows similar features as the second mode except the magnitude of energy is less, and the switches between negative and positive are more frequent. This is a reasonable consequence of the waves and instabilities that occur where turbulent eddies break down energy to higher modes. It is observed that the first time window in the smooth nozzle still has few structures, representing its smaller amount of turbulence compared to the straight nozzle. This can also be observed in the spanwise mode in Fig. 3.33, where traces of energy can only be found in the smooth nozzle starting from the 21 to 31 s window. Compared to the second mode, this contour reveals much more frequent sign changes in energy content and shows the waves from vortex shedding has multiple frequencies associated with it.

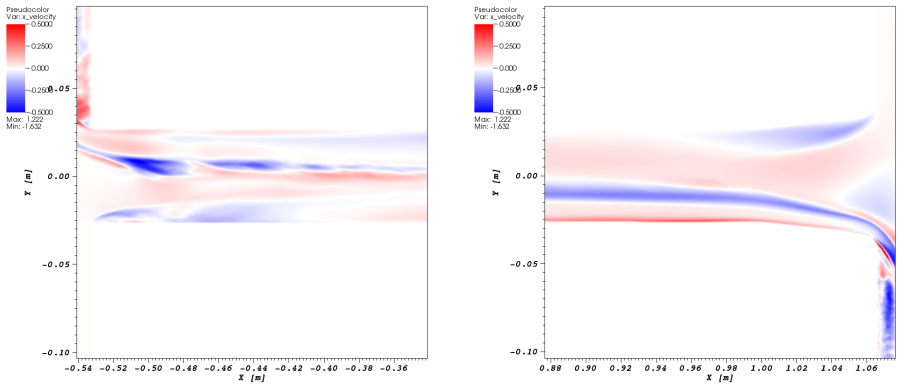

(a) 11 to 21 s.

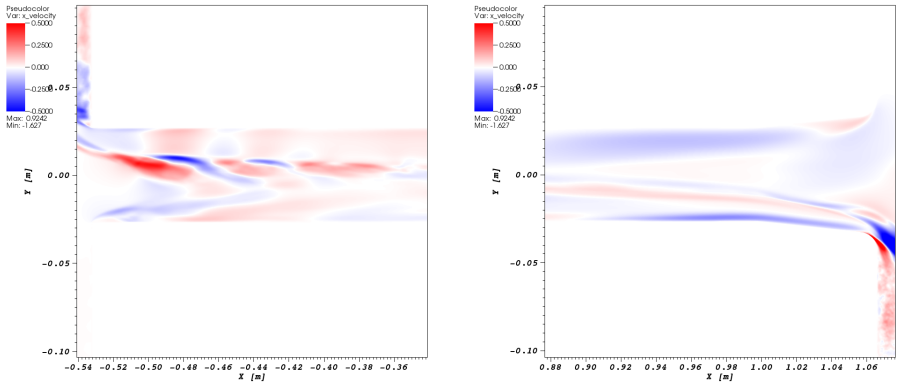

(b) 21 to 31 s.

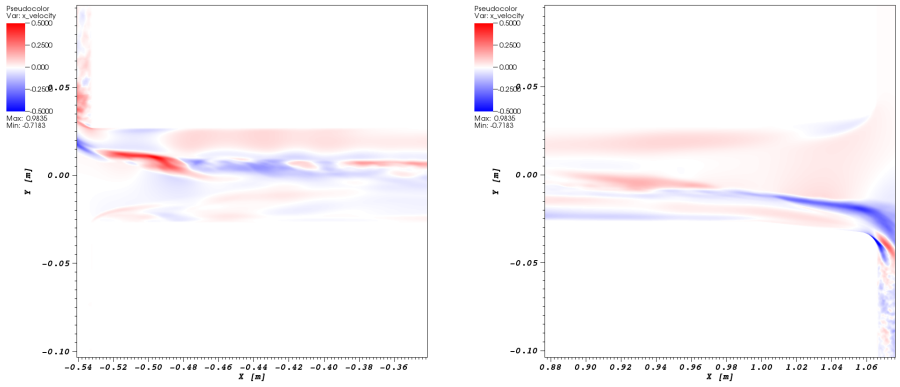

(c) 31 to 41 s.

Figure 3.30: POD mode 2 x-velocity at both (left) straight nozzle connected to tank and (right) smooth nozzle connected to annulus between various time windows.

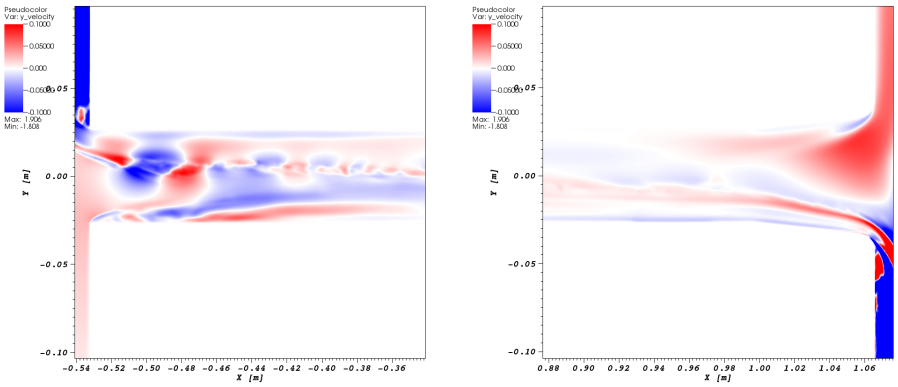

(a) 11 to 21 s.

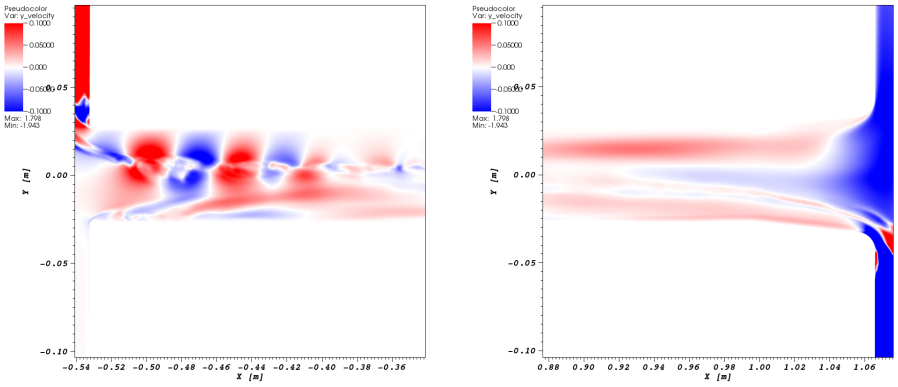

(b) 21 to 31 s.

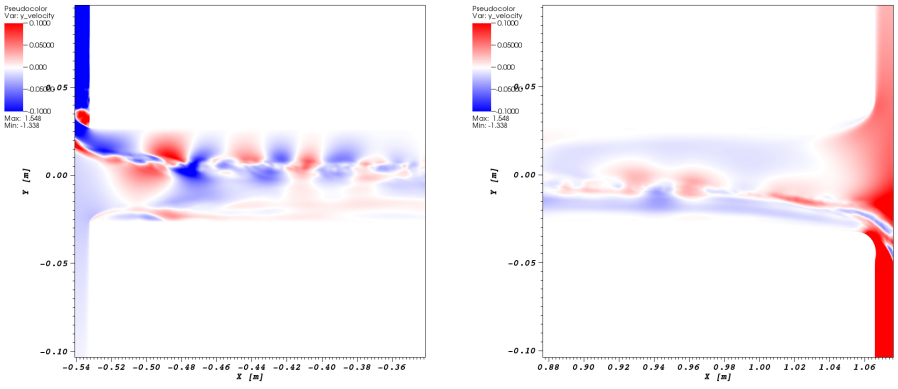

(c) 31 to 41 s.

Figure 3.31: POD mode 2 y-velocity at both (left) straight nozzle connected to tank and (right) smooth nozzle connected to annulus between various time windows.

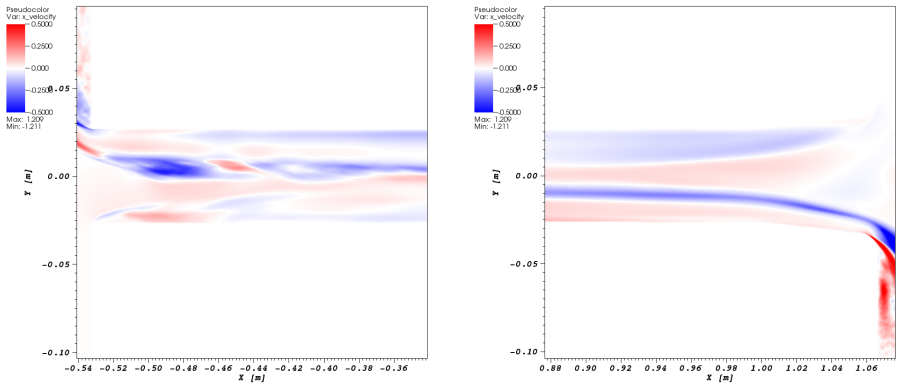

(a) 11 to 21 s.

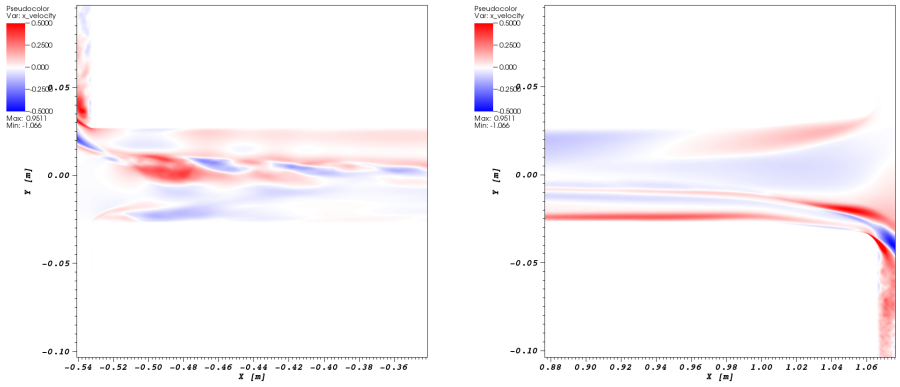

(b) 21 to 31 s.

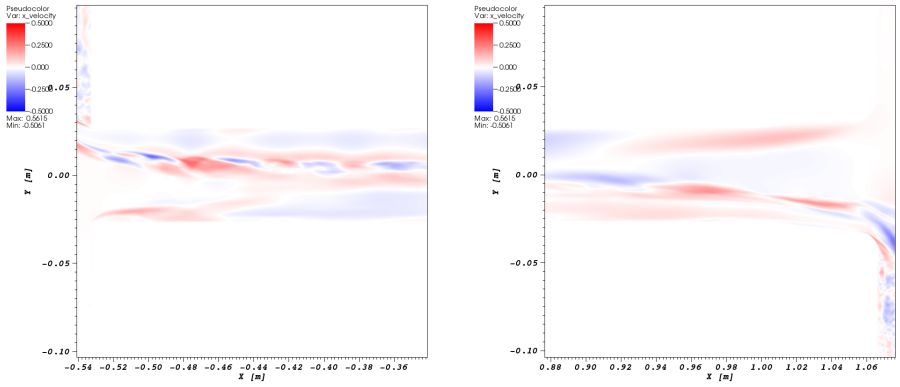

(c) 31 to 41 s.

Figure 3.32: POD mode 3 x-velocity at both (left) straight nozzle connected to tank and (right) smooth nozzle connected to annulus between various time windows.

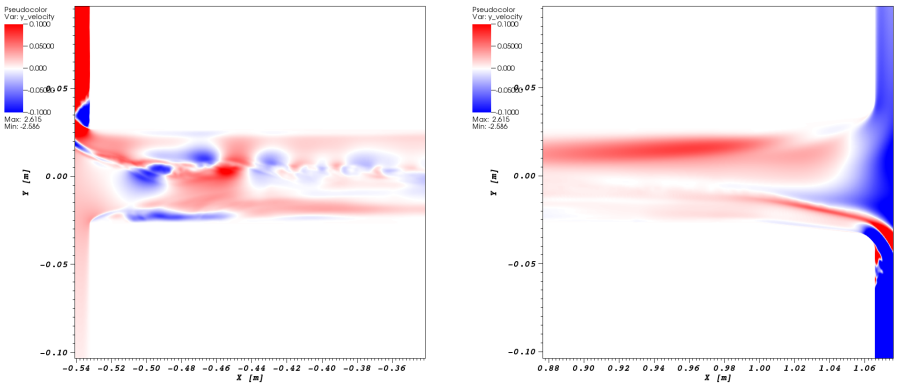

(a) 11 to 21 s.

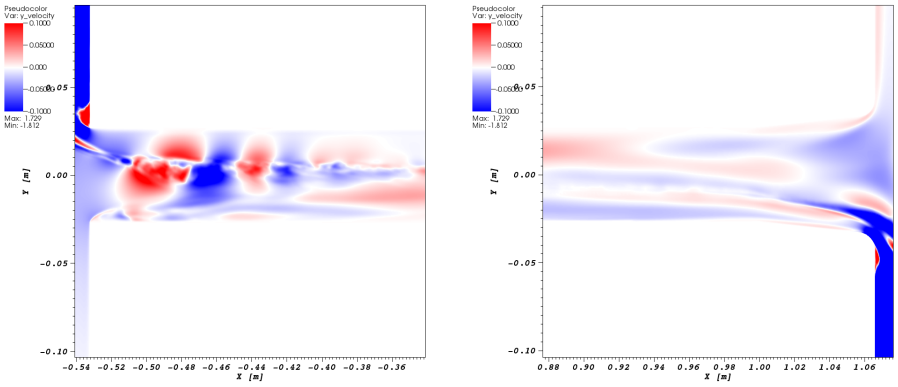

(b) 21 to 31 s.

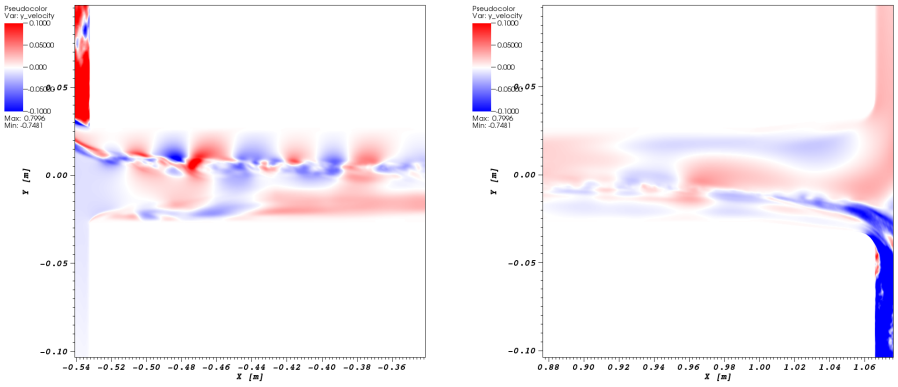

(c) 31 to 41 s.

Figure 3.33: POD mode 3 y-velocity at both (left) straight nozzle connected to tank and (right) smooth nozzle connected to annulus between various time windows.

3.8 Conclusions

Sensitivity analyses for this buoyancy driven, closed system at A = 0.05 show how different ICs, fluid models, and Sc change the system behavior. For ICs, instantaneous velocities are highly sensitive to any changes, but time averaging reveals that nearly no changes appear within the cold leg. On the other hand, the more turbulent downcomer is much more sensitive to any perturbations, since the flow involves entry to the nozzle, impingement on the inner wall, and spreading effects of going around the annulus. When validating against PIV measurements, the magnitude of Sc is observed to have a high influence on the velocity profile, especially at later times when predicting energy decay becomes important. Comparisons between LM and BA show insignficant differences that imply this Atwood number does approach the Boussinesq limit. There are several key discoveries from this study for this type of heat exchanger system:

1. The speed of the fluid front is insensitive to the chosen ICs and modeling parameters. The buoyancy term proves to have a larger effect on the evolution of the fluid front compared to the advection and viscous terms. This means that future validation studies need to analyze results after the fluid front passes before making any firm conclusions about modeling parameters.

2. Capturing the instabilities and fluctuations from using high Sc has proven to be essential for predicting the mean velocity. Therefore, it is recommended for future engineers to use the highest Sc available in literature when simulating this transience. Though resolving the small Batchelor length scale is impossible, added diffusion (either numerical or via another technique) will be present regardless to lower the effective Schmidt number.

3. Mixing immediately after the nozzle has shown to have an influence on mean quantities. Depending on how the flow enters the annulus, the mean can show a large bias towards one wall or another. Moreover, added turbulence can make the velocity profile more flat. This has been shown through adding small perturbations to the nozzle and even a 5% TKE has shown to increase the spreading in spanwise direction and decrease the streamwise veloc-

ities. Future studies should investigate the inclusion of smaller perturbations in the entire domain at earlier times to improve results for LES.

4. Studies on the Atwood number has shown that the fluid front is a good characteristic velocity for this transient geometry. Cold leg results for A = 0.05 and A = 0.10 match well when scaling the temporal windows using the fluid front ratios, while downcomer results have many similarities. Overall, correlations can be developed using simple regression analysis to predict Atwood numbers of greater or lower magnitudes.

Additional analyses such as the integral time scale show that statistics become relatively smooth even though full convergence cannot be obtained. Uncertainty methods show that errors are largest at the transition region between heavy and light fluids, and that there is difficulty in calculating errors for this transience in the large domain. Lastly, POD has shown that the overall decay of modes in the straight and smooth nozzles are fundamentally different. Alternating vortices are prevalent throughout the straight nozzle, but within the smooth nozzle they are nonexistant at early times windows. Overall, there have been many challenges for modeling a completely transient buoyancy driven flow. For this study, it has been shown that a closed system with valve opening can introduce undesired features that is difficult to capture with high fidelity simulations. Simulation parameters and resolution requirements have been documented to help future investigators of PTS or similar fluid scenarios to model this case.

4.1 Literature Review

The last mechanism of heat exchangers under consideration is the effect of thermal conductivity on heat transfer with turbulence. The Prandtl number (Pr) is the dimensionless number that quantifies this and is defined as $\frac{\nu}{\alpha}$, the ratio between diffusion of momentum over diffusion of thermal energy. For practical purposes, not all scales of motion in the thermal field are resolved to reduce computational costs and hence, a new parameter must be introduced, known as the turbulent Prandtl number (Pr_t). It is defined as $\frac{\nu_t}{\alpha_t}$ where the eddy viscosity is known and the turbulent thermal diffusivity is unknown. Pr_t can be assumed to be near unity due to the Reynolds analogy and has proved to be very accurate for most scenarios involving heat transfer [62]. This is because most experiments use more common fluids such as air or water for their measurements. However, fluids with very high thermal conductivity such as liquid metals show that the Reynolds analogy fails, because the relationship between momentum and heat transfer becomes less correlated [71].

Low Pr flows often involve liquid metal as their fluid due to high thermal conductivity. A review of multiple sets of liquid metal experiments for rod bundles by Mikityuk (2009) has shown current Nusselt number (Nu) versus Peclet number (Pe) correlations are poor and a new correlation is developed [72]. A heated rod validation experiment has shown that RANS has good comparisons with velocity measurements, but heat transfer comparisons show errors up to 7% when using Pr_t = 0.9. It is concluded that discrepancies arise from a poor prediction of the thermal boundary layer [73]. In the 2000s, a collaborative project called ASCHLIM worked towards Pr_t investigations by establishing a set of benchmarks for CFD. It has also been established that current models cannot predict the thermal boundary layer and suggests that new wall-functions should be developed based on measurements [74]. To recmedy this issue, Kays and Crawford (2012) investigated developing a new formulation for Pr_t by taking empiricial data using the turbulent Peclet number and fit it to a curve [75]. More recently, Shams et al. (2014) developed an algebraic turbulent heat flux model

that accounts for low Pr flows by using DNS data from channel flow. DNS that incorporated natural, mixed, and forced convection allowed for the improvement to their model correlations and coefficients [76]. The advantage of using DNS is that it eliminates the need for eddy diffusivity, including Pr_t , by having all momentum and thermal scales of motion captured.

DNS for liquid metals is available for basic geometries such as channel flow and backward-facing step. Kasagi and Ohtsubo (1993) has made simulations for Pr = 0.025 and compared their results with previous DNS of Pr = 0.71. Thermal turbulent statistics are taken to show major differences in heat transfer between Prandtl numbers [77]. Higher Re_τ simulations with DNS have also been conducted for channel flow by Abe et al. (2004) as well [78]. Niemann and Frohlich (2016) investigated the effect of low Pr on a backward-facing step geometry with and without buoyancy. Again, characteristics have different shapes due to differences in molecular heat transfer properties [79]. Low Pr DNS in literature only extends to these simple cases because of its high computational costs. However, modern high performance computing is allowing DNS of a more complex geometry to be more feasible.

The case under consideration is a tight lattice square rod bundle for advanced nuclear reactor core applications. This geometry is rich in physics while being simple enough for setting up a properly resolved DNS mesh. Moreover, a wide range of Reynolds numbers allows for the selection of the lowest Re_h to reduce computational costs for DNS. Data for bare rod bundle flows are prevalent, as discussed by Meyer (2010) in his literature review. Many works discovered difficulty of RANS to predict statistics due to anisotropy and presence of coherent structures, because the tight gap introduces flow oscillations and momentum transfer [80]. DNS of rod bundles have been conducted by Baglietto et al. (2006) [81], but to the author's knowledge none has been done to investigate the effects of heat transfer for low Pr in this geometry using DNS.

4.2 Channel Flow

4.2.1 Computational Domain

Before conducting DNS of liquid metals in rod bundles, it is advantageous to analyze low Pr DNS in existing cases such as Kasagi and Iida (1999) [82]. In addition to their previous work, simulations for Re_τ = 150 and 640 with Pr = 0.025 and 0.71 are considered with and without buoyancy for channel flow. This section will summarize the author's contribution to the collaborative work between Texas A&M University, University of Oklahoma, Mississippi State University, and our partners in national lab and industry as done in [83]. The high fidelity method that will be presented is PANS, which has been previously discussed in Section 1.2.4. The geometry under consideration is a rectangular prism where periodic boundary conditions are used for the x- and z-directions, while faces in the y-direction are no-slip and constant wall temperature for the walls. By using a heat sink in the energy equation, a constant heat flux scenario is replicated [77]. The turbulent coefficient Pr_t is specified to be 0.85 for the RANS and PANS simulations.

Using an 8^3 element channel with uniformly distributed streamwise elements and a wall refined distribution in the wall-normal direction, a total of 64^3 GLL points is used for N = 7 for Re_τ of 150. The domain size is selected to be the same as Kasagi and Iida (1999) as $5\pi\delta \times 2\delta \times 2\pi\delta$, where δ is channel half height [82]. For Re_τ of 640, a slightly larger mesh with 96^3 GLL points is selected for baseline comparisons. The time step needed for stability for Re_τ = 150 and Re_τ = 640 is 1.0×10^{-4} and 2.5×10^{-5}s respectively. Although the mesh should be more refined for PANS, especially when investigating small filter widths, it is kept the same as a baseline to have comparable computational costs with methods by other collaborators. By keeping the resolution the same for both URANS and PANS, this will allow for proper turbulent modeling comparisons.

It has been derived – using the Kolmogorov length scale as a reference by Girimaji and Abdol-Hamid (2005) [10] – that the minimum grid size can be calculated as a function of the filter width in the following equation

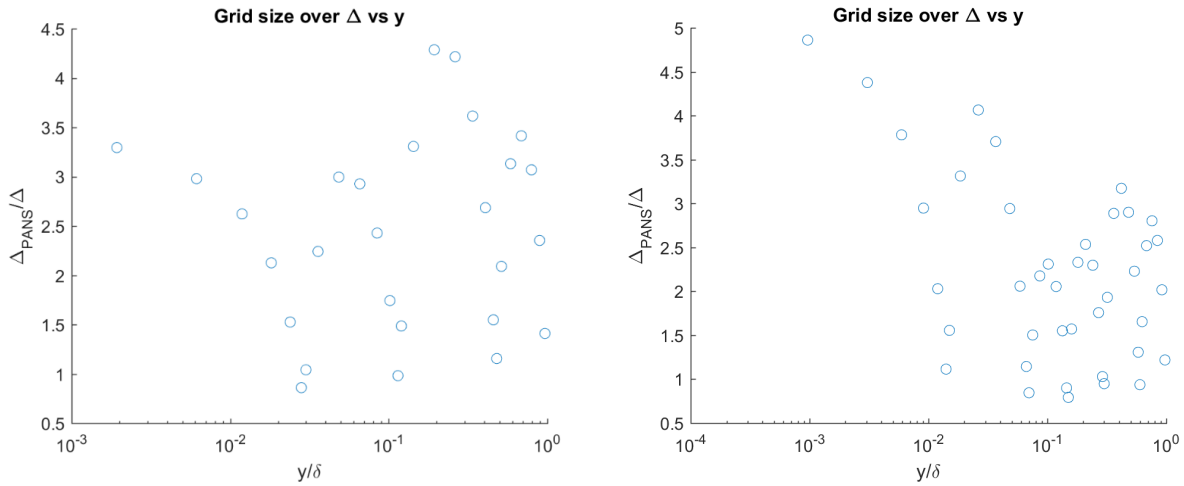

(a) Re_τ = 150. (b) Re_τ = 640.

Figure 4.1: PANS grid size over estimated minimum grid size for f_k = 0.10 at Re_τ = 150 and 640.

$$\Delta = C_\mu^{1.5} \frac{f_k^{1.5}}{f_\varepsilon} \frac{k^{1.5}}{\varepsilon} \tag{4.1}$$

where these quantities are solved from a RANS simulation. Using the distance between GLL points to calculate the relative grid size Δ_{PANS}, the ratio between grid size over the theoretical minimum can be made. Fig. 4.1 shows that the mesh is under-resolved for PANS for f_k = 0.10 since the ratio remains over 1 for most locations. This is expected, since the grid was chosen for URANS and the usage of f_k = 0.10 indicates that it requires higher resolution. Still, comparisons can still be made keeping in mind the low resolution. The present work investigates the sensitivity of f_k in increments of 0.10.

4.2.2 Filter Width Sensitivity

Sensitivity of f_k is conducted to determine which filter width is appropriate for channel flow. A previous study using PANS recommends that when there is clear separation between primary energy and its dissipation, f_ε = 1 while $f_k < 1$. For an external flow case, an f_k of 0.50 is used for a relatively large Reynolds number to get good results [10]. However, channel flow is very stable and the Reynolds numbers, at which DNS was conducted, is low. Hence, filter widths are varied

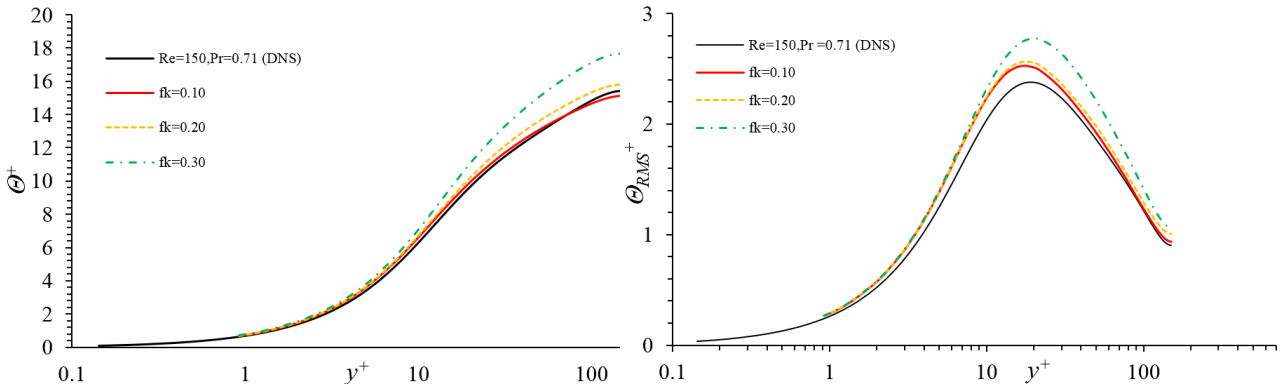

(a) Mean temperature

(b) RMS temperature

Figure 4.2: Mean and RMS temperature values for channel for Re_τ = 150 and Pr = 0.71.

from 0.1 to 1.0 in increments of 0.1 for this study. It is observed that the flow laminarizes for f_k equal to or greater than 0.4, even with large perturbations of up to 20% of turbulent kinetic energy. Therefore, only f_k values from 0.1 to 0.3 can properly simulate resolved components of turbulent kinetic energy and dissipation.

To calculate the actual kinetic energy and dissipation, the sum of the unresolved and resolved components must be considered to get the total value for PANS. The following are the equations used to get the correct quantities in channel flow for comparisons where the subscripts r, u, and tot are the resolved, unresolved, and total quantities respectively.

$$\overline{u'u'_{tot}} = \frac{2}{3}k_u + \overline{u'u'_r} \tag{4.2}$$

$$\overline{u'v'_{tot}} = 2C_\mu \frac{k_u^2}{\varepsilon_u}\left(\frac{\partial \overline{U}}{\partial y} + \frac{\partial \overline{V}}{\partial x}\right) + \overline{u'v'_r} \tag{4.3}$$

$$k_{tot} = k_u + \frac{1}{2}\left(\overline{u'u'_r} + \overline{v'v'_r} + \overline{w'w'_r}\right) \tag{4.4}$$

Since velocity and temperature profiles have identical trends when Pr = 0.71, only temperatures will be discussed for brevity to make conclusions regarding PANS. Here, constant heat flux BCs

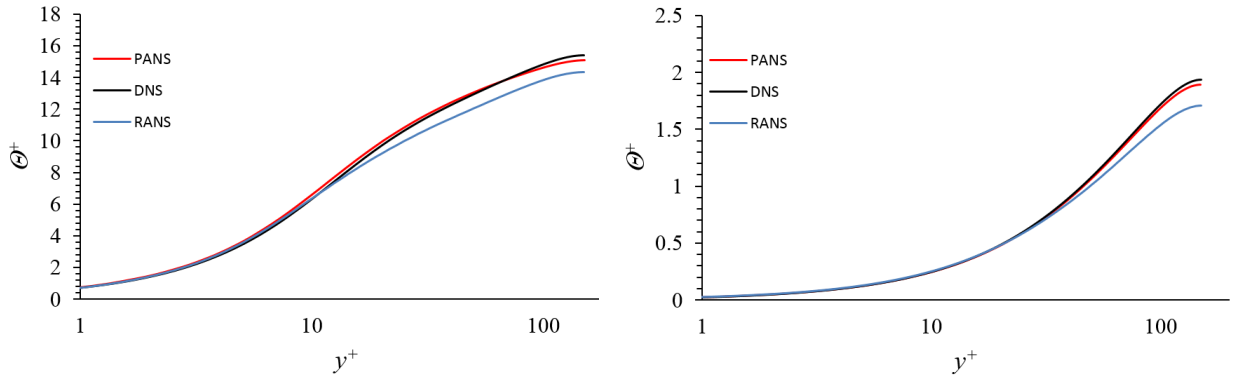

(a) Re_τ = 150, Pr = 0.71. (b) Re_τ = 150, Pr = 0.025.

Figure 4.3: Mean temperature for different Prandtl numbers with constant heat flux on both walls.

are replicated at the walls and temperatures are normalized by the wall temperature T_w in the same manner as Kasagi and Iida (1999) [82]. In Fig. 4.2, the trend for decreasing f_k becomes obvious. Larger f_k values consist of larger mean flow due to excessive modeling of the turbulent kinetic energy. For both the mean and fluctuating components, the temperature profiles are overpredicted when $f_k = 0.3$ and approaches DNS results as it goes to $f_k = 0.1$. Even better results can be obtained by increasing the mesh resolution and decreasing f_k slightly more, but to make fair comparisons between RANS and PANS, results for the smaller mesh are presented.

4.2.3 Temperature Profiles

RANS simulations have been conducted by W. D. Jock and Dr. D. K. Walters from University of Oklahoma [83]. Although the URANS equations are actually implemented, the stable nature of channel flow makes it impossible to capture transience at this Re and can be simply called steady RANS. The trends between velocity and temperature are identical when comparing RANS, PANS, and DNS results, hence again only temperature can be discussed for all intents and purposes. Also, simulations at Re_τ = 640 show very similar trends as Re_τ = 150, so only the lowest Re_τ is shown since the higher Re_τ does not presently have buoyancy DNS comparisons. Here, the PANS label indicates that an f_k of 0.1 is being shown, since it yields the best results. Fig. 4.3 shows that the lack of fluctuations in RANS causes the mean velocity to be underpredicted with RANS. Profiles

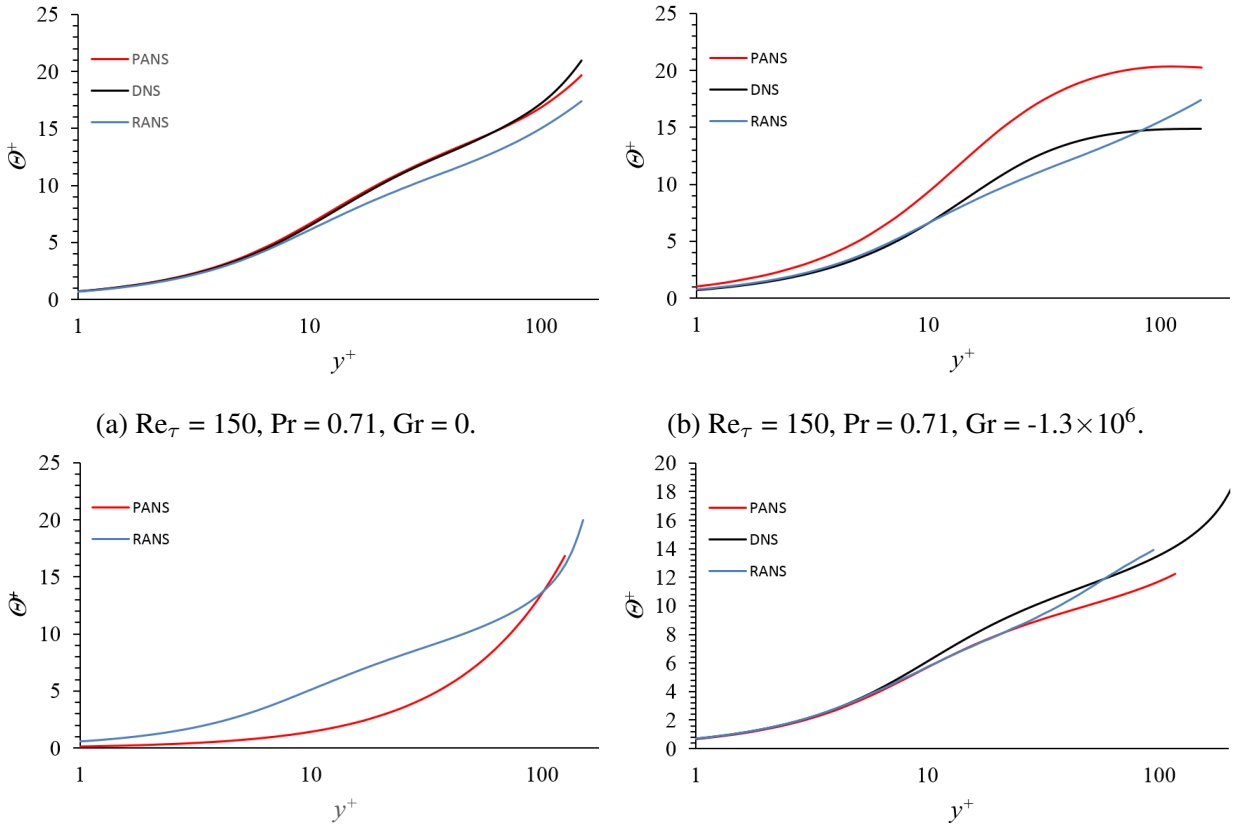

(a) Re_τ = 150, Pr = 0.71, Gr = 0.

(b) Re_τ = 150, Pr = 0.71, Gr = -1.3×10^6.

(c) Re_τ = 150, Pr = 0.71, Gr = 4.4×10^6.

(d) Re_τ = 150, Pr = 0.71, Gr = 9.6×10^5.

Figure 4.4: Mean temperature for buoyancy cases with different T_w .

for PANS is better, at the cost of additional computational resources due to its transient nature and longer convergence. When analyzing the difference between Prandtl numbers, temperature comparisons actually show no significant relative differences in how RANS or PANS predicts heat transfer. This indicates that the Reynolds number and geometry under consideration can use a constant Pr_t of near unity and do well in predicting heat transfer effects. It is also important to add that at Re_τ = 640, identical trends are observed.

DNS results also incorporate cases with buoyancy where the wall temperatures T_w of the top and bottom are different. When buoyancy is not included for these new BCs, it is evident that the trend is the same as the case with constant heat flux as shown in Fig. 4.4a. After adding buoyancy effects, there becomes a larger discrepancy between RANS and PANS, most likely due to PANS

capturing the transient effects. For Gr = -1.3$\times 10^6$, PANS largely overpredicts the temperature profile while RANS has a more similar magnitude. However, the shape of RANS with the additional buoyancy term appears to share the same shape as the case with Gr = 0 (which indicates the buoyancy term in the equation has little influence on the flow for stable Grashof numbers). PANS predicts the shape better, although has difficulty with magnitude likely because the mesh is too coarse for the small f_k . The difference in shape can be observed in both Gr = 4.4$\times 10^6$ and 9.6$\times 10^5$. Overall, it appears that the introduction of buoyancy makes it difficult for both RANS and PANS to predict the average temperature profiles.

Additional results regarding the channel flow aspect of this project can be found in Bhushan et al. (2018) [83], where comparisons with other simulations are presented as well. Since modeling efforts at Re_τ = 150 and Re_τ = 640 still show reasonable heat transfer predictions at low Pr, it is determined that a more complex flow is required before the Reynolds analogy breaks down and the usage of Pr_t around unity becomes an issue.

4.3 Rod Bundle Validation

4.3.1 Computational Domain

For an applied DNS test case, the tight square lattice rod bundle experiment conducted by Hooper and Wood (1984) is considered due to its simple geometry yet complex physics as previously mentioned [3]. The facility consists of six 14 cm diameter rods spaced with P/D = 1.107 and a hydraulic diameter of 7.84 cm. The low P/D ratio and large range of Re_h makes it a good candidate for a DNS benchmark. The experiment has an axial length of 128 hydraulic diameters, which is sufficiently long enough to be considered fully developed. Spacers are placed to hold the rods and create two subchannel regions as shown in Fig. 4.5. The labeled "unit cell" represents the smallest symmetric geometry that represents a square lattice bundle. It is possible to simulate this flow using only one unit cell for RANS, but since there are oscillatory effects and more complex fluid motion, 16 unit cells will be required for DNS. Additionally, it is important to capture no-slip BCs from the spacers to get accurate representation of the physics. Measurements documented in

Hooper and Wood's database are radial from the rods θ = -10° to 55° with increments of 10° [84]. This means that the line at θ = 0° is from rod wall at x = 0 to the gap center (origin), a located between the two center rods. The line at θ = 45° goes towards the subchannel center, a location furthest from rod walls.

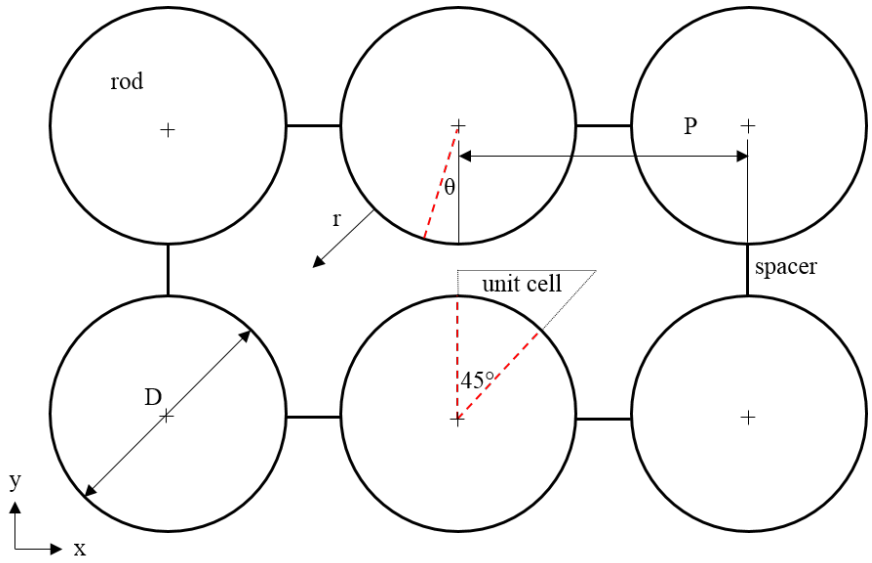

Figure 4.5: Geometry of rod bundle where θ is measured from gap center (origin) and lines are measured normal to rod surface.

The mesh is designed for spectral element method with Nek5000 where aspect ratios far from the wall are as close to unity as possible, as shown in Fig. 4.6. Hence, elements in the z-direction have the same side length as the center diamonds to maintain good aspect ratios. Through preliminary sensitivity tests, it has been confirmed that mean statistics with an axial length of 24.0 rod diameters become invariant with the domain length. For each unit cell, there are 6 elements in the θ-direction, 6 elements in the r-direction, and 480 elements in the z-direction, which totals to 829,440 hexahedral elements. Element growth away from the wall is 2.0 for the first 4 elements, meaning that GLL point spacing becomes smaller as N increases. Near-wall elements are spaced such that the first near-wall GLL point has an average of y^+ of 0.15 for N = 7 and at least 3 GLL points within $y^+ < 1$.

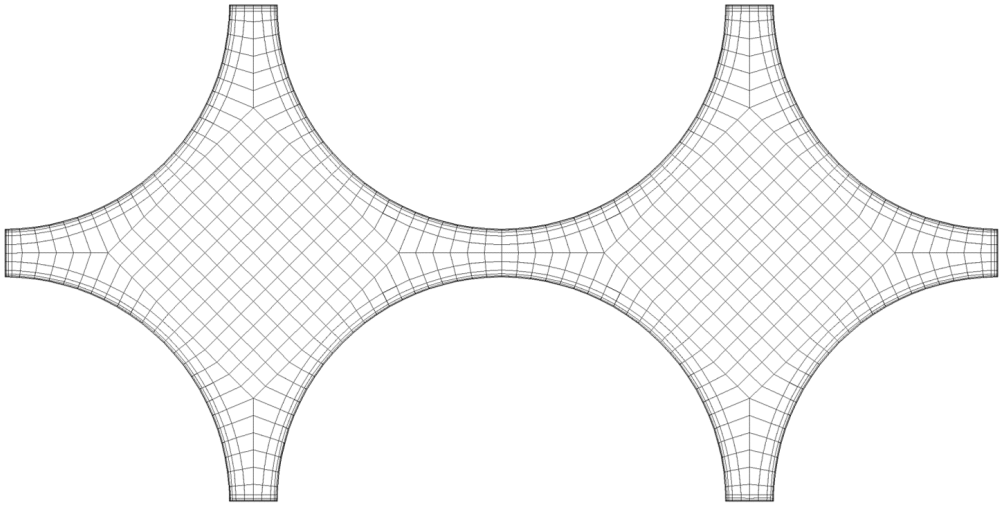

Figure 4.6: Element distribution for each spectral element on the xy-plane before discretization in GLL points.

Simulations are set up such that all values are normalized by rod diameter (D), bulk velocity (V_b), and Reynolds number (Re_h). This means D = 1.0, V_b = 1.0, D_h = 0.56023, ρ = 1.0, and ν = 2.478867×10^{-5} to yield Re_h = 22600. The energy equation is also normalized, so that heat capacity c_p = 1.0 and thermal diffusivity $\alpha = \nu/Pr$. Since the values of temperature become arbritary, the average temperature is maintained at 100.0, by using a flux ϕ = 0.1 at rod walls and heat sink of $\phi/L \times$(rod surface area) = 0.6282. For the spacers, Neumann BCs are specified with a zero flux so only rod walls will have an influence on the heating of the fluid.

4.3.2 Analyses

As mentioned in Section 1.2.1, the Kolmogorov length, time, and velocity scales can be calculated using the dissipation of turbulent kinetic energy. Therefore, one method to check if length scales are properly being resolved is to calculate the ratio of relative mesh size (Δx) divided by the Kolmogorov length scale (η). As long as these ratios are smaller than 1, there can be confidence that the simulation is properly resolving the turbulence. Using the spacing between GLL points to calculate Δx, the ratios for each polynomial order can be calculated as shown in Table 4.1. As one would expect, as the polynomial order increases, the mesh size ratio decays at an exponential fashion. The difference between N = 5 and 7 is more significant than between N = 7 and 9. The

time step is much smaller than the Kolmogorov time scale for all cases and will not introduce any temporal errors.

Polynomial order N	max(Δx / η)	Δt / max(τ_η)
5	0.30	0.19
7	0.17	0.08
9	0.10	0.02

Table 4.1: Ratios of local mesh and time step to Kolmogorov length and time scales.

Kármán vortices appear within the gap center due to the tight gap between the rods, which has been shown in literature of similar cases [80]. Hence, a similar analysis is conducted for DNS where instantaneous velocity is recorded at various points across the domain as shown in Fig. 4.7. A location at the gap center (where the origin is) and at the subchannel center (a location furthest from rod walls) is selected to be a good candidate for analysis. For the gap center, there is an oscillatory effect where viscosity becomes dominant due to no-slip BCs. At the subchannel center, it is much more difficult to differentiate how the signal is behaving. Therefore, analysis using FFT can be used to quantify the oscillatory behavior.

Using Welch's method to estimate the power spectral density (PSD) [85], the frequency spectrums for both locations are shown in Fig. 4.8. At gap center, it is evident that there is a dominant frequency that holds a majority of the energy, whereas higher frequencies have little influence. This spectral peak lies at roughly 40 Hz. Calculation of the Strouhal number using the characteristic dimensions ($St = f D_h/V_b$) can be equated to 22, revealing that oscillations are extremely large. PSD of the subchannel center more resembles turbulence, where energy cascades to higher frequencies at a steady rate. Still, it is possible to see the large 40 Hz frequency within this PSD, hinting that this mode of energy can propogate to other locations as well.

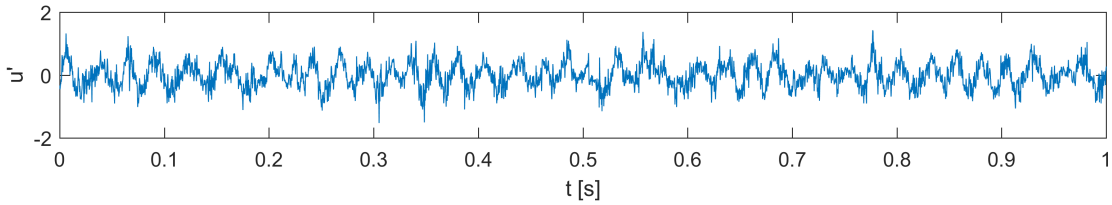

(a) Gap center

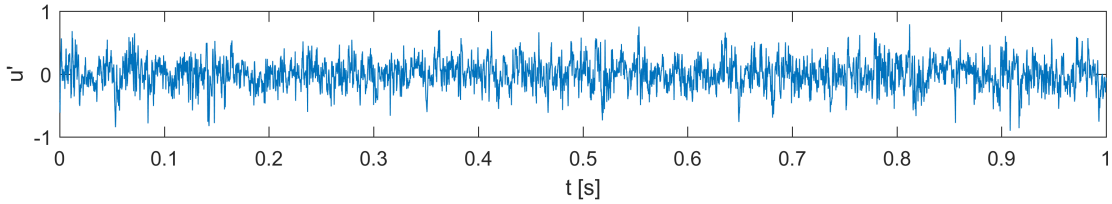

(b) Subchannel center

Figure 4.7: Instantaneous velocity fluctuations of x-velocity in m/s at (a) gap center and (b) subchannel center.

4.3.3 Wall Shear Stress

The first step in validating the simulations is to compare the wall shear stress distribution across the θ-direction of the rod. To properly compare data, the distribution must be normalized by the mean wall shear stress $\tau_{w,m}$ between $0^\circ \leq \theta \leq 45^\circ$. Results for N = 9 every 5 $^\circ$ are extracted radially across the rods to estimate the wall velocity gradients. In Fig. 4.9, comparisons show that the wall distribution closely resembles those of Hooper and Wood (1984) [3]. There are minor differences due to both numerical and experimental imperfections. Distributions for DNS are not as smooth due to the lower resolution in the θ-direction and due to statistics not being completely converged. For the experiment, there is a lack of symmetry due to possible uncertainties in measuring techniques. Nonetheless, it is confirmed that the wall distribution is validated and that DNS shear stress closely resembles reality.

4.3.4 Velocity

The instantaneous velocity contour can be shown in Fig. 4.10. Flow oscillations mentioned previously can be observed by the complex scales of motion captured by DNS. Other studies of rod bundles with RANS shows a steady oscillation at the gap center [86, 87], while DNS reveals

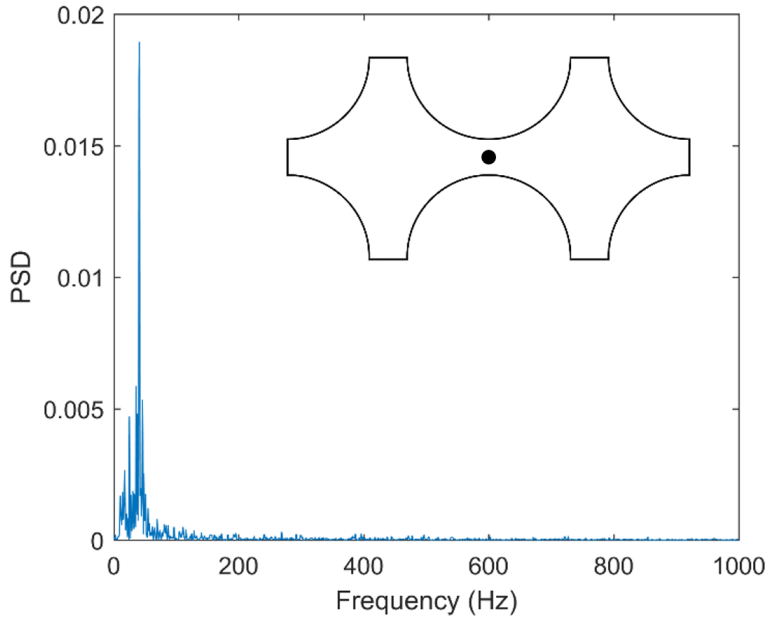

(a)

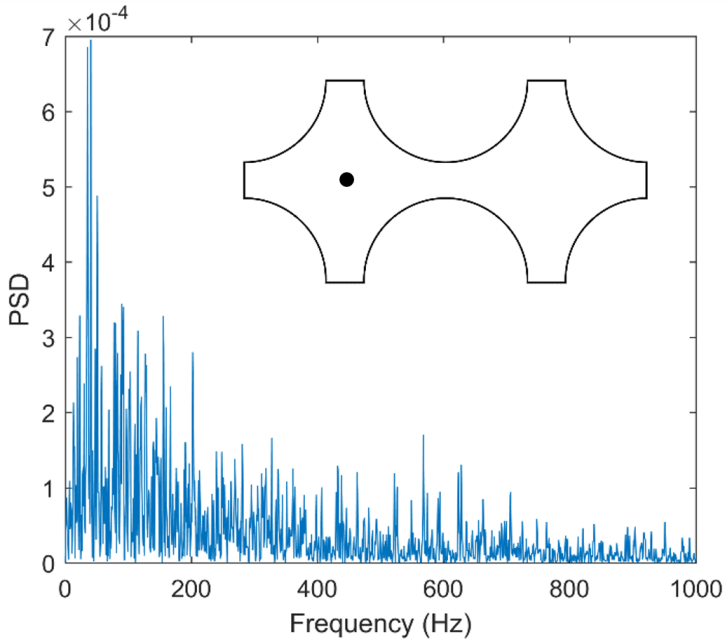

(b)

Figure 4.8: Power spectral density of x-velocity at (a) gap center and (b) subchannel center.

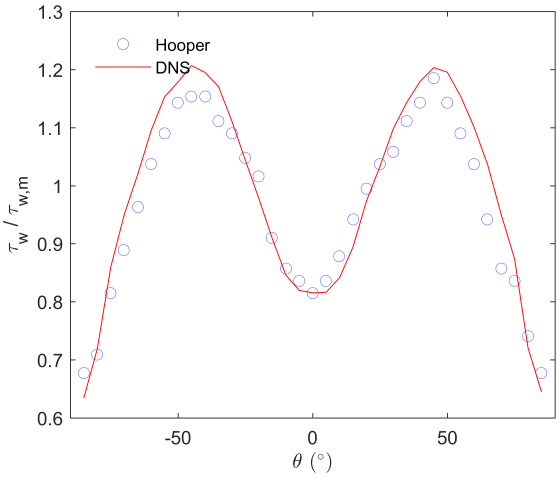

Figure 4.9: Wall shear stress across the surface of the rods.

other turbulent effects in this region. As fluid oscillates side-to-side around the gap center, mass is exchanged from one subchannel to another. Moreover, as TKE in one subchannel increases, energy in the other decreases. For an infinite array of rods, these oscillations would be generated at every gap, but the effect of wall spacers suppress the oscillations at other locations for this geometry.

Since simulations have been normalized, velocities are scaled multiplying velocity by experimental bulk velocity. The bulk velocity can be calculated using $V_b = \nu Re_h / D_h$ to convert it to m/s. The "original" label in Fig. 4.12 shows that velocities are consistently overpredicted even though the model is identical to the experiment. It is possible that there are laminarizing effects within DNS, so a test is done where the Reynolds number is increased and then decreased. However, this sensitivity test did not change results. Moreover, the length of the domain was increased as previously mentioned to find no difference in magnitudes either. It is not out of the question that the fluid properties of the experiment could be inaccurate up to 10%, so the viscosities of various Reynolds numbers are presented in Fig. 4.11. It is shown that documented kinematic viscosities vary in a nonlinear fashion, and although fluid property discrepancies up to 10% appear innocuous, they change DNS velocity calculations significantly. Hence, values from literature are gathered [88] and justified using a linear fit calculation of Hooper and Wood's data to be ν = 1.54$\times 10^{-5}$ m^2/s. This hints that it is possible the experimental Re_h could be larger than reported. Therefore, the bulk

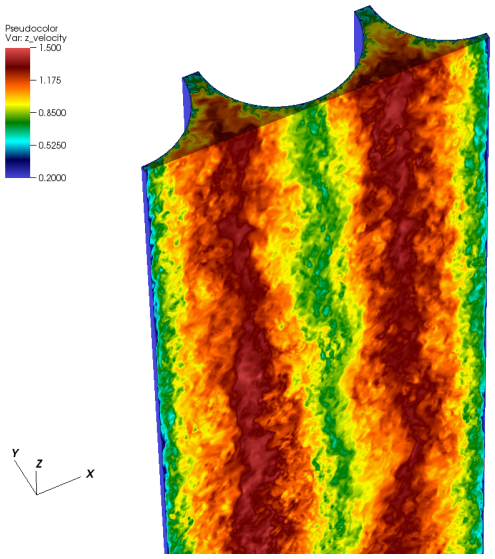

Figure 4.10: Instantaneous velocity contour in the streamwise direction at a slice y = 0.

velocity used for the "scaled" dataset is calculated to be 4.4393 m/s.

The new normalization factor in Fig. 4.12 reveals that the bulk velocity matches well with the experiment. Simulations at both N = 7 and N = 9 overlap and show that the simulation is not sensitive to the spatial discretization. However, simulations at N = 5 (not plotted) have discrepancies due to the lack of grid points within $y^+ < 1$ as well as the coarse regions at 22.5 ° , where the ratio Δx / η can become large. Therefore, it is determined that simulations must be at least N = 7 to be considered DNS. Closer inspection of Fig. 4.12 show that for both N = 7 and N = 9, near wall velocity validation is consistently smaller than the experiment. This difference is present at every angle, and discrepancies in wall velocity gradients will have a large impact when analyzing the wall normalized velocity U^+.

The average velocity profile at two different locations are presented in Fig. 4.13a-b. For these plots, $U^+ = W/u_\tau$ and $y^+ = u_\tau r/\nu$. Now, it is demonstrated that even with scaling that there are differences between DNS and the experimental case. Still, the original dataset matches with the log-law region at 45° where $\kappa = 0.41$ and B = 5.1, giving confidence to simulation results. With the presence of the tight gap at 0° , normalized velocities go above the log-law. The viscous sublayer is

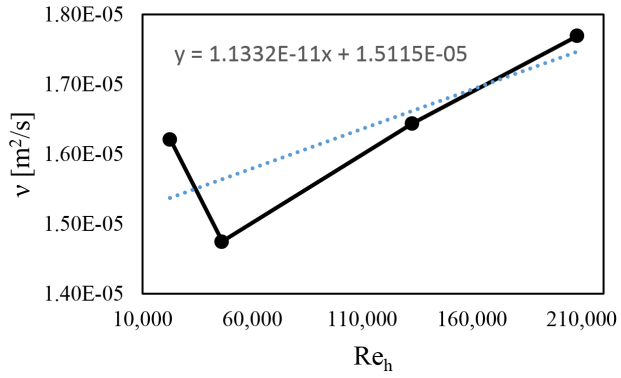

Figure 4.11: Kinematic viscosities from Hooper and Wood (1984) [3] with respect to the Reynolds number.

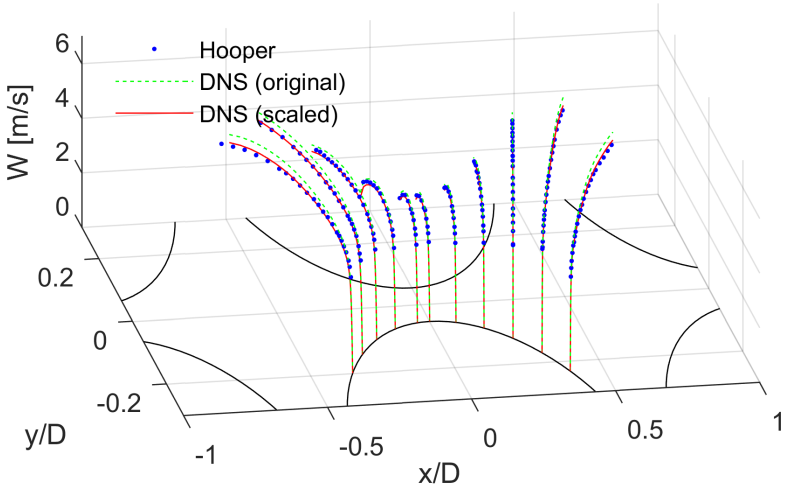

Figure 4.12: Streamwise velocity validation along various locations normal to rod surface.

captured at all locations under consideration, showing that the theoretical wall gradient is resolved. The difference between the original and scaled dataset within the viscous sublayer is impossible to observe, and thus proves the difficulty in knowing the exact normalization value. One possible explanation of the differences between DNS and experimental results is the location of the buffer layer. The log-law region appears to occur earlier in Hooper and Wood's database than predicted by DNS.

Since the friction velocity does not have the same value as DNS, there will also be differences in

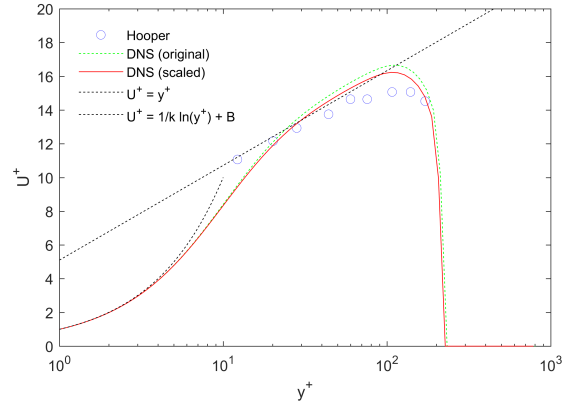

(a) Mean velocity at $\theta = 0°$

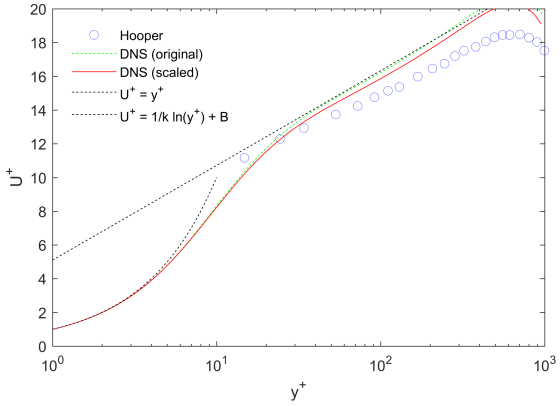

(b) Mean velocity at $\theta = 45°$

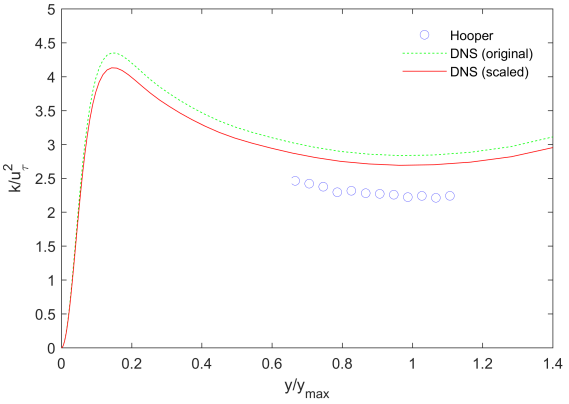

(c) TKE at $\theta = 0°$

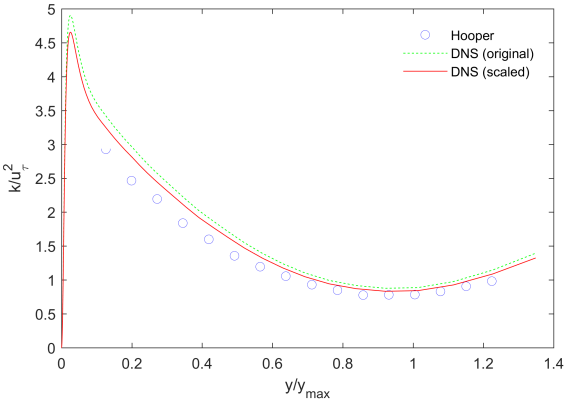

(d) TKE at $\theta = 45°$

Figure 4.13: Mean velocity profile and TKE at locations radial from rods.

TKE since presented data is normalized by u_τ^2. In Fig. 4.13c-d, the wall distance is now normalized by y_{max} (radial distance to y = 0) as done in Hooper and Wood (1984) [3]. For both θ = 0° and 45° , there is symmetry for DNS around y_{max} = 1 due to geometrical symmetry. The magnitudes at 0° have poor comparisons with experiments but share the same shape for the available data. On the other hand, TKE at θ = 45° appears more accurate. This effect is due to the much smaller friction velocity at the gap center compared to the angle furthest from other rod walls. Reinforced with the information that the documented experimental accuracy of Reynolds stresses is 10-15%, the fluctuating velocities for DNS has been validated. Moreover, the overprediction of TKE is simply due to the larger wall shear stress of the experiment compared to DNS calculations. Overall, the discrepancies are the consequences of possible different experimental conditions compared to the theoretical model, such as having a more turbulent field within the test facility. Measurements with Preston tubes has some inaccuracies in measuring the secondary flow, albiet small.

4.4 Rod Bundle Heat Transfer

4.4.1 Qualitative Temperature

It has been confirmed that DNS calculations closely resemble a real rod bundle and can be a good benchmark for studying heat transfer with different Prandtl numbers. Since experiments and simulations do not perfectly match each other, comparisons with this DNS benchmark should be standalone, rather than comparing with Hooper and Wood's database. The addition of temperature does not require higher resolution, because the Batchelor length scale for the energy equation can be defined as $\eta/Pr^{0.5}$. This means that as long as Prandtl numbers under investigation are less than 1, the length scales of temperature will never be larger than η. This means that previous ratio studies in Table 4.1 will be smaller for Batchelor length scales and remain valid.

The Prandtl numbers simulated are 0.71, 0.1, 0.02, 0.01, and 0.002 to demonstrate the effects when approaching the thermal conductivity of liquid metals. Instantaneous temperature profiles at the symmetric plane in Fig. 4.14 reveal the difference in complexity of length scales when the thermal conductivity changes for the system. When Pr is close to unity, the scales of motion tend to be

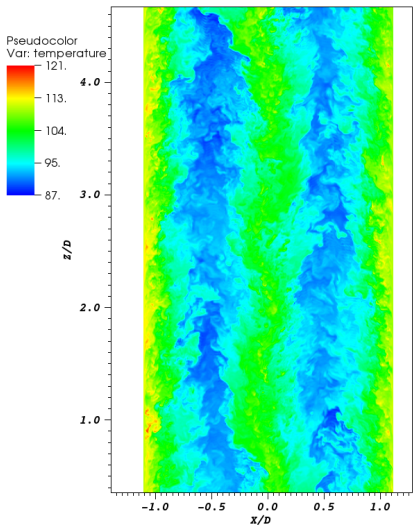

(a) Pr = 0.71

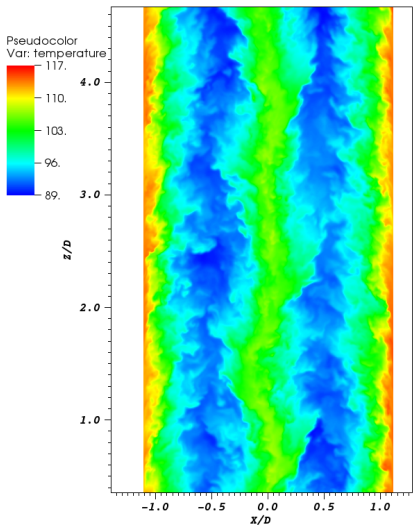

(b) Pr = 0.1

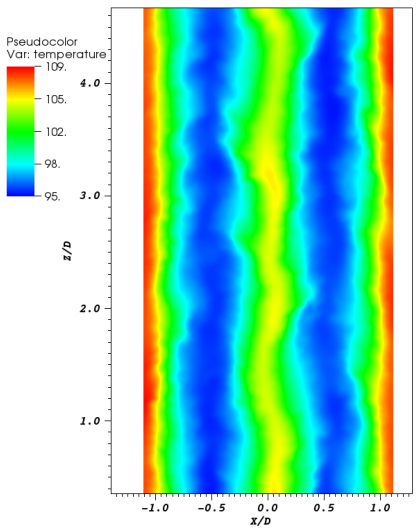

(c) Pr = 0.01

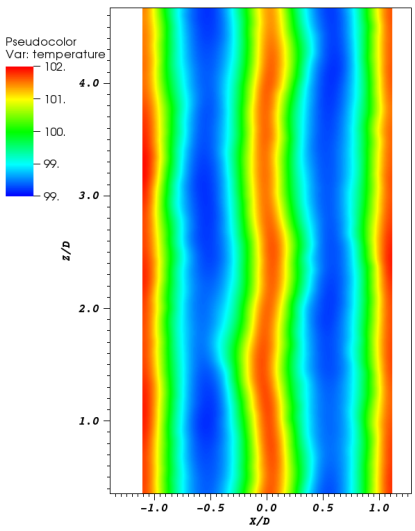

(d) Pr = 0.002

Figure 4.14: Instantaneous temperature contours at the symmetry plane y = 0 for various Prandtl numbers.

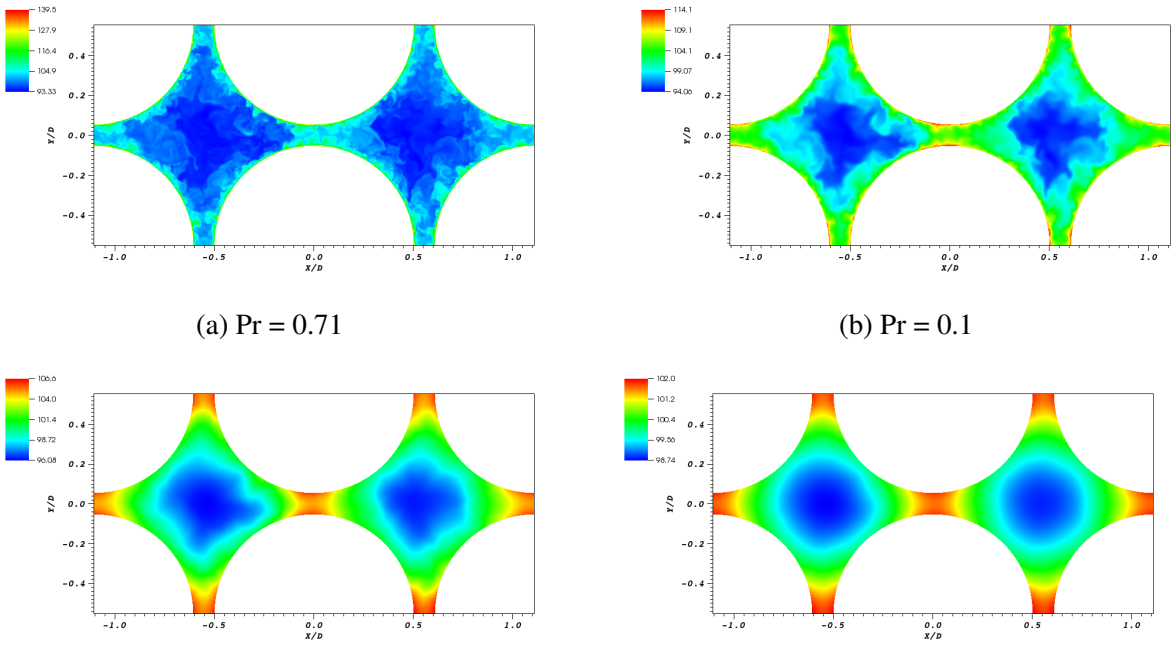

(a) Pr = 0.71

(b) Pr = 0.1

(c) Pr = 0.01

(d) Pr = 0.002

Figure 4.15: Instantaneous temperature contours at z = 0 for various Prandtl numbers.

very similar to those for momentum. Since the constant flux $\phi = 0.1$ does not change, higher conductivity means lower temperature differences within the system. The legend in Fig. 4.14 is scaled by its local maxima, so qualitative comparisons can be easily made. Even at the lowest Prandtl number, there are still oscillations within the gap center. This indicates there is enough momentum in the system to push thermal energy from subchannel to subchannel even for conductivities of liquid metal.

To visualize motion in the radial and azimuthal direction, Fig. 4.15 shows a slice at z = 0. For Pr = 0.71, the scales of temperature appear very similar to velocity, where near-wall scales are small and grow as they get further from the rod walls. At Pr = 0.1, there is already a significant difference in complexity of temperature movement and can be analogous to a more "viscous velocity distribution." Relative wall temperature gradients are smaller, and this trends continues as Pr decreases. At the lowest Prandlt number, almost no change is observed in the r- and θ-direction. This characteristic of behaving so different than velocity makes it difficult to use $Pr_t = 1$ for this

type of flow.

4.4.2 First and Second Order Statistics

Taking line profiles as conducted in Fig. 4.16 proves that the temperature gradients for the highest Prandtl number are largest, while little temperature change is observed for the lowest Pr. Although Pr = 0.71 and Pr = 0.1 vary by almost an order of magnitude, the bulk temperature at $y/y_{max} > 0.2$ remains relatively the same. However, when Pr is changed from 0.02 to 0.01, the bulk temperature is much different even though it has been changed by a magnitude of only 2. This characteristic highlights difficulty for accurately predict the bulk temperature at Prandtl numbers of these magnitudes using turbulence modeling techniques.

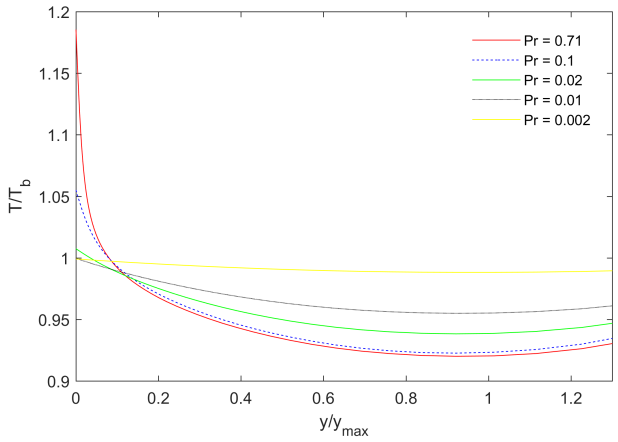

Figure 4.16: Average temperature profile at $\theta = 45°$ normalized by bulk temperature.

To relate this temperature profile for developing thermal wall functions, the distribution is normalized by the square root the characteristic temperature in Fig. 4.17. The characteristic temperature is equal to the heat flux times length divided by thermal conductivity. The distribution of temperature for Pr = 0.71 is identical to velocity, aside from its magnitude due to the definition of normalization. For Pr = 0.1, the logarithmic region begins earlier and has a steeper slope than for higher Pr. Both Pr = 0.01, 0.02, and 0.002 have the same shape with different magnitudes, alluding

that the same wall function could be used for Pr of magnitude 1×10^{-2} and 1×10^{-3}. This finding proves that it may be possible to develop a universal thermal wall function for liquid metals. However, additional investigation will be required at other locations and closer analysis should be done for future work.

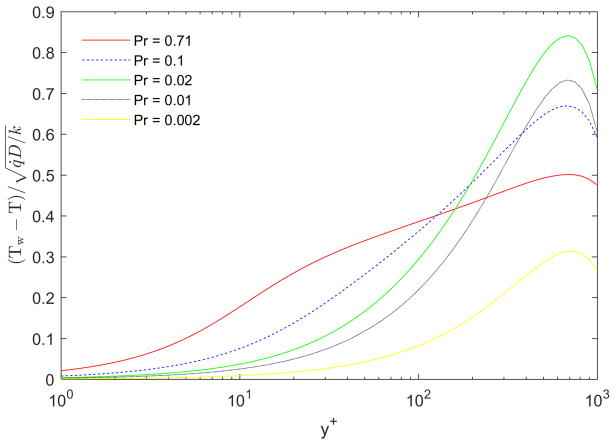

Figure 4.17: Average temperature profile at θ = 45° normalized by square root of characteristic temperature.

The temperature fluctuations in Fig. 4.18 reveal that the shape of Pr = 0.71 closely resembles TKE. On the other hand, every other Prandtl number under consideration has a different shape. When observing the peaks of the temperature fluctuations, they gradually increase as the Prandtl number decreases with the exception of Pr = 0.002. This is because when conductivity is extremely high, temperature fluctuations in the far-wall regions become negligible. Pr = 0.01 and Pr = 0.02 have identical peak locations for RMS of temperature, albiet different magnitudes. This trend is relatively the same at most locations except at the gap center.

At the gap center, it is easier to compare trends by normalizing the values by their local maxima as shown in Fig. 4.19. Here, the peak occurs at roughly y/y_{max} = 0.15 for the highest Prandtl number, while other Prandtl numbers have their peak occur at the point of symmetry at y/y_{max} = 1.0. Therefore, it is concluded that any Prandtl number of 0.1 or less for this Reynolds number has

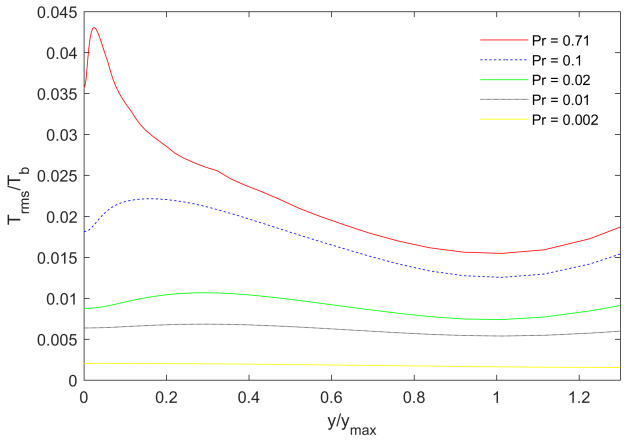

Figure 4.18: RMS of temperature at $\theta = 45°$ normalized by bulk temperature.

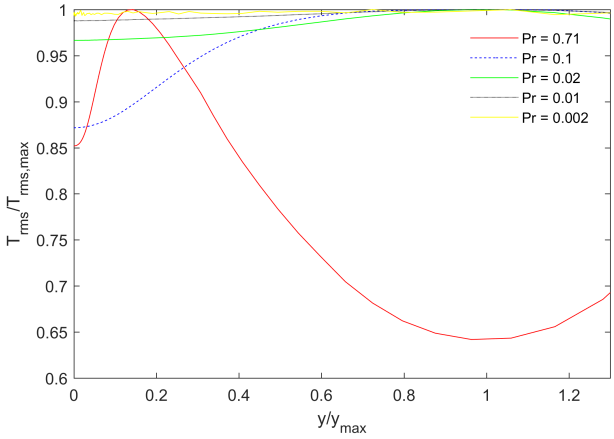

Figure 4.19: RMS of temperature at $\theta = 0°$ normalized by local maximum.

its largest source of temperature fluctuations at gap center, rather than near the rod surface.

4.5 Conclusions

The influence of fluid properties on heat transfer has been analyzed for a rod bundle heat exchanger application. First, available data on DNS of channel flow is analyzed to discover that RANS methodologies predicts heat transfer reasonably well compared to DNS. This indicates that a more complex geometry is necessary before using $Pr_t = 1$ becomes an issue. The higher fidelity method of PANS is used to discover that low f_k values are required to obtain transience and prevent

laminarization. Although its comparison with DNS is better than RANS, the computational cost of PANS show that the method is not necessary to improve low Prandtl modeling for channel flow.

Through literature review, a bare rod bundle geometry is chosen as the more applied and complex test case for liquid metal investigations. Validation of both average quantities and turbulent energy shows that the DNS benchmark is a suitable case for replicating realistic fully developed rod bundles. Analyses with the Kolmogorov length and time scales show that all scales are being resolved in the simulation. Moreover, the negligible differences between N = 7 and N = 9 for mean values reveal the simulation is independent of the grid. A constant heat flux is imposed for simulations of different Prandtl numbers, and calculations investigate the influences of changing the thermal conductivity. It is evident that Prandtl numbers near unity show similar characteristics for both average and RMS temperature, however very different features are observed for $Pr < 0.1$. For instance, near wall gradients are reduced as the Prandtl number decreases. Differences in bulk temperature are found even when moving from Pr = 0.02 to 0.01 due to the effects of the thermal conductivity on this flow.

Now that DNS data is developed for this bare rod bundle, engineers can develop their own thermal wall functions for the Prandtl number under consideration. Plots of normalized temperature distributions are presented, and once the database is released, values for all locations can be used as empirical data. It is evident that the near-wall tempreatures are heavily impacted by the molecular Prandtl number. Moreover, investigations of the turbulent Prandtl number can be made through algebraic calculations. Although focus lies within the energy equation, studies on improving RANS and LES models when there is a tight gap between rods can also be conducted. The statistics gathered from DNS can be used to calculate the production and dissipation of TKE at every location and be matched with current turbulent modeling techniques. Overall, this high fidelity database becomes a useful tool for fine tuning liquid metal modeling in this complex application.

Some passages, analyses, and figures in this section reference or are quoted from the author's previously published work in [83] and [89].

5. SUMMARY AND CONCLUSIONS

5.1 Summary of Cases

The advantages and disadvantages of high fidelity CFD for studying turbulence have been presented for applied heat exchanger scenarios. The required grid sizes to obtain spatially-independent calculations become excessively large and impractical for design efforts. However, a deeper understanding of the physics through their transient nature and ability to capture greater scales of motion allows higher order analyses that uncover more information than lower resolution techniques. The individual projects that isolate heat exchanger mechanisms investigate turbulence within a complex geometry, mixing within a buoyancy-driven system, and heat transfer within low Pr rod bundles.

5.1.1 HCSG

Turbulence within the HCSG is complex due to its three-dimensional physics. Its geometry resembles flow over a cylindrical rod, however its P/D ratio changes constantly along the axial direction. Rather than having the rods bank in the same direction, the rods curve with different angles and add to its complexity. Whereas vortex shedding commonly occurs for flow over a cylinder, the axial flow can distrupt the transverse movement. The LES model is confirmed by testing the sensitivity of the inlet BC and the polynomial order to see if quantities of interest change. Then, comparisons with established fluid dynamical features in literature are made such as the law of the wall, the subinertial range of the energy spectrum, and the Taylor length scales. These tests reveal that the spectral discretization at N = 7 and N = 9 for the given mesh are able to capture the expected turbulent characteristics.

LES calculations are validated with experimental results involving both first and second order statistics. Through instantaneous velocity observations from CFD, there are still characteristics of flow oscillations, although not as dominant as one who would observe in typical vortex shedding with FFT analysis. Recirculation zones grow and shrink with long temporal wavelengths, which was also observed from the experimental test section. This evolution indicates that the full geom-

etry will also have flow oscillations which can cause vibrations within the system. Additionally, POD analysis from both LES and PIV quantify some of the coherent structures that appear within the first modes around the center region furthest from the rods. The overall turbulent characteristics have been analyzed for the HCSG geometry, and the requirements for high fidelity LES for this case have been documented.

5.1.2 Buoyancy Driven Flow

The mixing within a system purely driven by buoyancy isolates an important aspect of heat exchangers: momentum generated via potential energy within fluid property differences. Although this particular case is isothermal, its turbulent mixing can be analogous to scenarios where fluids have different densities based on temperature changes. Using the Atwood number to characterize the magnitude of buoyancy and the Schmidt number to characterize mixing due to mass diffusion, an experimental benchmark is established to help validate CFD methods. The geometry consists of a cylindrical tank and annulus connected by a transfer pipe. Within the pipe, a disc valve separates two fluids with different densities and viscosities. The high fidelity technique of LES is utilized to predict the transience immediately after the disc valve opens when the two fluids begin to mix.

Verification is conducted in two ways: through sensitivity of the buoyancy model and mixing parameters, and through simulations of varying spatial discretization to quantify error bars. Due to the transient nature of the problem, analyses using the integral time scale are utilized to establish psuedo-steady time windows, where statistical validation can be made with the experimental benchmark. This is needed since the fluid undergoes multiple stages of wave formation, as well as instabilities within the transfer pipe that are difficult to quantify. Comparisons with experiments show that velocity statistics are reasonable within the pipe, and less accuracy is found within the downcomer. Further investigation – through sensitivity analyses in the geometry and introducing perturbations – show that this closed system can be largely influenced by small motions, artifacts that cannot be measured. Nonetheless, it can be concluded that the high fidelity simulation closely resembles the experimental facility. Additional studies are made to investigate the structures within the transfer pipe using POD as well as to investigate how increasing the Atwood number changes

mixing characteristics. The importance of mixing due to Schmidt number diffusion and sensitivity of the flow for a closed system has been established to support heat exchangers of this application.

5.1.3 Low Prandtl Number Flow

Heat transfer within rod bundles with lower than typical Prandtl numbers is critical, since literature shows that lower fidelity CFD has difficulty in proper temperature predictions. This project first analyzes data based on existing DNS data that incorporate liquid metal properties. Using channel flow data, the higher fidelity method of PANS is utilized to judge its suitability for low Prandtl number flows. However, it is shown that the accuracy of RANS and PANS for Pr = 0.71 is just as good as it is for Pr = 0.025. Therefore, a more complex scenario must be considered in order to contribute to improvement of modeling low Pr flows. Through literature review, the simple yet complex case of a tight lattice bare rod bundle is chosen for heat transfer analyses using DNS with different Prandtl numbers.

Development of the DNS benchmark, first, involves ensuring the Kolmogorov length scales are resolved and that the time step is never lower than the temporal scales. Since these ratios remain lower than one and the sensitivity on the polynomial order show statistics do not change, independence of spatial discretization is ensured. Validation with experimental results in wall shear stress, velocity, and turbulent kinetic energy show some discrepancies in the near-wall regions, hence comparisons with this benchmark must be conducted standalone rather than with both databases. A constant heat flux is added to the simulation with cases that have different Pr to find drastic differences in temperature profiles as well as its fluctuating component. Even when changing Pr by only a magnitude of 2 at Pr = 0.01, the bulk temperature varies much more than expected. Temperature distributions from the wall are presented to reveal significantly different shapes between all Prandtl numbers. Overall, the DNS benchmark has been developed and will be distributed to collaborators in efforts to aid modeling of Pr_t for liquid metal applications.

5.2 Further Study

Since the present HCSG study involves a simplified test section, future work necessitates a full geometry which becomes much more difficult to conduct. Experimental work has already been completed in Texas A&M University by Delgado et al. (2019) [90]. Additional analyses will be presented to obtain statistics useful for CFD validation as well as pressure fluctuations that supports flow-induced vibrations studies. Moreover, high fidelity simulations are being conducted by Yildiz et al. (2018) [91] and future studies involves additional comparisons. This will provide whole-field calculations that will be valuable for next generation HCSG designs. Future studies could also include simulations of flow-induced vibrations with Nek5000 as done by Brockmeyer et al. (2017) in [92].

The Cold Leg Mixing CFD-UQ benchmark project is still ongoing and will come to a close in the coming year of this writing. Blind test submissions for Atwood number of 0.10 are complete for Nek5000 in this present work and will be evaluated with the many participants of this NEA-OECD benchmark at the end of the project. After blind test results are released, future work will involve judging the accuracy of the chosen grid, buoyancy model, and mixing parameters. The instabilities and wave propogation within the transfer should be discussed for the higher A, so designers of nuclear safety can choose proper geometrical features and materials to prevent accident scenarios. Meetings with other participants will be held to complete these studies within a year of this writing.

Future work will also be conducted on the rod bundles for low Pr applications. Additional statistics will be documented from the DNS benchmark, and all information for collaborators to fine tune Pr_t modeling will be provided. The same turbulence modeling techniques used for channel flow mentioned in Bhushan et al. (2018) [83] will be utilized for the rod bundle benchmark. Moreover, implementation of different Pr_t modeling covered in literature will be investigated for it. The available information regarding turbulent kinetic energy and higher order statistics will prove beneficial for preventing difficulties that isotropic URANS methods had in previous literature. Finally, the DNS database of different Pr will contribute to making improvements to heat transfer modeling of liquid metals. Ideally, a universal thermal wall function and suitable Pr_t correlation

will be empirically derived from this database for low Pr modeling.

REFERENCES

[1] J. K. Lai, E. Merzari, and Y. A. Hassan, "Large eddy simulation of the flow behavior in a simplified helical coil steam generator," *Journal of Fluids Engineering*, vol. 141, no. 2, p. 021401, 2019.

[2] J. K. Lai, E. Merzari, and Y. A. Hassan, "Sensitivity analyses in a buoyancy-driven closed system with high resolution cfd using boussinesq approximation and variable density models," *International Journal of Heat and Fluid Flow*, vol. 75, pp. 1–13, 2019.

[3] J. Hooper and D. Wood, "Fully developed rod bundle flow over a large range of reynolds number," *Nuclear engineering and design*, vol. 83, no. 1, pp. 31–46, 1984.

[4] S. B. Pope, *Turbulent flows*. Cambridge University Press, 2001.

[5] J. Boussinesq, *Essai sur la théorie des eaux courantes*. Impr. nationale, 1877.

[6] A. N. Kolmogorov, "The local structure of turbulence in incompressible viscous fluid for very large reynolds numbers," in *Dokl. Akad. Nauk SSSR*, vol. 30, pp. 299–303, 1941.

[7] J. Smagorinsky, "General circulation experiments with the primitive equations: I. the basic experiment," *Monthly weather review*, vol. 91, no. 3, pp. 99–164, 1963.

[8] D. C. Wilcox *et al.*, *Turbulence modeling for CFD*, vol. 2. DCW industries La Canada, CA, 1998.

[9] F. R. Menter, "Two-equation eddy-viscosity turbulence models for engineering applications," *AIAA journal*, vol. 32, no. 8, pp. 1598–1605, 1994.

[10] S. Girimaji and K. Abdol-Hamid, "Partially-averaged navier stokes model for turbulence: implementation and validation," in *43rd AIAA Aerospace Sciences Meeting and Exhibit*, p. 502, 2005.

[11] S. S. Girimaji, "Partially-averaged navier-stokes model for turbulence: A reynolds-averaged navier-stokes to direct numerical simulation bridging method," *Journal of Applied Mechanics*, vol. 73, no. 3, pp. 413–421, 2006.

[12] A. Quarteroni and A. Valli, *Numerical approximation of partial differential equations*. Springer, 1994.

[13] M. O. Deville, P. F. Fischer, and E. H. Mund, *High-order methods for incompressible fluid flow*, vol. 9. Cambridge university press, 2002.

[14] P. Fischer, J. Lottes, S. Kerkemeier, O. Marin, K. Heisey, E. Obabko, A. annd Merzari, and Y. Peet, "Nek5000 user documentation," *Argonne National Laboratory*, 2016.

[15] N. Offermans, O. Marin, M. Schanen, J. Gong, P. Fischer, P. Schlatter, A. Obabko, A. Peplinski, M. Hutchinson, and E. Merzari, "On the strong scaling of the spectral element solver nek5000 on petascale systems," in *Proceedings of the Exascale Applications and Software Conference 2016*, p. 5, ACM, 2016.

[16] A. G. Tomboulides, J. C. Y. Lee, and S. A. Orszag, "Numerical simulation of low mach number reactive flows," *Journal of Scientific Computing*, vol. 12, pp. 139–167, Jun 1997.

[17] Y. Maday, A. T. Patera, and E. M. Rønquist, "An operator-integration-factor splitting method for time-dependent problems: application to incompressible fluid flow," *Journal of Scientific Computing*, vol. 5, no. 4, pp. 263–292, 1990.

[18] P. Fischer and J. Mullen, "Filter-based stabilization of spectral element methods," *Comptes Rendus de l'Académie des Sciences-Series I-Mathematics*, vol. 332, no. 3, pp. 265–270, 2001.

[19] D. Prabhanjan, G. Raghavan, and T. Rennie, "Comparison of heat transfer rates between a straight tube heat exchanger and a helically coiled heat exchanger," *International Communications in Heat and Mass Transfer*, vol. 29, no. 2, pp. 185–191, 2002.

[20] J. Doyle, B. Haley, C. Fachiol, B. Galyean, and D. Ingersoll, "Highly reliable nuclear power for mission-critical applications," in *Proceedings of ICAPP*, 2016.

[21] M. D. Carelli, L. Conway, L. Oriani, B. Petrović, C. Lombardi, M. Ricotti, A. Barroso, J. Collado, L. Cinotti, N. Todreas, *et al.*, "The design and safety features of the iris reactor," *Nuclear Engineering and Design*, vol. 230, no. 1-3, pp. 151–167, 2004.

[22] R. Simoneau and G. VanFossen, "Effect of location in an array on heat transfer to a short cylinder in crossflow," *Journal of Heat Transfer*, vol. 106, no. 1, pp. 42–48, 1984.

[23] D. Sumner, "Two circular cylinders in cross-flow: a review," *Journal of Fluids and Structures*, vol. 26, no. 6, pp. 849–899, 2010.

[24] D. K. Williams, D. P. Fassett, B. J. Webb, W. J. Bees, and A. S. Kruskamp, "Helical coil steam generator," June 17 2014. US Patent 8,752,510.

[25] E. Rivas and E. Rojas, "Heat transfer correlation between molten salts and helical-coil tube bundle steam generator," *International Journal of Heat and Mass Transfer*, vol. 93, pp. 500–512, 2016.

[26] R. Kharat, N. Bhardwaj, and R. Jha, "Development of heat transfer coefficient correlation for concentric helical coil heat exchanger," *International Journal of Thermal Sciences*, vol. 48, no. 12, pp. 2300–2308, 2009.

[27] J. Jayakumar, S. Mahajani, J. Mandal, P. Vijayan, and R. Bhoi, "Experimental and cfd estimation of heat transfer in helically coiled heat exchangers," *Chemical engineering research and design*, vol. 86, no. 3, pp. 221–232, 2008.

[28] H. Yuan, J. Solberg, E. Merzari, A. Kraus, and I. Grindeanu, "Flow-induced vibration analysis of a helical coil steam generator experiment using large eddy simulation," *Nuclear Engineering and Design*, vol. 322, pp. 547–562, 2017.

[29] S. J. Lee, S. Lee, and Y. A. Hassan, "Numerical investigation of turbulent flow in an annular sector channel with staggered semi-circular ribs using large eddy simulation," *International Journal of Heat and Mass Transfer*, vol. 123, pp. 705–717, 2018.

[30] S. Joh, "Thermal hydraulic studies on helical coil steam generator by cfd," in *ASME 2011 Pressure Vessels and Piping Conference*, pp. 399–404, American Society of Mechanical Engineers, 2011.

[31] M. Delgado, S. Lee, Y. Hassan, and N. Anand, "Flow visualization study at the interface of alternating pitch tube bundles in a model helical coil steam generator using particle image velocimetry," *International Journal of Heat and Mass Transfer*, vol. 122, pp. 614–628, 2018.

[32] S. Lee, M. Delgado, S. Lee, and Y. Hassan, "Flow visualization in a simplified helically coiled steam generator geometry," in *International Congress on Advances in Nuclear Power Plants (ICAPP'17), Fukui-Kyoto, Japan, Apr*, pp. 24–28, 2017.

[33] M. Delgado, S. Lee, and Y. Hassan, "Differences in experimental friction factors across two model helical coil steam generators," in *17th International Topical Meeting on Nuclear Reactor Thermal Hydraulics, Xi'an, China, Sept*, pp. 1–7, 2017.

[34] N. Jarrin, S. Benhamadouche, D. Laurence, and R. Prosser, "A synthetic-eddy-method for generating inflow conditions for large-eddy simulations," *International Journal of Heat and Fluid Flow*, vol. 27, no. 4, pp. 585–593, 2006.

[35] N. Jarrin, *Synthetic inflow boundary conditions for the numerical simulation of turbulence*. PhD thesis, University of Manchester, 2008.

[36] J. M. Österlund, *Experimental studies of zero pressure-gradient turbulent boundary layer flow*. PhD thesis, Mekanik, 1999.

[37] P. Bradshaw and G. P. Huang, "The law of the wall in turbulent flow," *Proc. R. Soc. Lond. A*, vol. 451, no. 1941, pp. 165–188, 1995.

[38] G. I. Taylor, "The spectrum of turbulence," *Proceedings of the Royal Society of London. Series A, Mathematical and Physical Sciences*, pp. 476–490, 1938.

[39] J. L. Lumley, "The structure of inhomogeneous turbulent flows," *Atmospheric turbulence and radio wave propagation*, 1967.

[40] L. Sirovich, "Turbulence and the dynamics of coherent structures. ii. symmetries and transformations," *Quarterly of Applied mathematics*, vol. 45, no. 3, pp. 573–582, 1987.

[41] D. Cavar and K. E. Meyer, "Les of turbulent jet in cross flow: Part 2 – pod analysis and identification of coherent structures," *International Journal of Heat and Fluid Flow*, vol. 36, pp. 35 – 46, 2012.

[42] E. Merzari, W. Pointer, and P. Fischer, "Numerical simulation and proper orthogonal decomposition of the flow in a counter-flow t-junction," *Journal of Fluids Engineering*, vol. 135, no. 9, p. 091304, 2013.

[43] L. H. Fick, E. Merzari, and Y. A. Hassan, "Direct numerical simulation of pebble bed flows: Database development and investigation of low-frequency temporal instabilities," *Journal of Fluids Engineering*, vol. 139, no. 5, p. 051301, 2017.

[44] J. Jeong and F. Hussain, "On the identification of a vortex," *Journal of fluid mechanics*, vol. 285, pp. 69–94, 1995.

[45] I. Campbell and J. Turner, "Turbulent mixing between fluids with different viscosities," *Nature*, vol. 313, no. 5997, p. 39, 1985.

[46] D. L. Youngs, "Three-dimensional numerical simulation of turbulent mixing by rayleigh–taylor instability," *Physics of Fluids A: Fluid Dynamics*, vol. 3, no. 5, pp. 1312–1320, 1991.

[47] K. O. Mikaelian, "Boussinesq approximation for rayleigh-taylor and richtmyer-meshkov instabilities," *Physics of Fluids*, vol. 26, no. 5, p. 054103, 2014.

[48] D. Livescu and J. Ristorcelli, "Variable-density mixing in buoyancy-driven turbulence," *Journal of Fluid Mechanics*, vol. 605, pp. 145–180, 2008.

[49] N. J. Mueschke, O. Schilling, D. L. Youngs, and M. J. Andrews, "Measurements of molecular mixing in a high-schmidt-number rayleigh–taylor mixing layer," *Journal of Fluid Mechanics*, vol. 632, pp. 17–48, 2009.

[50] C. Boyd, "Pressurized thermal shock," *Proceedings of the THICKET-3*, 2012.

[51] L. Wolf, U. Schygulla, W. Haeffner, K. Fischer, and W. Baumann, "Results of thermal mixing tests at the hdr-facility and comparisons with best-estimate and simple codes," *Nuclear Engineering and Design*, vol. 99, pp. 287–304, 1987.

[52] T. Theofanous and H. Yan, "A unified interpretation of one-fifth to full scale thermal mixing experiments related to pressurized thermal shock," tech. rep., Nuclear Regulatory Commission, Washington, DC (USA); California Univ., Santa Barbara, CA (USA). Dept. of Chemical and Nuclear Engineering, 1991.

[53] M. Scheuerer and J. Weis, "Transient computational fluid dynamics analysis of emergency core cooling injection at natural circulation conditions," *Nuclear Engineering and Design*, vol. 253, pp. 343–350, 2012.

[54] A. Shams, G. Damiani, D. Rosa, and E. Komen, "Design of a single-phase pts numerical experiment for a reference direct numerical simulation," *Nuclear Engineering and Design*, vol. 300, pp. 282–296, 2016.

[55] M. Loginov, E. Komen, and A. Kuczaj, "Application of large-eddy simulation to pressurized thermal shock problem: A grid resolution study," *Nuclear Engineering and Design*, vol. 240, no. 8, pp. 2034–2045, 2010.

[56] M. Raffel, C. E. Willert, F. Scarano, C. J. Kähler, S. T. Wereley, and J. Kompenhans, *Particle image velocimetry: a practical guide*. Springer, 2018.

[57] O. Marin, R. Vinuesa, A. Obabko, and P. Schlatter, "Characterization of the secondary flow in hexagonal ducts," *Physics of Fluids*, vol. 28, no. 12, p. 125101, 2016.

[58] J. S. Turner, *Buoyancy effects in fluids*. Cambridge University Press, 1979.

[59] T. M. Özgökmen, T. Iliescu, and P. F. Fischer, "Large eddy simulation of stratified mixing in a three-dimensional lock-exchange system," *Ocean Modelling*, vol. 26, no. 3, pp. 134–155, 2009.

[60] E. Spiegel and G. Veronis, "On the boussinesq approximation for a compressible fluid.," *The Astrophysical Journal*, vol. 131, p. 442, 1960.

[61] K. R. Harris, T. Goscinska, and H. N. Lam, "Mutual diffusion coefficients for the systems water–enthanol and water–propan-1-ol at 25 c," *Journal of the Chemical Society, Faraday Transactions*, vol. 89, no. 12, pp. 1969–1974, 1993.

[62] A. Reynolds, "The prediction of turbulent prandtl and schmidt numbers," *International Journal of Heat and Mass Transfer*, vol. 18, no. 9, pp. 1055 – 1069, 1975.

[63] J. Malm, P. Schlatter, P. F. Fischer, and D. S. Henningson, "Stabilization of the spectral element method in convection dominated flows by recovery of skew-symmetry," *Journal of Scientific Computing*, vol. 57, no. 2, pp. 254–277, 2013.

[64] J.-L. Guermond, R. Pasquetti, and B. Popov, "Entropy viscosity method for nonlinear conservation laws," *Journal of Computational Physics*, vol. 230, no. 11, pp. 4248–4267, 2011.

[65] V. Zingan, J.-L. Guermond, J. Morel, and B. Popov, "Implementation of the entropy viscosity method with the discontinuous galerkin method," *Computer Methods in Applied Mechanics and Engineering*, vol. 253, pp. 479–490, 2013.

[66] H. G. Weller, G. Tabor, H. Jasak, and C. Fureby, "A tensorial approach to computational continuum mechanics using object-oriented techniques," *Computers in physics*, vol. 12, no. 6, pp. 620–631, 1998.

[67] R. Issa, "Solution of the implicitly discretised fluid flow equations by operator-splitting," *Journal of Computational Physics*, vol. 62, no. 1, pp. 40 – 65, 1986.

[68] B. Launder and B. Sharma, "Application of the energy-dissipation model of turbulence to the calculation of flow near a spinning disc," *Letters in Heat and Mass Transfer*, vol. 1, no. 2, pp. 131 – 137, 1974.

[69] J. Mahaffy, B. Chung, C. Song, F. Dubois, E. Graffard, F. Ducros, M. Heitsch, M. Scheuerer, M. Henriksson, E. Komen, *et al.*, "Best practice guidelines for the use of cfd in nuclear reactor safety applications-revision," tech. rep., Organisation for Economic Co-Operation and Development, 2015.

[70] W. L. Oberkampf and C. J. Roy, *Verification and validation in scientific computing*. Cambridge University Press, 2010.

[71] W. M. Kays, "Turbulent prandtl number–where are we?," *Journal of Heat Transfer*, vol. 116, no. 2, pp. 284–295, 1994.

[72] K. Mikityuk, "Heat transfer to liquid metal: review of data and correlations for tube bundles," *Nuclear Engineering and Design*, vol. 239, no. 4, pp. 680–687, 2009.

[73] C.-H. Lefhalm, N.-I. Tak, H. Piecha, and R. Stieglitz, "Turbulent heavy liquid metal heat transfer along a heated rod in an annular cavity," *Journal of Nuclear materials*, vol. 335, no. 2, pp. 280–285, 2004.

[74] L. Maciocco, "Assessment of turbulence models for heavy liquid metals in computational fluid dynamics," 2002.

[75] W. M. Kays, *Convective heat and mass transfer*. Tata McGraw-Hill Education, 1993.

[76] A. Shams, F. Roelofs, E. Baglietto, S. Lardeau, and S. Kenjeres, "Assessment and calibration of an algebraic turbulent heat flux model for low-prandtl fluids," *International Journal of Heat and Mass Transfer*, vol. 79, pp. 589–601, 2014.

[77] N. Kasagi and Y. Ohtsubo, "Direct numerical simulation of low prandtl number thermal field in a turbulent channel flow," in *Turbulent Shear Flows 8*, pp. 97–119, Springer, 1993.

[78] H. Abe, H. Kawamura, and Y. Matsuo, "Surface heat-flux fluctuations in a turbulent channel flow up to reτ= 1020 with pr= 0.025 and 0.71," *International Journal of Heat and Fluid Flow*, vol. 25, no. 3, pp. 404–419, 2004.

[79] M. Niemann and J. Fröhlich, "Buoyancy-affected backward-facing step flow with heat transfer at low prandtl number," *International Journal of Heat and Mass Transfer*, vol. 101, pp. 1237–1250, 2016.

[80] L. Meyer, "From discovery to recognition of periodic large scale vortices in rod bundles as source of natural mixing between subchannels–a review," *Nuclear Engineering and Design*, vol. 240, no. 6, pp. 1575–1588, 2010.

[81] E. Baglietto, H. Ninokata, and T. Misawa, "Cfd and dns methodologies development for fuel bundle simulations," *Nuclear Engineering and Design*, vol. 236, no. 14-16, pp. 1503–1510, 2006.

[82] N. Kasagi and O. Iida, "Progress in direct numerical simulation of turbulent heat transfer," in *Proceedings of the 5th ASME/JSME Joint Thermal Engineering Conference*, pp. 15–19, American Society of Mechanical Engineers San Diego, 1999.

[83] S. Bhushan, O. ElFajri, W. Jock, D. Walters, J. Lai, Y. Hassan, R. B. Jackson, A. Obabko, and E. Merzari, "Assessment of rans, les, and hybrid rans/les models for the prediction of low-pr turbulent flows," in *ASME 2018 5th Joint US-European Fluids Engineering Division Summer Meeting*, pp. V001T08A005–V001T08A005, American Society of Mechanical Engineers, 2018.

[84] J. D. Hooper, D. Wood, and W. Crawford, "Data bank of developed single-phase flow through a square-pitch rod cluster for four reynolds numbers," tech. rep., Australian Atomic Energy Commission Research Establishment, 1983.

[85] P. Welch, "The use of fast fourier transform for the estimation of power spectra: a method based on time averaging over short, modified periodograms," *IEEE Transactions on audio and electroacoustics*, vol. 15, no. 2, pp. 70–73, 1967.

[86] E. Merzari, H. Ninokata, and E. Baglietto, "Numerical simulation of flows in tight-lattice fuel bundles," *Nuclear Engineering and Design*, vol. 238, no. 7, pp. 1703–1719, 2008.

[87] E. Baglietto, "Rans and urans simulations for accurate flow predictions inside fuel rod bundles," 2007.

[88] T. L. Bergman, F. P. Incropera, D. P. DeWitt, and A. S. Lavine, *Fundamentals of heat and mass transfer*. John Wiley & Sons, 2011.

[89] J. K. Lai, E. Merzari, and Y. A. Hassan, "Towards low prandtl number investigations with direct numerical simulation in fuel bundles," in *ANS Annual 2018 Driving the Future of Nuclear Technology*, 2018.

[90] M. Delgado, Y. Hassan, and N. Anand, "Experimental flow visualization study using particle image velocimetry in a helical coil steam generator with changing lateral pitch geometry," *International Journal of Heat and Mass Transfer*, vol. 133, pp. 756 – 768, 2019.

[91] M. Yildiz, E. Merzari, and Y. Hassan, "Large eddy simulation of 5-tube bundle helical coil steam generator test section," p. V008T09A043, 07 2018.

[92] L. Brockmeyer, J. Solberg, E. Merzari, and Y. Hassan, "Simulation of fluid-structure interaction of crossflow through a tube bundle and experimental validation," in *ASME 2017 Fluids Engineering Division Summer Meeting*, pp. V01BT11A019–V01BT11A019, American Society of Mechanical Engineers, 2017.